Modelling thermal conductivity of porous thermal barrier coatings for high-temperature aero engines

Ramandeep Singh Ghai

A thesis submitted to the Faculty of Engineering in partial fulfilment of the requirement for the degree of

Master of Applied Science

Ottawa-Carleton Institute for Mechanical and Aerospace Engineering

University of Ottawa, Ottawa, Canada.

September 2017

Acknowledgements

This thesis is the product of years of work, procrastination, changing minds, ideas and opinions. It is a delight to acknowledge those who have supported and motivated me to finish my thesis.

Firstly, I wish to express my deepest gratitude to my supervisors Prof. Dr. Kuiying Chen (Senior Research Officer, Aerospace Portfolio, NRC Ottawa) and Prof. Dr. Natalie Baddour (Chair of the Department of Mechanical Engineering, University of Ottawa) for their excellent concern and endless support during my Master's thesis.

I would like to thank Dr. Kuiying Chen for his support, guidance, inspiration and especially for his patience throughout this research work. Dr. Chen introduced me to the technical details of this study and helped me to better understand every tiny detail of this field. Whenever I got deviated from the path, he was always there to guide me back on the right track and motivated me to work in a smarter way. During the last year and a half, we had weekly meetings to discuss the progress of research work. We worked together as a team to tackle every technical difficulty. I am grateful to Dr. Chen for his faith in me.

Also, I would like to thank Dr. Natalie Baddour for her invaluable suggestions and discussions. She always helped me to better understand the way of writing and details that I needed for this thesis work. Dr. Baddour helped me financially by having me as her Teaching Assistant. She has given me her precious time to discuss the technical details with her. She also guided me in optimizing my research and writing. She made me familiar with software that helped me a lot during the thesis. She sponsored me to participate in the 29th Canadian Material Science Conference. During the conference, I met many researchers from the Materials field and gained an enormous amount of knowledge. I felt really honoured when I won the First place in the Poster Presentation. I really respect her from the core of my heart.

I would like to take some time to thank my friends who stand by my decision to choose the Masters of Applied Science. I really appreciate Dildar Singh for guiding me to understand the MATLAB software. He is like a brother to me. Also, I would like to thank Arman, Nikhil, Faisal, Paschal, Jennifer, and Vinay for their moral support during my studies. These friends inspired me in unexpected ways. I would like to present special thanks to Huan, who helped me to understand the details for my TA duties and helped me for poster making. She has been always kind to me.

Finally, I would thank my mom and dad for their encouragement, support and love. I am thankful to my elder sister Roohi, for being on my side. Without my family's support and guidance, I could never have been completed my work.

Abstract

Thermal Barrier Coatings (TBC) are used to shield hot sections of gas turbine engines, helping to prevent the melting of metallic surfaces. TBC is a sophisticated layered system that can be divided into top coat, bond coat, and the super-alloy substrate. The highly heterogeneous microstructure of the TBC consists of defects such as pores, voids, and cracks of different sizes, which determine the coating's final thermal and mechanical properties. The service lives of the coatings are dependent on these parameters.

These coatings act as a defensive shield to protect the substrate from oxidation and corrosion caused by elevated temperatures. Yttria Stabilized Zirconia (YSZ) is the preferred thermal barrier coating for gas turbine engine applications. There are a certain number of deposition techniques that are used to deposit the thermal coating layer on the substrate; commonly used techniques are Air Plasma Sprayed (APS) or Electron Beam Physical Vapour Deposition (EB-PVD).

The objective of this thesis is to model an optimized TBC that can be used on next-generation turbine engines. Modelling is performed to calculate the effective thermal conductivity of the YSZ coating deposited by EB-PVD by considering the effect of defects, porosities, and cracks. Bruggeman's asymmetrical model was chosen as it can be extended for various types of porosities present in the material. The model is used as an iterative approach of a two-phase model and is extended up to a five-phase model. The results offer important information about the influence of randomly oriented defects on the overall thermal conductivity. The modelled microstructure can be fabricated with similar composition to have an enhanced thermal insulation.

The modelling results are subsequently compared with existing theories published in previous works and experiments. The modelling approach developed in this work could be used as a tool to design the porous microstructure of a coating.

List of Abbreviations

APS	Air Plasma Sprayed
EB-PVD	Electron Beam-Physical Vapour Deposition
EB-DVD	Electron Beam-Directed Vapour Deposition
CVD	Chemical Vapour Deposition
FEM	Finite Element Method
FEA	Finite Element Analysis
LOM	Light Optical Microscopy
LFA	Laser Flash Analysis
MIP	Mercury Intrusion porosimetry
SANS	Small Angle Neutron Scattering
TBC	Thermal Barrier Coatings
YSZ	Yttria-Stabilized Zirconia
XRD	X-Ray Diffraction
TGO	Thermally Grown Oxide
NACA	National Advisory Committee for Aeronautics

Table of Contents

List of Figures

List of Tables

1. Introduction

1.1 Introduction to Thermal Barrier Coatings

The advancement in high-temperature engineering alloys led to the design and development of the present era turbine engines. The laws of thermodynamics suggest that with an increase in inlet operating temperature, the performance and efficiency of an engine can be increased [1]. This improvement in power and efficiency is necessary to make the system economical as well as environmentally friendly.

The components of a turbine engine are exposed to elevated temperatures as well as to an oxidative and corrosive gaseous environment. In certain cases, there are some impacts from high-velocity foreign particles during operation [2]–[4]. Material properties such as high-temperature strength, good stress relaxation, higher resistance to hot corrosion and oxidation are required for a base metal or alloy [5]. Generally, super-alloys are best suited for substrate material [6]. With technical advancements and ever-increasing design specifications, these super-alloys have almost reached their theoretical design limit. Improvement in engine design slowed down after the mid-1900's due to the very significant improvements in earlier designs [7]. Figure 1-1 shows the stages of evolution of super-alloys within the past six decades. It is evident that development has been almost stable since about 2008. With advancements in high-temperature capability and cooling technologies, these super-alloys are now able to withstand higher temperatures than ever before.[8].

To further enhance the design and efficiency, the recent trend shifted towards the use of ceramically coated components in turbine engines [9]. In this case, the components used at elevated temperatures are coated with a ceramic coating to provide protection against high-temperature degradation. These ceramic coatings are known as the Thermal Barrier Coatings

(TBC) and are used to protect the super-alloy components [10]. These coatings protect the base metal from damage at elevated temperature and increase the lifetime and efficiency of the component. TBC provides thermal shock resistance, creep resistance, strain tolerance, protection against hot corrosion and stability to the substrate at higher temperatures[11] [12].

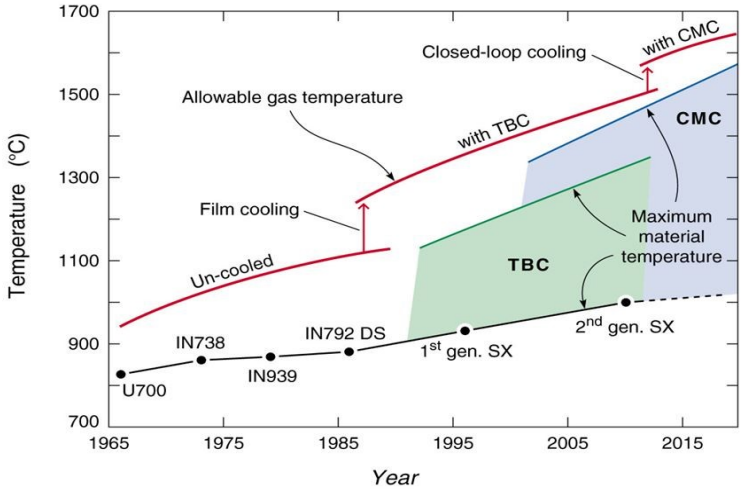

Figure 1-1 Development of high-temperature super-alloys and cooling technology over six decades [8]

TBCs have become an integral part of gas turbine engines as they enhance the operational lifetime, along with the betterment of turbine efficiency [13], [14]. Figure 1-2 provides an overview of where these TBCs are used in high-pressure turbine aero-engines. The simple structure of the TBC system (Figure 1-2) consists of the ceramic top coat, bond coat and superalloy substrate. During service life, a thermally grown oxide (TGO) layer (mostly α-Al_2O_3) forms on the bond coat surface and reduces the rate of oxidation [15]. The objective of the top ceramic coating is to reduce the metal temperature. A metallic bond coat is used to enhance the bonding between the top coat and the underlying super-alloy and to protect the super-alloy from oxidation and hot corrosion [16]. Yttria-stabilized Zirconia [YSZ] containing 6-8%Y_2O_3 is known as a state of the art thermal barrier coating [10]. However, the bond coat is composed of MCrAlY where usually M=Ni, Co or NiCo [17]. The key properties of YSZ TBC are low thermal conductivity, high melting point, phase compatibility with alpha alumina,

and the combination of good resistance to corrosion and damage from large particle impacts [18].

The microstructure of ceramic coatings is highly heterogeneous as it consists of imperfections such as pores, voids, and vacancies, along with cracks of different shapes and sizes. Overall, the thermal conductivity of the coating is highly affected by the presence of such defects [19], [20] and spraying parameters [21]. The extent of change in the thermal and mechanical properties depends on the amount, size, and morphology of the defects present in the coating.

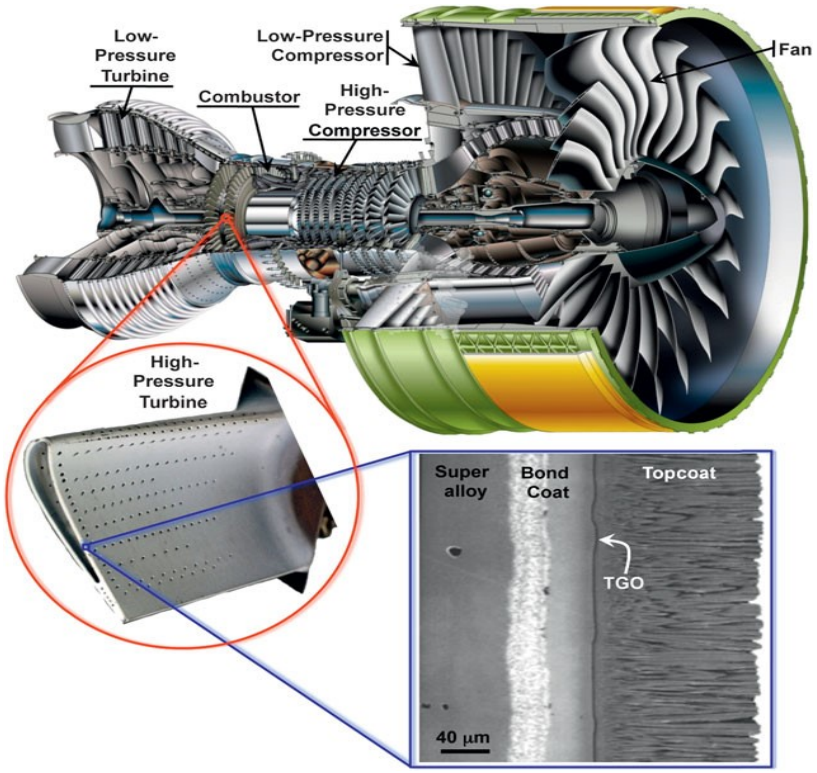

Figure 1-2 Cutaway view of Engine Alliance GP7200 aircraft engine, a photograph of a turbine blade (~10 cm long) with a thermal-barrier coating (TBC) from the high-pressure hot section of an engine, and a scanning electron microscope (SEM) image.[22]

The lifetime of a coating is also highly dependent on its thermal and mechanical properties, hence ultimately the service life of the part is dependent on the density of the defects present. Defects lead to a lower value for thermal conductivity and a lower thermal conductivity

implies a longer service life, as heat transfer to the substrate is reduced. Lower heat transfer into the substrate also leads to lower damage to the coating interface, where most of the failure occurs [16]. To achieve lower values for thermal conductivity, better strain tolerance and higher lifetime, the distribution of cracks and pores in the coating needs to be optimized [23]. It thus becomes essential to understand the fundamental microstructural properties of the TBC in order to produce an optimized coating.

One of the goals of future engine designs is to develop materials or processes that reduce the temperature of the metal surface while concomitantly facilitating increased gas path temperatures. Hence, one of the aims of TBC design is to design coatings with a lower thermal conductivity. Design optimization can be performed using experimentation or through simulation methods. Experimentation is the traditional approach to optimizing the coating microstructure. In this approach, various parameters are pre-set and coatings are deposited to generate samples. Various types of tests are performed to evaluate the coating structure. This approach is iterative, time-consuming and expensive. This technique does not offer any quantitative knowledge or understanding about microstructural properties.

At the same time, modelling or/and simulation is a cost-effective and flexible approach to optimize and understand the coating microstructure. Development of new types of coatings design or new structures can easily be performed. Modification of the parameters is simple and the analysis can be performed quickly compared to a traditional experimental approach. Simulation can provide analysis of different microstructural parameters and their individual effect, as well as the combined effect on the TBC. With a better understanding of microstructural properties and complex process variables, highly sophisticated fabrication techniques can then be developed.

The relation between microstructural properties and process parameters for modelling are obtained through the link with experimental parameters during this work [24]. Development of materials with lower thermal conductivity will further help in reducing thermal transport to the substrate [25].

1.2 Objectives and Limitations

The aim of this thesis work is to propose and validate a model for evaluating thermal conductivity of TBCs. The proposed model could then be used to optimize TBC microstructure exhibiting low thermal conductivity along with high strain tolerance, and a lifetime comparable to the best thermal sprayed coatings currently used in industrial gas turbine engines.

Simulation is used for this thesis work due to its benefits over the experimental technique. The present study is based on the different types of defects (pores, voids and cracks) that are present in the coating during the fabrication of the coating and is not dependent on the material and equipment used during fabrication. Pores are empty space in the material (can be filled with liquid or gas phase) and the voids are the pores that remain unoccupied and typically the result of an imperfection. The independence of material and process is not always a valid assumption; hence, there can be certain limitations of this work when applied to other coatings or materials.

The material chosen for the top coat in this work is yttria-stabilized zirconia $ZrO_2$6-8%Y_2O_3 or [YSZ]. The reason for using (YSZ) is its efficient properties at a higher temperature, such as good resistance to high-temperature corrosion, higher stability, and lower thermal conductivity for a high-temperature range [26], [27]. The material for the bond coat is NiCoCrAlY [28].

There are some specific deposition techniques that are used to deposit these thermal barrier coatings on super-alloys. Some of these techniques are Electron Beam Physical Vapour

Deposition (EB-PVD), Air Plasma Sprayed (APS), Chemical Vapour Deposition (CVD), Electron Beam Directed Vapor Deposition (EB-DVD), as well as others [26], [29]–[32]. In this thesis, EB-PVD is chosen to be the deposition technique. It is used for depositing the coating on the aero engine components because of certain benefits such as higher strain tolerance or strain accommodation, better surface finish, and higher operating temperature range, which can be attributed to its columnar structure [32], [33].

In this modelling work, the changes in the chemistry or the effects of these changes on the coating are not considered. For the simplicity of the model, the microstructure is comprised of only the defects (different defects are assumed embedded in a continuous matrix). The material properties are independent of temperature (this assumption is not valid for very high temperature, $>1500^0$C). All the pores or defects are assumed independent of each other. The effect of heat transfer by radiation in the pores or coatings is neglected [34]. Thermal conductivity is the only thermal property that is modelled in this thesis work.

1.3 Contributions of the thesis

In this thesis, an improvement to the existing model used to predict the thermal conductivity of the porous material is proposed and validated. A two-phase model is used as the reference model to construct a five-phase composite model. The development of the proposed model is based on an iterative approach. It is demonstrated that the proposed model predicts the thermal conductivity values of porous coatings more effectively than existing models. The proposed five-phase model offers thermal conductivity values near to experimental values. The results obtained from the proposed model were compared with experimental results, results from a four-phase model and to FEA results.

The thesis is structured as follows. An introduction to TBCs, a little history and background details are first discussed. The details about the two widely used deposition

techniques are presented in Chapter 2. Chapter 3 incorporates a brief introduction to previous numerical and analytical models. The details of the proposed model, the five-phase model, for porous composite materials are presented in Chapter 4. The verification of the proposed model using the results from experimental data and comparison to the results of the four-phase model and FEA results is performed in Chapter 5. Finally, in Chapter 6, conclusions are drawn.

2. Literature review

2.1 History

To introduce the thesis work, a brief review of the history of TBC is needed. Thermal barrier coatings have been used for over half a century in gas turbine/aeroplane engines [18], [21], [22], [35]–[41]. The first ever turbine blade-oriented ceramic coating was the frit-enamel coating, developed between the years 1942 to 1956 by the National Advisory Committee for Aeronautics (NACA). In the year 1960, the benchmark use of ROKIDE thermal barrier coatings on the rocket engine XLR99's nozzle on flight X-15 occurred [42]. Zirconia was used as the top coat and the bond coat was nickel chrome. These coatings served the dual purpose of preventing the oxidation of the tube assembly and preventing the boiling of liquid ammonia. In Figure 2-1, the brazed stainless-steel tube structure with Rokide Z TBC is shown. The graded rokide TBC prevented the premature spallation of the X-15 combustion chamber [42].

In the mid-70s, the development of modern thermal spray coatings was a big step towards modern ceramic coatings. For the J-75 engine test, a thermal barrier coating of zirconia-12%yttria on NiCrAlY survived for longer than any earlier coatings. The keys to this accomplishment were the use of Yttria as a Zirconia Stabilizer and the use of an MCrAlY type bond coat. This success of ROKIDE TBC demonstrated that Blade TBCs were feasible [43].

Stecura reported on the optimum zirconia-yttria TBC composition in the report on 'Effects of compositional changes on the performance of a thermal barrier coating system' [44].

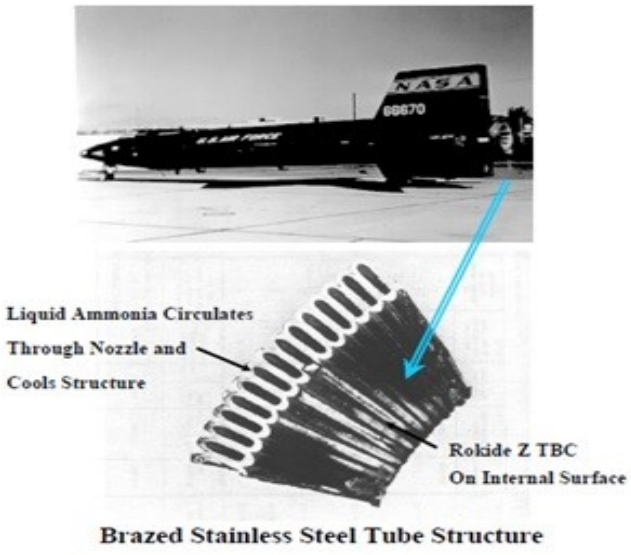

Figure 2-1 ROKIDE TBC used on XLR99 rocket for X-15 Flight [42]

This composition (ZrO_2-6-8%Y_2O_3) is still considered to be a state of the art TBC composition [44]. Similar results can be seen in Figure 2-2, where the cycles of failure were calculated as a function of the concentration of yttria in the zirconium.

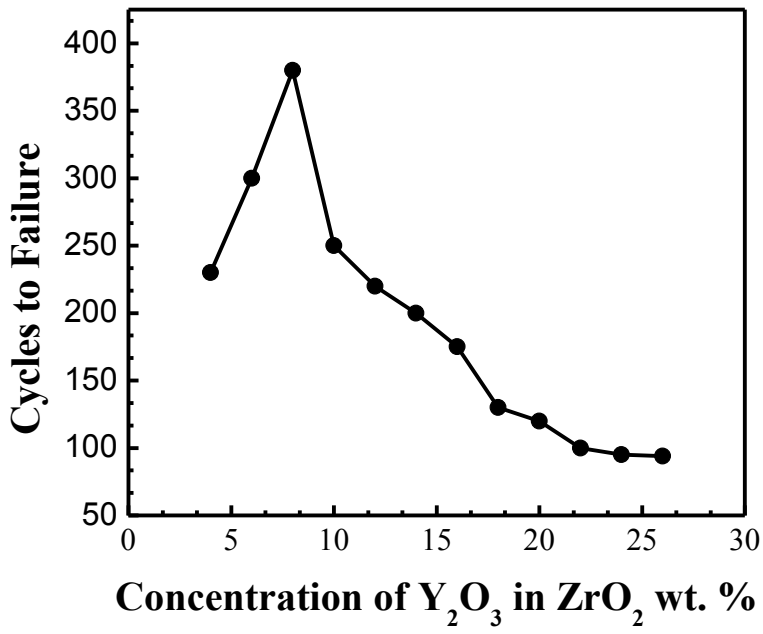

Figure 2-2 Number of cycles to failure Vs Concentration of Yttrium in Zirconia (Reconstructed from [7])

2.2 Background

The development of high-temperature super-alloys was the primary driver to increase the operating temperature in turbine engines for almost 50 years [1]. The improvements in engine performance slowed in the mid-1990's as super-alloys approached their theoretical composition limits and temperature ranges. With little prospect for significant improvement in alloy performance, the trend shifted towards multi-layered ceramic coatings that can be applied to hot section superalloy components for efficient operation under high temperature and harsh conditions [45].

TBCs are widely used in modern power generation, and marine/aero engine applications to lower the temperature of a metallic surface in the combustor and for turbine components such as blades or vanes. The use of TBCs can offer increased engine thrust as well as a performance by allowing elevated gas temperatures or by reducing cooling air flow. Increased lifetime of turbine blades[46], [47] is also promoted by decreasing metal temperatures. Figure 2-3 describes the various benefits of a system with a thermal barrier coating. From the work of Schulz, it became evident that thrust, performance and life of the component increase with the use of TBCs [48].

2.3 Thermal barrier coatings

Thermal barrier coatings are material combinations that can lower heat transfer from hot gases to the metallic substrate. The structure of TBC system consists of an insulating ceramic topcoat layer and an intermediate bond coat layer placed on top of a superalloy substrate. A single-crystal super-alloy substrate is preferred that contains 5 to 12 elements (in addition to the Ni-base element) to optimize high-temperature strength, ductility, oxidation and hot-corrosion resistance [49].

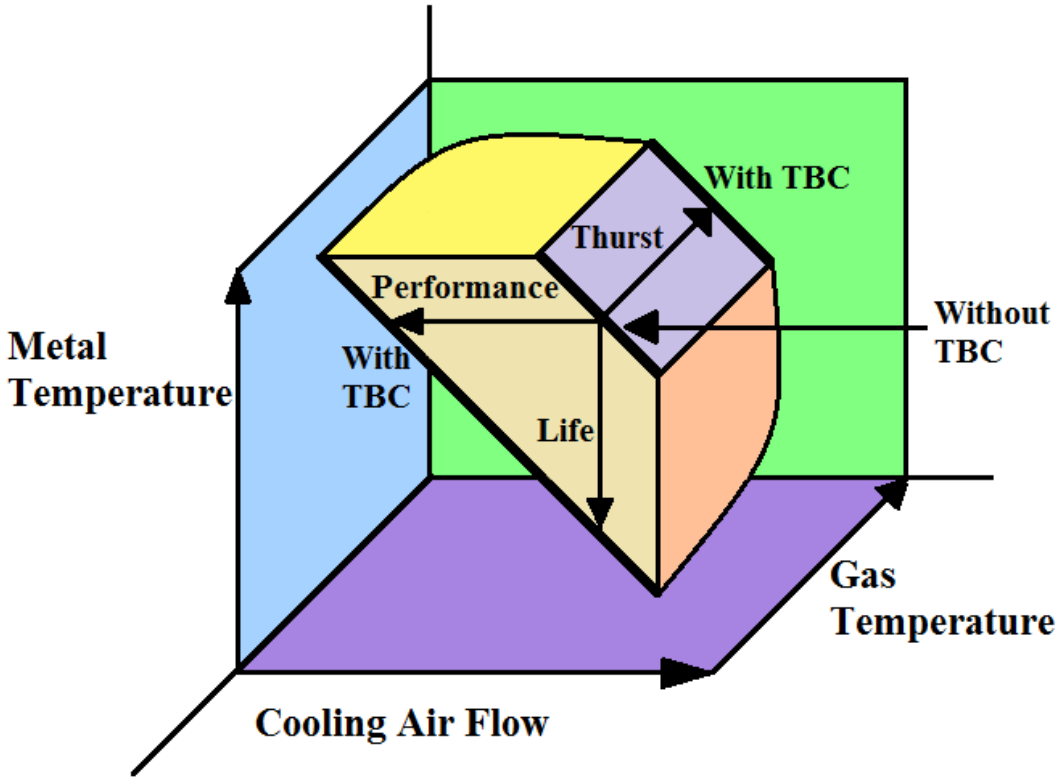

Figure 2-3 Potential benefits of gas turbines for the use of TBCs [48]

Blades and vanes are subjected to high centrifugal loads and high stresses, so the essential requirement for the super-alloy material used for these is to be creep resistant [50]. Blade or vanes are mostly made of nickel-based super-alloys that have the required material properties. These structures are internally cooled by the flow of cool air through internal serpentine cooling passages [51]. Small holes allow cooling air to form a thin air film on the blade surface.

TBC protects the gas turbine components from severe thermal environments, thus improving the efficiency and at the same time decreasing unwanted emissions. Turbine entry gas temperatures can be higher than $1{,}500^{0}$C with TBCs providing a temperature drop of about 200-300^{o}C across the thickness of the coating [52]. The efficiency (ε) of a TBC can be expressed by the following equation [53]

$$\varepsilon = \frac{T_2 - T_1}{T_2} \tag{2.1}$$

where T_2 is the operating temperature and T_1 is the sink temperature. Thus, any increase in T_2 (Turbine Entrance Temperature) results in an increase in the efficiency.

TBCs exhibit the low thermal conductivity crucial for a decrease in heat transfer from the hot combustion gases to the super-alloy substrate of the turbine blade [54], [55]. The combination of TBC with an internal blade cooling system can enable the gas turbine engine to operate at a temperature much higher than the melting temperature of the super-alloys [1], [56]. The challenge of high-temperature phase stability and sintering resistance becomes evident with higher ceramic layer surface temperature [57].

A schematic of simple an EB-PVD TBC system is shown in Figure 2-4. It consists of a top coat, Thermally Grown Oxide (TGO), bond coat and substrate. Each of these has different materials with specific functions and properties.

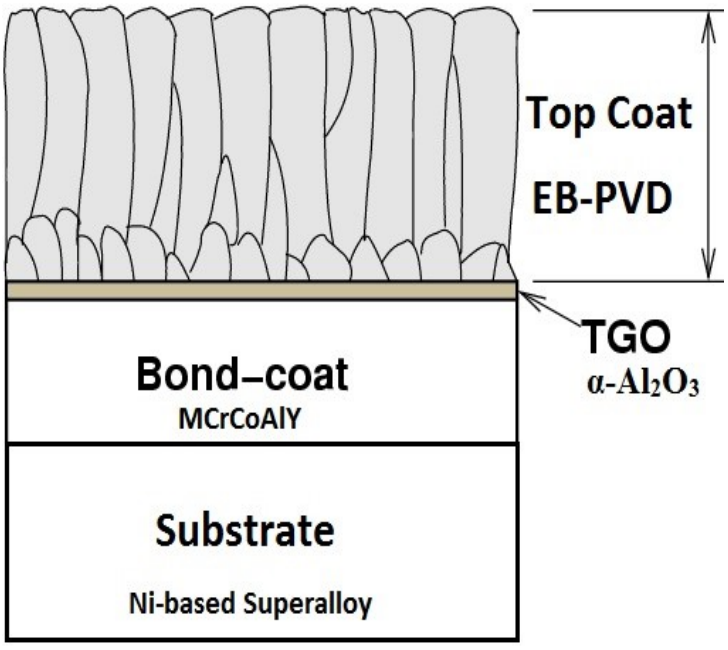

Figure 2-4 Schematic of a thermal barrier coating (TBC) obtained by electron beam physical vapour deposition (EBPVD)

The bond coat layer is applied to the superalloy substrate. TGO forms on the outer side of the bond coat. The top coat is applied to the TGO-covered bond coat [58]. Typical types of bond coats include the Platinum modified nickel aluminide (NiAl + Pt) [59] or MCrAlY overlays (M can be Ni, Co or NiCo) [52]. Bond coat protects the oxidation of the substrate by oxidation of aluminium and other reactive metals such as Cr or Y; these can form a protective thermally grown oxide layer adherent to the bond coat [60]. The most common oxide layer that forms during top coat deposition or service life is α-Al_2O_3 [60], [61]. The temperature distribution along the different layers of TBCs can be seen in Figure 2-5

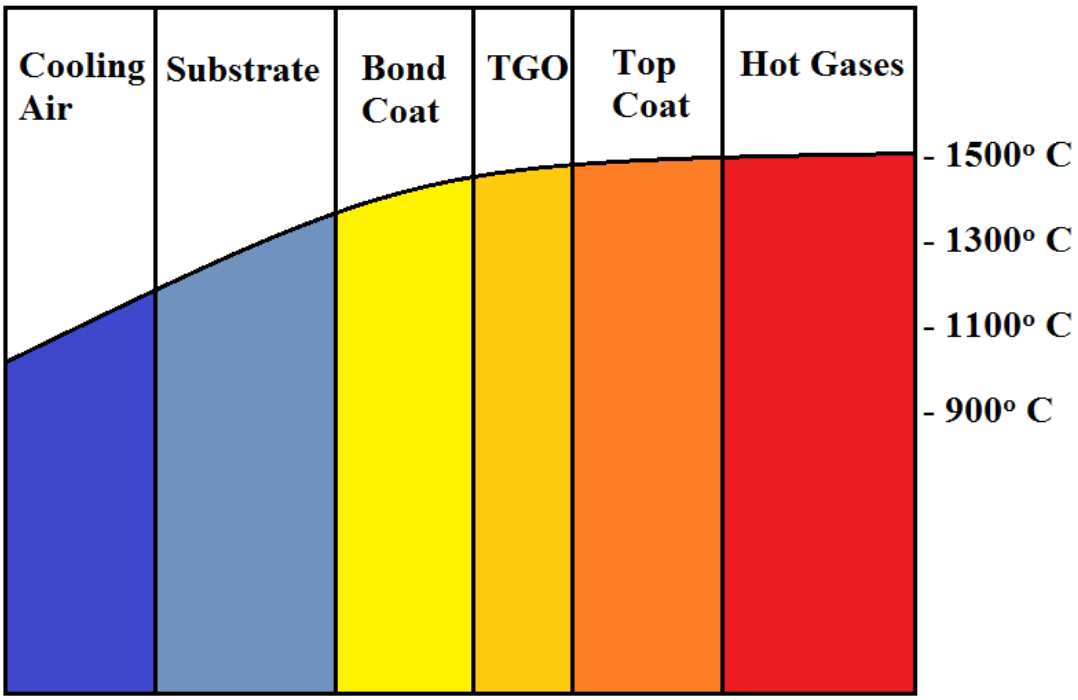

Figure 2-5 Schematic of thermal barrier coating system with temperature distribution along the cross-section of the internally cooled component.

Improvement in the performance of TBCs remains a key objective for the further development of gas turbine applications [62]. A key objective of such applications is to maximise the temperature drop across the topcoat, thus allowing higher turbine entry temperatures and higher engine efficiencies [63], [64]. This comes with the requirement that the thermal conductivity of the ceramic topcoat should be minimized and that the value should

remain low during prolonged exposure to service conditions. Lowering the thermal conductivity has a counter effect on certain other properties such as high-temperature phase stability [57] and sintering resistance (avoiding the agglomeration of particles) [65] that are essential for a better life of a coating.

The growth of the TGO layer depends on the oxidation of Al, Cr, Y, or other metals. Oxygen penetrates the coating and a thermally grown oxide layer is formed between the top coat and bond coat. The easy diffusion of oxygen from the engine environment to the bond coat is due to the interconnected porosity that is always present in the top-coat layer. Oxygen has a very high ionic diffusivity in ZrO_2-based ceramics. This diffusivity makes even dense top coats "oxygen-transparent" [58].

TGO growth rate is usually well modelled by the parabolic growth law as [66]

$$h^2 = 2k_p t \tag{2.2}$$

where h is the thickness (μm), t is time (s) and k_p is a parabolic rate constant. TGO growth involves the counter-diffusion of oxygen and aluminium along the α-Al_2O_3 grain boundaries. Figure 2-6 represents the inward diffusion of oxygen and outward diffusion of aluminium from the bond coat. The grain size of α-Al_2O_3 determines the diffusion flux and the parabolic TGO growth rate [67]. Transient metastable alumina (gamma and theta) is generally expected to form during the initial stage of oxidation and then transform to the stable α-Al_2O_3 [68]–[70]. The formation of new α-Al_2O_3 occurs at the bond coat interface (when inward diffusion of oxygen is rapid) or at the surface of TGO (when outward diffusion of aluminium is faster).

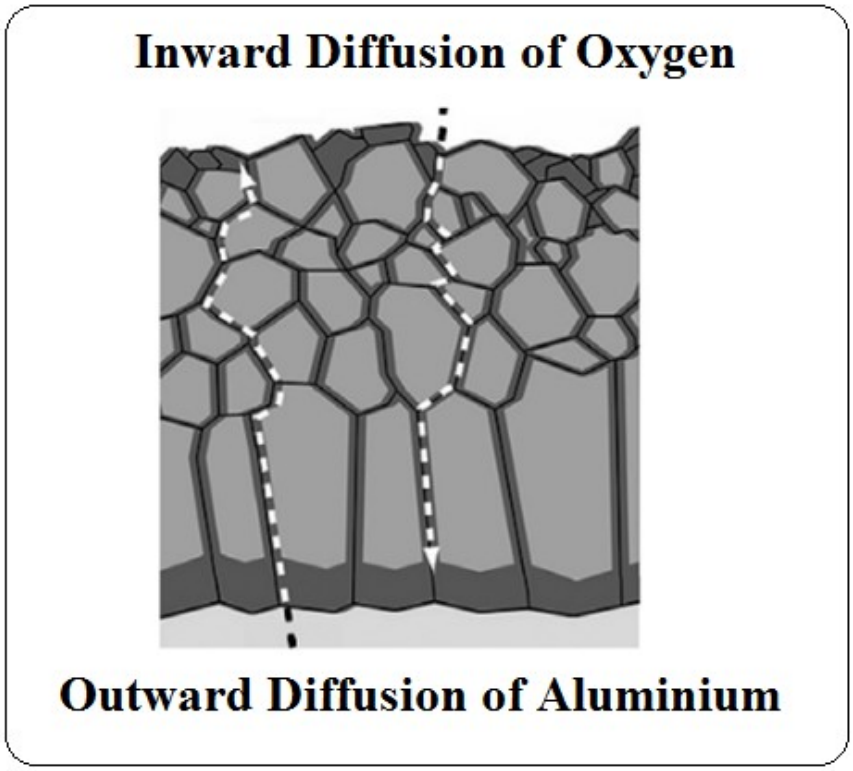

Figure 2-6 The inward diffusion of oxygen and outward diffusion of aluminium from the bond coat.

2.3.1 Coating deposition techniques

The thermal conductivity of a coating is greatly affected by the technique that is used to deposit the coating layer. The microstructural properties change based on different coating techniques. There are several methods that are in use today for deposition, however, in this thesis, only APS and EB-PVD techniques are explained. These techniques are the most widely used for land-based turbine engines and aero engines respectively. Most of the new techniques are based on these two types of coating methods.

Air Plasma Sprayed

Air Plasma Spray (APS) is a low-cost method for depositing ceramic TBC that are used to protect and to insulate hot-section metallic components in gas turbine and diesel engines [22]. APS is characterized by the high temperature of the plasma jet, which allows the melting of

materials (having a high melting point) to yield an effective thermal spray. High-speed Ar–He or Ar–H_2 hot plasma jet dissolves the ceramic and metallic feedstock powder and accelerates it to a high velocity.

A schematic illustration of APS coating technique can be seen in Figure 2-7. The impact of the spray onto the prepared surface of the substrate forms a coating by solidifying rapidly. The plasma spray creates “splats”, the flattened particle boundaries that run parallel to the ceramic-metal interfaces.

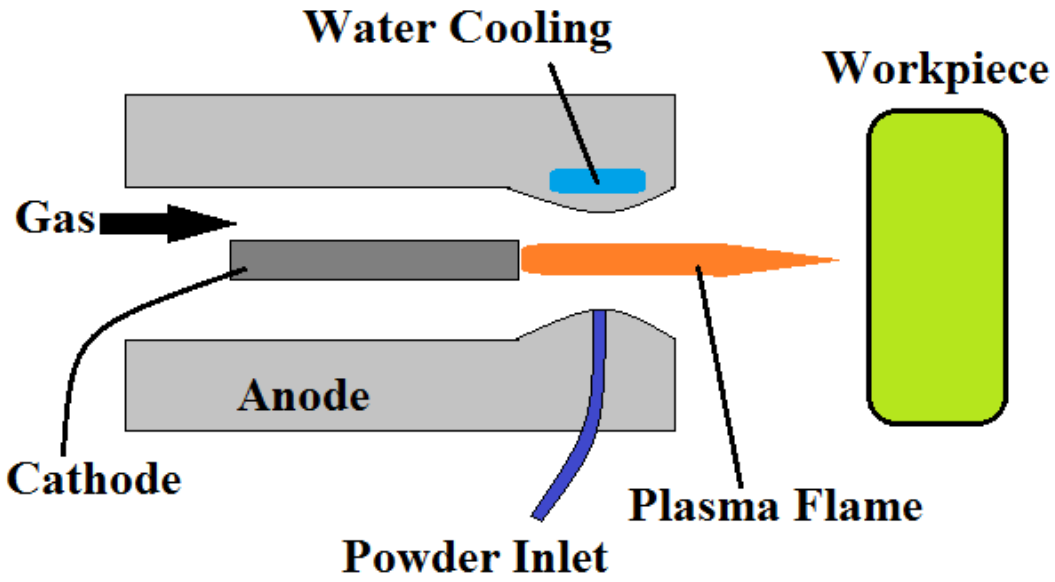

Figure 2-7 Schematic of air plasma spray technique

Figure 2-8 provides an illustration of the APS splats. There is some spacing left between the splat boundaries during the coating process, which is due to incomplete bonding between splats owing to the lack of adhesion, relaxation of residual stresses during the cooling of the splat, or trapped gases. The actual area of contact between the various splats is only around

20% [71] that can be enhanced using modern techniques (near 5%)[72]. This affects the properties of the coatings, such as mechanical, thermal, and electrical properties, and the properties are very different compared to the sprayed bulk material.

There are other factors apart from substrate temperature and roughness (such as temperature, velocity and size distribution of the incident particles) that also influence the structure of a coating. This type of coating is widely used on a commercial scale. The splat boundaries and microcracks that run approximately parallel to metal/ceramic interface in APS TBCs are highly efficient in reducing the thermal conductivity of APS TBCs. However, the splat boundaries and microcracks are a source of weakness in APS TBCs, limiting the service life of the coatings and potentially leading to early spallation. Splat structure can be seen in Figure 2-9.

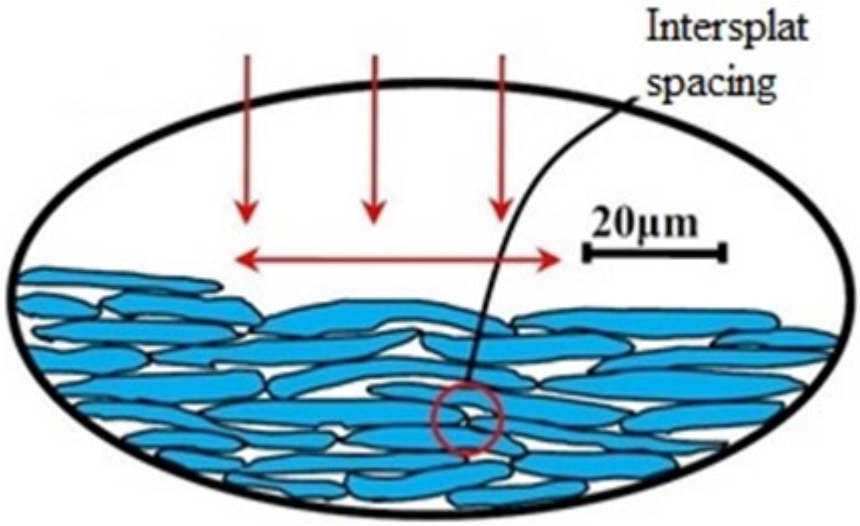

Figure 2-8 Schematic Illustration of APS splats (modified from [73])

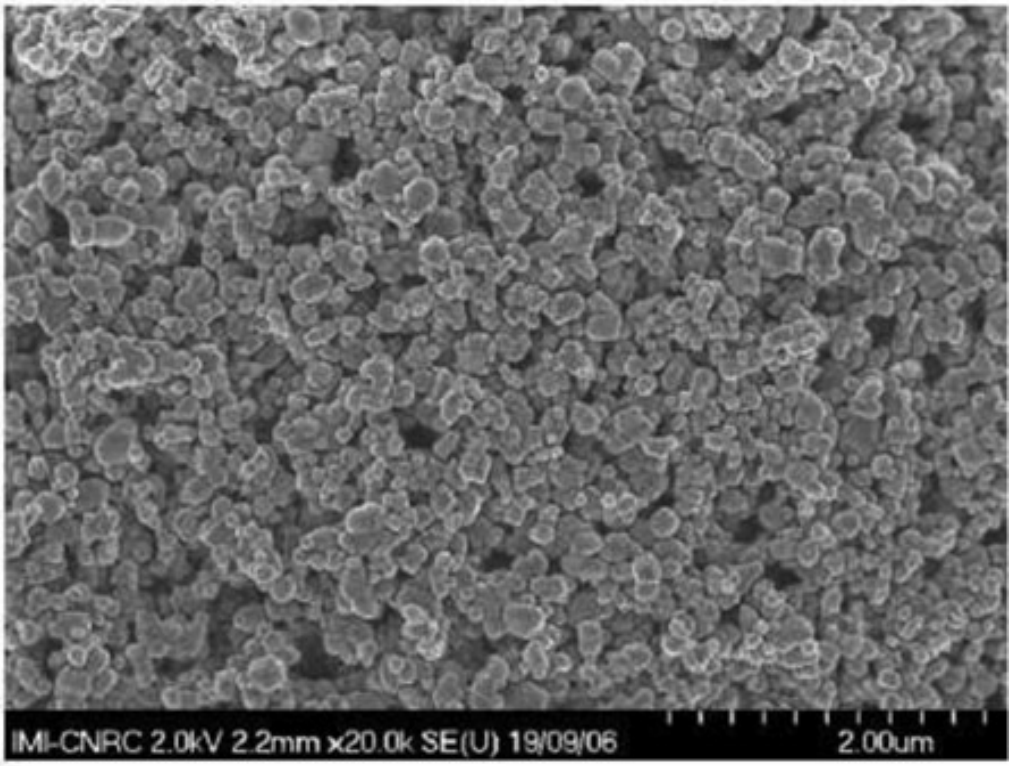

Figure 2-9 SEM of Air Plasma Sprayed TBC [74]

The nature of the synergy between the plasma gas and ceramic feedstock plays a crucial role in determining the properties of an APS-deposited TBC. This follows because the TBC is created by thousands of individual solidifying particles per mm^3 after experiencing a hot plasma environment [75]. The thermal conductivity of APS TBC can be achieved to near about 0.8-1.1 W/mK [76]. The effective thermal conductivity of the porous air plasma sprayed TBCs is strongly dependent on structure, such as pores, cracks, pore/coating interface, crack/coating interface, and layer interface. Besides the scattering effect at the defects or interfaces, the interface thermal resistance (ITR) is another important factor which will affect the eventual effective thermal conductivity of the APS-TBCs [73].

Electron Beam Physical Vapour Deposition

EB-PVD is a popular processing technique for ceramic top coats, where the coatings are formed by vapour condensation and are characterized by a columnar microstructure with defects such as cracks and grain boundaries which run normal to the ceramic-metal interface [77]. The vapours are produced with an electron beam by melting and evaporating the ceramic placed in a crucible under the workpiece. EB-PVD is performed in a vacuum chamber. Vacuum chambers avoid contamination of molten material in the crucible and/or the vapour phase of the condensate (coating). Ideally, individual ceramic columns are poorly bonded to adjacent columns, but the bonding between the coating and underlying substrate is stiff [78].

The extremely fine columnar structure of EB-PVD is highly tolerant to strains induced during the expansion of the underlying substrate [79]. In this process, a high-energy electron beam is used to heat and vaporize the ceramic feedstock. The vapour travels perpendicular to the substrate on which it condenses atom by atom [80]. For zirconia-yttria ceramics, the low partial pressure of oxygen is maintained during the process in order to preserve the stoichiometry of zirconia. In the EB-PVD case, the interface between the bond coat and top coat is smooth in comparison to plasma sprayed coatings.

The structure of EB-PVD is shown in Figure 2-10. The microstructure of EB-PVD coatings exhibits improved strain tolerance and thermal shock resistance, which significantly enhances their lifetime. The EB-PVD TBC can be used without spalling on highly stressed gas turbine engine components having higher operating temperatures or greater thermal gradients. The columnar growth is believed to reduce the elastic modulus in the plane of the coating to approximately near zero.

Usually, the operating temperature lies between room temperature and above 1200^{o}C [81]. The factors affecting the thermal protection are mostly the thickness of the coating,

internal coolant flow rate and cooling efficiency, and the heat flux of the impinging hot gases. Overall thicker coatings are used for higher heat flux to attain the given temperature difference ΔT [17].

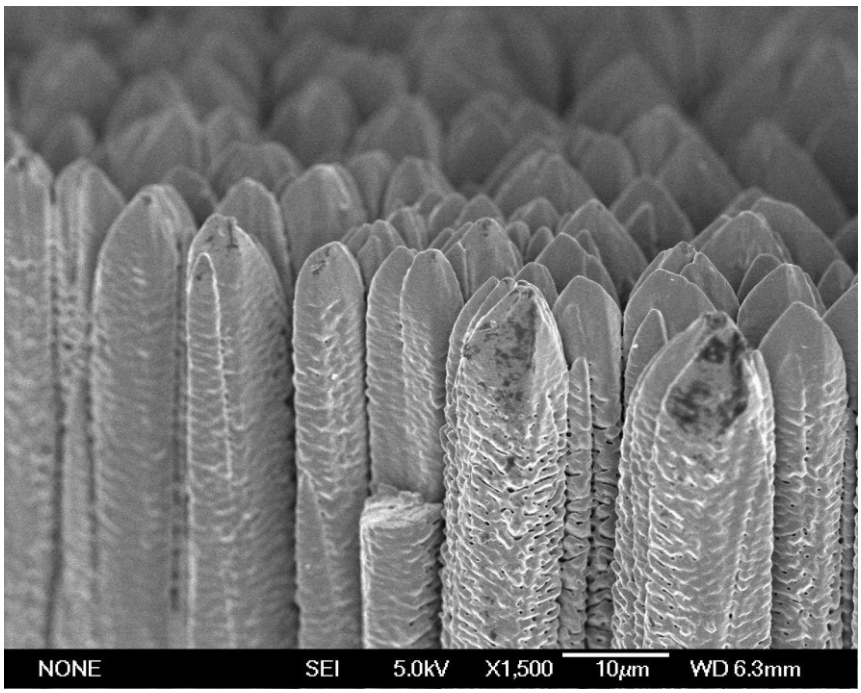

Figure 2-10 SEM of EB-PVD TBC [82]

The negative aspect of EB-PVD coating is related to its microstructure. The TBCs prepared by EB-PVD often exhibit columnar grain structural characteristics, where the pore channel between the columnar grains is often parallel to the thermal flux direction (Figure 2-12). This results in an effective thermal conductivity that is often higher than that of APS-TBCs [83].

The EB-PVD TBC has some better properties as compared to plasma sprayed TBC. The surface finish of EB-PVD coatings dominates over the APS coatings. The columnar structure of EB-PVD coatings produces excellent strain tolerance properties. Due to the capability of stress relaxation at elevated temperature, EB-PVD coatings are more resistant to erosion. The coating microstructure is an important factor in determining the behaviour of the coating during its service life.

Thermal and mechanical properties of coatings are easier to control with the EB-PVD process. A schematic of the EB-PVD coating process can be seen in Figure 2-11. During the EB-PVD process, the vapour is created by heating the source material with a beam of electrons, and the evaporated atoms gradually condense on the substrate. The crystal nuclei form at favoured sites and grow both laterally and along the thickness to form individual columns, which yield a high inter columnar porosity [85].

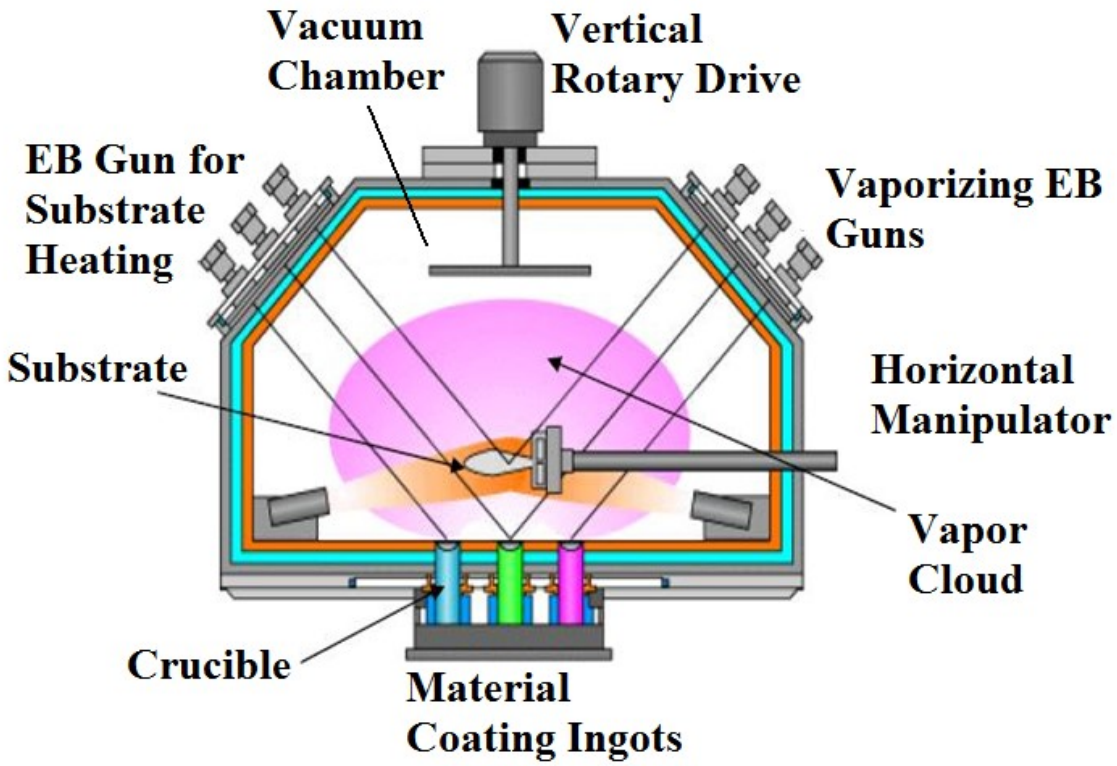

Figure 2-11 Schematic of EB-PVD Process [84]

However, APS-TBCs often exhibit lamellar structure with a lot of ellipsoid pore structures, so that the effective thermal conductivity is usually lower than that of a perfect TBC. Hence, it is very important to control the pore volume fraction, spatial distribution, orientation and morphology to obtain TBCs with optimized or reduced thermal conductivity. The porous,

microcracked columnar EB-PVD ceramic structures provide progressively increasing coating durability [86].

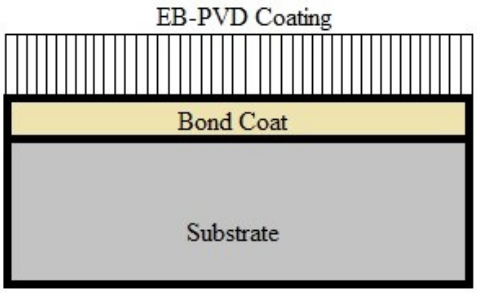

Figure 2-12 Schematic Illustration of EB-PVD coating

A simple comparison between the air plasma sprayed and electron beam physical vapour deposition is shown in Table 2-1. These two TBCs are compared on ten different parameters. These parameters define the areas where the coatings will be more beneficial.

Table 2-1 Air Plasma sprayed (APS) versus on-evaporated EB-PVD TBCs

	APS	**EB-PVD**
Surface Finish	Good but extra polish	Excellent
Bond Coat Roughness	Grit Blasted	Smooth
Bonding Mechanism	Mechanical and Chemical	Chemical
Alloy Flexibility	High	Limited
Typical Thickness	0.2-3mm	0.1-0.3mm
Cooling Hole Closure	Poor	Excellent
Coating Source	Moveable	Fixed
Large Part Predicable	Favourable	Costly
Parts per Charge	1	1-10
Investment Cost (%)	100	100-400

2.4 Thermal conductivity of coatings

Thermal conductivity is the property of a material to conduct heat and can be considered as the rate at which heat passes through a specified material. Heat is transferred at a lower rate for a material with a low thermal conductivity. The thermal conductivity of coatings depends on the method of depositing the coating [20], [35], [87] since the microstructure changes according to the coating deposition technique. The most widely-used techniques for depositing coatings are plasma sprayed and electron beams physical vapour deposition techniques. Microstructural properties such as micro-cracks, grain size, pores and their distribution, impurities, and voids have an adverse impact on the thermal conductivity of the coatings.

Plasma sprayed thermal barrier coatings currently offer a thermal conductivity in the range of 0.8-1.1 W/mK, while electron beam physical vapour deposition coatings offer thermal conductivity in the range of 1.5-1.9 W/mK. Both techniques provide a thermal conductivity range that is much smaller than that of the Bulk YSZ (2.2-2.9 W/mK) [88]. Plasma sprayed coatings are more porous than EB-PVD coatings and this serves to reduce the thermal conductivity of APS coatings [89]. The comparison between the thermal conductivity of bulk zirconia, EB-PVD and APS coating can be seen in Figure 2-13. The thermal conductivity of a porous ceramic layer depends on the intrinsic thermal conductivity of the bulk ceramic, which is linked to its composition, structure and on the architecture of the porous structure i.e. pore volume fraction, geometry and distribution [90].

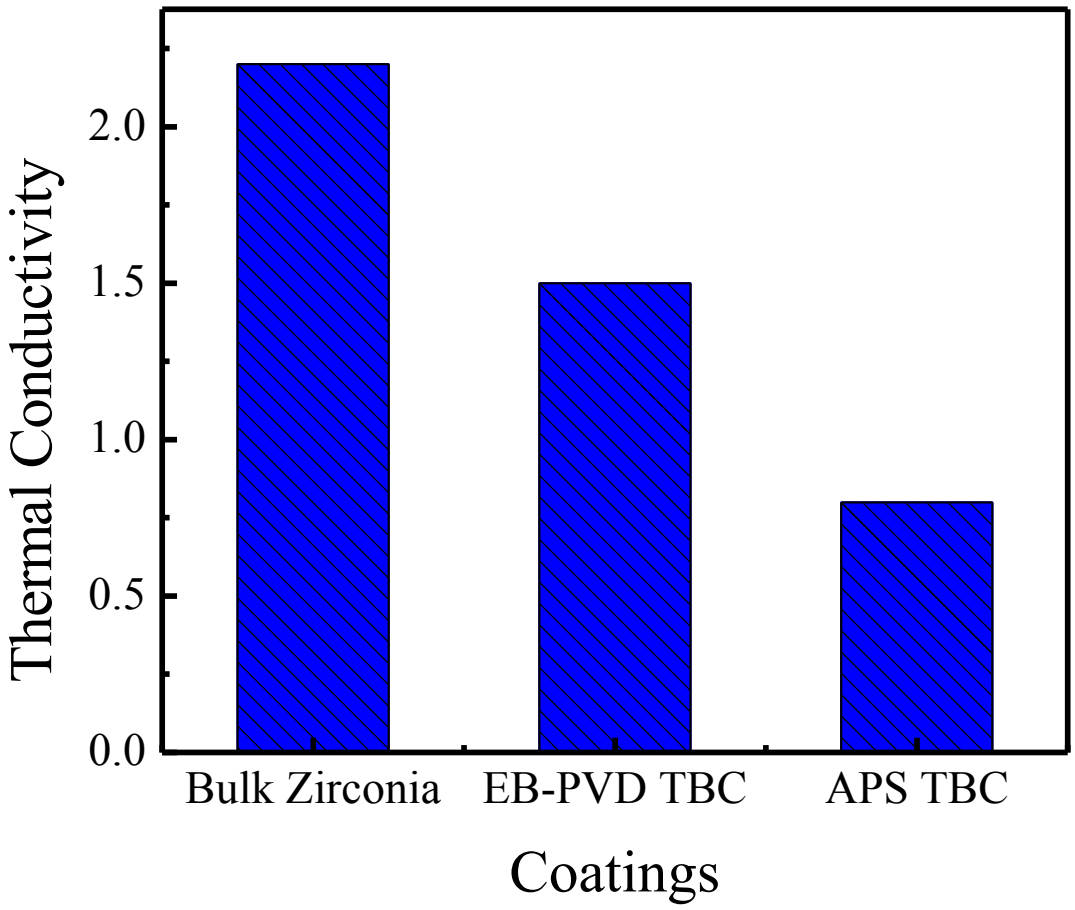

Figure 2-13 Thermal conductivities of different processes compared to bulk (reconstructed from [88]).

2.4.1 Methods to measure thermal conductivity

Design of a TBC can be evaluated using several material properties including thermal conductivity. For high-temperature protective coating, lower thermal conductivity is most desirable, along with a higher coating stability. To measure these properties several measuring techniques are used. A common and simple method to determine the thermal conductivity of an unknown material is discussed below.

To calculate thermal conductivity of materials, the guarded heat plate method is used [91]. In this method, a sample is placed between two plates, one plate acts as a heat source and

the other plate acts as heat sink. The transfer through a sample having cross-sectional area A, having thickness L can be calculated. The formula for thermal conductivity is then given by

$$k = \frac{Q.L}{A.\Delta T} \tag{2.3}$$

where Q (W) is the heat load on the sample, L (m) is the length of the sample, A (m^2) is the cross-sectional area to which heat is applied, and ΔT (K) is temperature difference across the sample top and bottom. For this process, the cross-sectional area is measured using a Vernier calliper. The heat load Q is calculated from the measurement of the voltage across the sample. The sample is clamped between the copper sample holder. Temperature sensors are placed on the sample using varnish. A dual-twist phosphor/bronze lead wire is wrapped around the sample to ensure better thermal conductance to the sensor. Heat flows from top to bottom of the sample. Testing is mostly done in a vacuum to avoid heat leaks. The temperature of each sensor and the current and voltage of heater coils are collected. Using these values, thermal conductivity is calculated.

The guarded heat plate method is suitable for cold samples. However, for thermal coatings, there is a need to calculate thermal conductivity at elevated temperatures. Hence, a different technique is used. Laser Flash Analysis (LFA) is a technique accepted for evaluating thermal conductivity of TBCs at any temperature [92]. In this method, a laser pulse is shot at the substrate face of the sample and the resulting temperature increase is measured at the other face of the sample with an infrared detector. The signal is then normalized and the thermal diffusivity is calculated using an equation based on one of the existing models. One such equation is given by

$$\alpha = (0.1388L^2) / t_{(0.5)} \tag{2.4}$$

where α (m^2/s) is the thermal diffusivity, L (m) is the thickness of the sample and $t_{0.5}$ (s) is the time taken for the rear face of the sample to reach half of its maximum rise.

Thermal conductivity K (W/m.k) can then be calculated if the density (ρ) and specific heat capacity (C_p) of the coating are known via

$$k = \alpha.C_{p.}\rho \tag{2.5}$$

This technique has a few requirements for measuring the thermal conductivity of YSZ coatings, such as the zirconia must be coated with a thin layer of gold or graphite. The reason for this is that zirconia is translucent to light in the operating wavelength of the laser [93]. The coating prevents the laser from passing through the zirconia ceramic layer. A major drawback is that only small flat samples can be used for measurement and thus measurement on a real component is not possible [94].

2.5 Heat transfer mechanism

Thermal conductivity is attributed to the thermal transport property of coatings. This property is an important design parameter for thermal barrier coatings and is an important factor in determining the coating performance [95]. The thermal conductivity of ceramic coatings is significantly affected by the intrinsic attributes of the material and the extrinsic characteristics (microstructural defects, oxidation and temperature) [25],[96].

The thermal conductivity is affected by temperature changes in the material [97]. For a material such as YSZ, there is a variation in the dominant mechanism of heat transport that occurs at high temperatures. There is a reduction in thermal conductivity of YSZ from room temperature to about 800^{o}C because the scattering of phonons (phonons density increases at high temperature and they collide with other phonons and reduces the mean free path) becomes more pronounced with rising temperature (in the case of Zirconia coatings). As the temperature

of Zirconia based coatings increases, the phonon-phonon interaction also increases. This results in deflection of phonons from straight paths. A rise in temperature results in a reduction of the mean free path. As the mean free path decreases, the thermal conductivity of Zirconia coatings also decreases. The temperature dependent thermal conductivity of YSZ is shown in Figure 2-14. The thermal conductivity is limited by intrinsic phonon scattering scales as *1/T* [98]. At higher temperatures, photon conduction (radiation) becomes increasingly important and results in a faster elevation of thermal conductivity (proportional to T^3) (in the case of Zirconia coatings) [99].

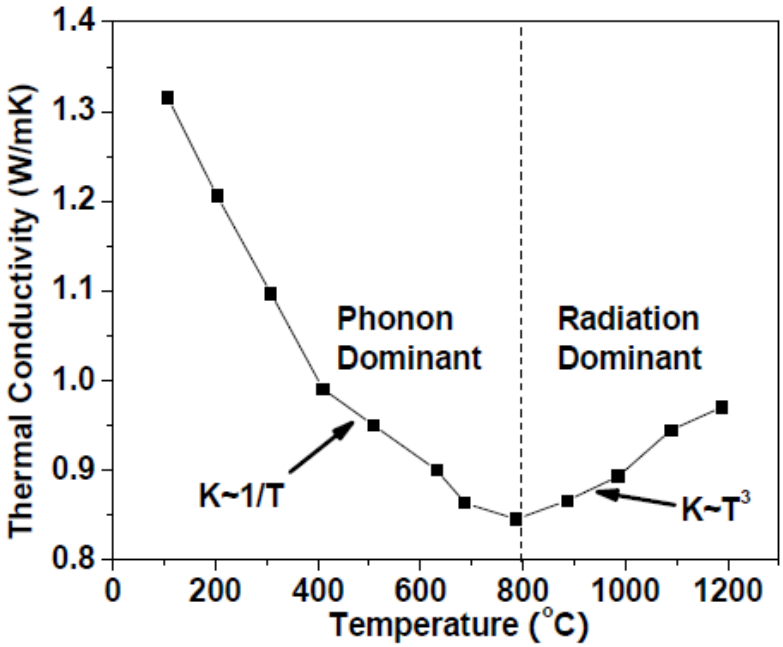

Figure 2-14 Temperature-dependent thermal conductivity of YSZ [25]

Heat transfer can be categorised using the basic mechanisms of conduction, radiation and transfer of energy by phase change. These mechanisms are based on phonon and photon interactions with surroundings. The thermal conductivity of the as-sprayed TBCs (mainly for APS) is dependent on certain molecular interactions. There are five different types of interactions that are represented in Figure 2-15.and are:

- The phonon conduction, which is caused by the crystal lattice vibration [F1]

- The radiation scattering at grain-boundaries [F2]
- Knudsen conduction, which is induced in the inter-splat interface [F3]
- Gas phase conduction [F4]
- Radiation scattering at all kinds of interfaces, such as the splat interfaces, and the interfaces between the coating and defects [F5].

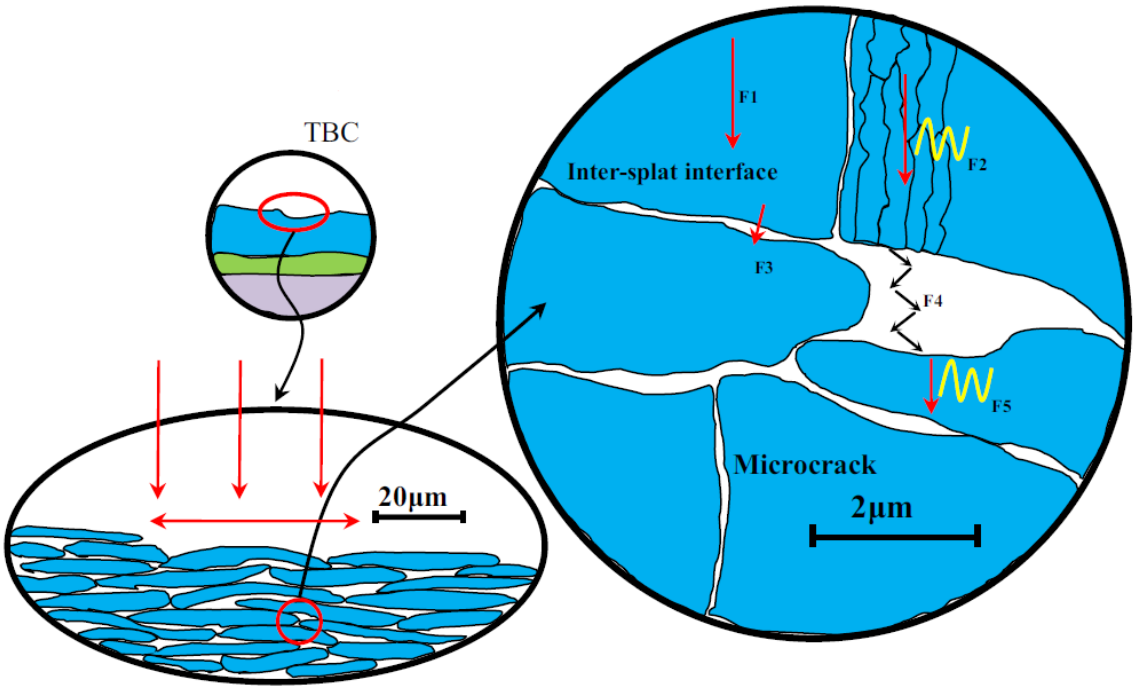

Figure 2-15 Heat transfer mechanism in thermal barrier coatings [73]

These interactions are not always present in all types of coatings. The microstructure of a coating influences the heat transfer mechanism. Zirconia and its alloys are electronic insulators due to a lack of free electrons. Electrons play no part in the total thermal conductivity of the system, consequently, heat transfer in zirconia is governed by lattice vibrations (phonons) or by radiation (photons). The dominant role in heat transfer is played by phonon conduction. The total thermal conductivity (K) of ceramic materials [100], which is the sum of three components, can be expressed in a general form as

$$k = \frac{1}{3}\sum_{j=1}^{N} C_{pj} v_j l_j \tag{2.6}$$

where N is the total number of energy carriers, v is the carrier's velocity (group velocity if the carrier is a wave), C_p is the specific heat at constant pressure and l is the corresponding mean free path. The electron mean free path has two parts. Some part is the residual mean free path, which is related to the scattering of electrons by defects and the other is intrinsic mean free path, which is related to the scattering of electrons by lattice vibrations. The residual mean free path is independent of temperature while the intrinsic mean free path is directly proportional to temperature. The contribution to thermal conductivity from just the lattice vibration (k_p) is given by [88]

$$k_p = \frac{1}{3}\int C_v \rho v l_p \tag{2.7}$$

where C_v is the specific heat, ρ is the density, v is the phonon velocity and l_p is the mean free path for the scattering of phonons. In the case that no defect is present and with a high-temperature limit, three-phonon interactions limit the mean free path of phonons, owing to the cubic anharmonicities of the lattice forces. This expression then leads to the following expression of the intrinsic thermal conductivity [101] given by

$$k = \frac{3}{2}\gamma^{-2}.(\frac{\mu v^2}{\omega_D})T^{-1}.N^{\frac{-2}{3}} \tag{2.8}$$

where γ is the Gruneisen constant, μ is the shear modulus, v is the transverse sound velocity, ω_D is the Debye frequency, T is the temperature and N is the number of atoms per primitive unit cell. The Gruneisen parameter, γ, is a valuable quantity in solid-state geophysics because it can be used to set limitations on the pressure and temperature dependence of the thermal properties of the mantle and core, and to constrain the adiabatic temperature gradient. It is dimensionless and, for a wide range of solids, has an approximately constant value, varying only slowly with pressure and temperature [102].

At higher temperature, the thermal conductivity of ceramics increases with temperature owing to the photon heat transfer (radiation conduction). The thermal conductivity contribution due to radiation can be written as [103]

$$k_r = \frac{16}{3}\pi\sigma n^2 T^3 l_r \tag{2.9}$$

where k_r is the thermal conductivity due to radiation, σ is the Stephen–Boltzmann constant, n is the refractive index, T is the absolute temperature, and l_r is the mean free path for photon scattering. From this equation, the thermal conductivity of ceramics at higher temperature became a function of T^3. The total theoretical thermal conductivity of zirconia-based systems is the sum of thermal conductivity by photon transport and thermal conductivity by phonon transport and is given by

$$k = k_r + k_p \tag{2.10}$$

At temperatures below 1200°C, phonon transport dominates the heat conduction through zirconia. However, as the temperature is increased, radiation becomes more significant (a 10% contribution at 1250°C) [88]. In real crystal structures, a scattering of phonons occurs with the interaction of phonons with lattice imperfections. Such imperfections include dislocations, vacancies, voids, grain boundaries, ions, atoms of differing ionic radius or atoms of different masses and other phonons [104]. Scattering can be caused by locally distorting the bond length and thus introducing elastic strain fields into the lattice. The effects that such imperfections cause can be quantified through their influence on the phonon mean free path (l_p). The phonon mean free path can be described using [88]

$$\frac{1}{l_p} = \frac{1}{l_i} + \frac{1}{l_{vac}} + \frac{1}{l_{gb}} + \frac{1}{l_{strain}} \tag{2.11}$$

where l_i, l_{vac}, l_{gb} and l_{strain} are the contributions to the mean free path due to interstitials, vacancies, grain boundaries and lattice strain, respectively. There may be a significant effect of grain boundaries in nanostructured coatings [23]. The intrinsic lattice structure and strain fields have a significant effect on both conventional materials and coated structures.

2.6 Effect of different parameters on thermal conductivity of thermal barrier coatings

Thermal conductivity is one of the key material property that can be influenced by even minor changes in the material microstructure or composition. In this section, the influence of these parameters that can affect the thermal conductivity of coatings is discussed.

2.6.1 Impact of yttria content on thermal conductivity

The impact of microstructural properties on the thermal conductivity of zirconia-based coatings is significant [105]. These microlevel changes are attributed to the process parameters used for the different coating techniques. Each of these processes has a significant impact on coating morphology and structure. APS coatings have a more splat-like structure while EB-PVD coating has a columnar structure. With enhancement in process parameters, coatings can be deposited that have a thermal conductivity lower than bulk materials.

Bulk zirconia has a thermal conductivity in a range of 2.2-2.8 W/(m.K). On the other hand, yttria-stabilized zirconia (YSZ) based coatings have a lower thermal conductivity of approximately 0.8-1 W/(m.K) [98]. This change in thermal conductivity is dependent on the percentage of yttria content present in the coatings, along with some other factors such as deposition technique or heat treatment. The reduction in thermal conductivity with the addition of yttria is commensurate with a shorter intrinsic mean free path due to local modifications of the lattice structure, and the introduction of vacancies and local strain fields generated by

incorporating large dopant atoms. These strain fields and vacancies act to scatter phonons, directly increasing phonon dispersion in the lattice. With increased dispersion, there is a high probability that phonon-phonon interactions will occur whereby the mean free path will be further reduced. The higher the yttria content, the lower the thermal conductivity of the coating [104].

Srinivasan et al. suggested that at a given temperature, the reduction in thermal conductivity with higher yttria content is consistent with oxygen vacancies playing the dominant role in phonon scattering [105]. Figure 2-16 describes the effects of yttria content on the thermal conductivity. Figure 2-16 depicts that a monoclinic phase with 0 wt% yttria content has the highest thermal conductivity. The tetragonal phase with 5.3-5.8 wt% yttria has an intermediate thermal conductivity value. A relatively large drop in conductivity can be seen from 5.8 to 8wt.% yttria for cubic phase. Further increase in yttria content to 15wt.% from 5.8wt% does not cause a proportionate decrease in thermal conductivity.

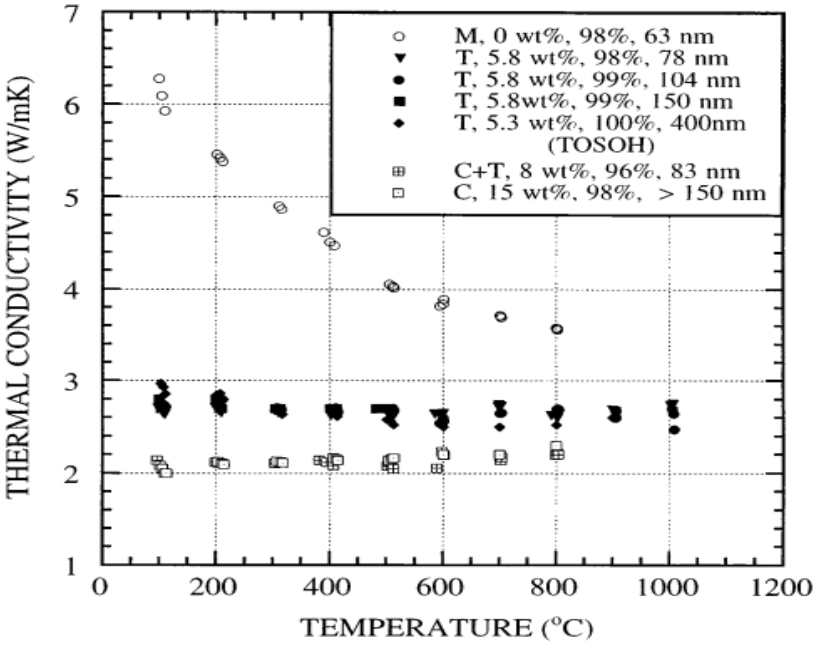

Figure 2-16 Effect of yttria content on thermal conductivity [105].

2.6.2 Effect of Defects on the thermal conductivity of ceramic coatings

The thermal conductivity of an insulator can be lowered in an efficient way by introducing structural defects which constitute obstacles to the propagation of phonons [106]. Several types of defects may be envisaged such as vacancies, voids, cracks, pores, substitution ions, dislocations, interfaces (grain boundaries), etc. The role of vacancies is particularly important in this respect for zirconia-based materials [107]. As nanostructured TBC have many grain boundaries, phonon scattering will enhance significantly. In addition, the existence of nano and micron pores, oxygen vacancies [108] and solute atomic point defects in the nanostructured TBC, can possibly enhance the phonon-scattering effect, which makes the insulation effect of the nanostructured TBC improve significantly. A special kind of lattice defect is a vacancy, which is the total absence of mass (as shown in Figure 2-17) and a mismatch of volume on the crystalline sites, as well as the surrounding chemical bonds.

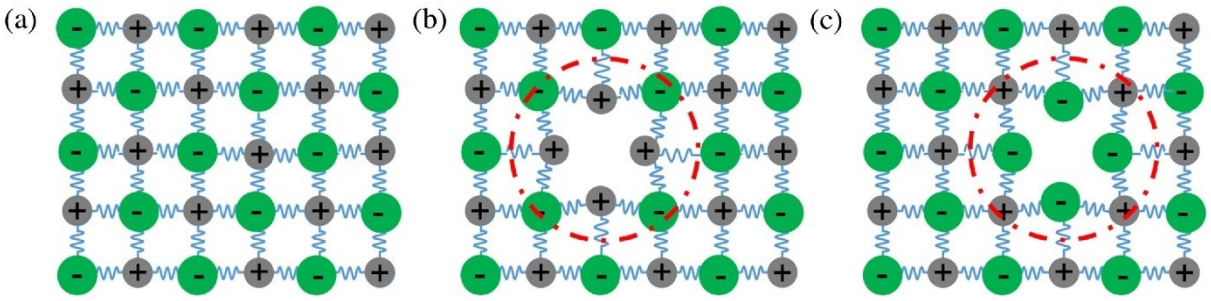

Figure 2-17 Schematic drawings of (a) perfect crystal lattice without vacancies; (b) defective lattice with anion vacancies; (c) defective lattice with cation vacancies. [55]

This leads to the strongest phonon scattering and lattice distortion. This distortion leads to further scattering. An increase in the concentration of the vacancies will surely result in a lower thermal conductivity.

Pure zirconia is treated as unusable because of its undesirable transformation at elevated temperatures around 1100°C. Zirconia is stabilised either partially or fully by adding hetero elements (most often Y, Mg, Ca) which stabilise the cubic (or the tetragonal phase). The cubic form of zirconia can be fully stabilized by the addition of 20 wt.% Y_2O_3 in the Zirconia. The metastable t' phase can be achieved by adding 6 to 8 wt.% Y_2O_3. Different phases and phase diagram are shown in Figure 2-18. The electrical neutrality of the ionic lattice is maintained by incorporating the hetero elements accompanied by the introduction of vacancies. Incorporating hetero-elements such as Ca, Mg or Y lowers the thermal conductivity of zirconia.

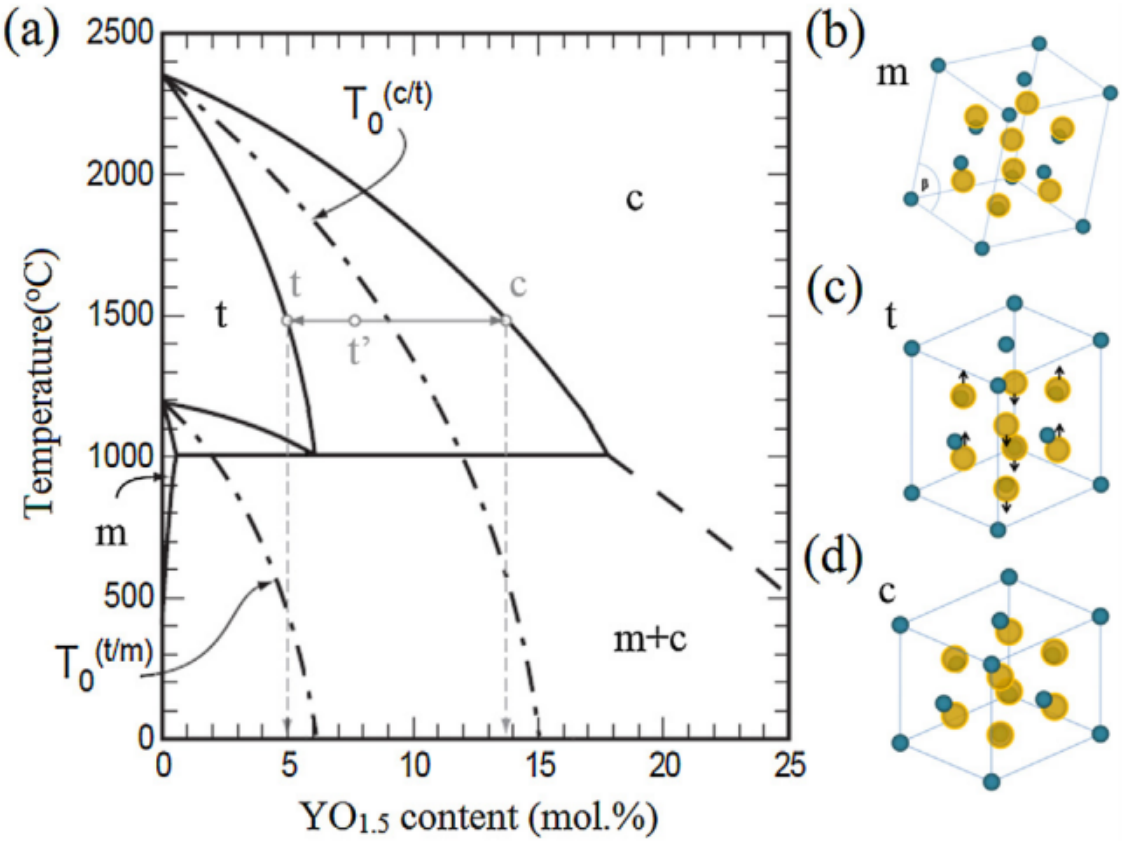

Figure 2-18 (a) The ZrO_2-rich part of the ZrO_2-Y_2O_3 binary phase diagram, (b) the lattice structure of the m phase, (c) t phase and (d) c phase of ZrO_2 [55]

The assessment of diffusivity measurements on zirconia with several types of stabilisers indicates that analogous defect populations result in comparable thermal diffusivity [109].

Some previous studies on different effects of defects

In the case of pure solids, the phonon thermal conductivity during the absence of any extrinsic scattering by extended defects (grain boundaries, pores) or point defects (vacancies, solute atoms), is given by the equation (2.8). Phonons interact strongly with a population of randomly distributed defects rather than ordered vacancies. Some of these defects can be seen in Figure 2-19. Wei et. al calculated the influence of pore radius and crack length on effective thermal conductivity with the aid of finite element method (FEM) and analytical calculation. The effect of defects on the effective thermal conductivity of TBCs is expressed as [110]

$$K_{eff} = K_0\left(1-\frac{D}{hl}\right) \tag{2.12}$$

where K_{eff} is the effective thermal conductivity, K_0 is the thermal conductivity of the non-defective bulk material, D is the influence parameter of defects on the effective thermal conductivity, h is the height of sample, and l is the width of the sample (as in Figure 2-20).

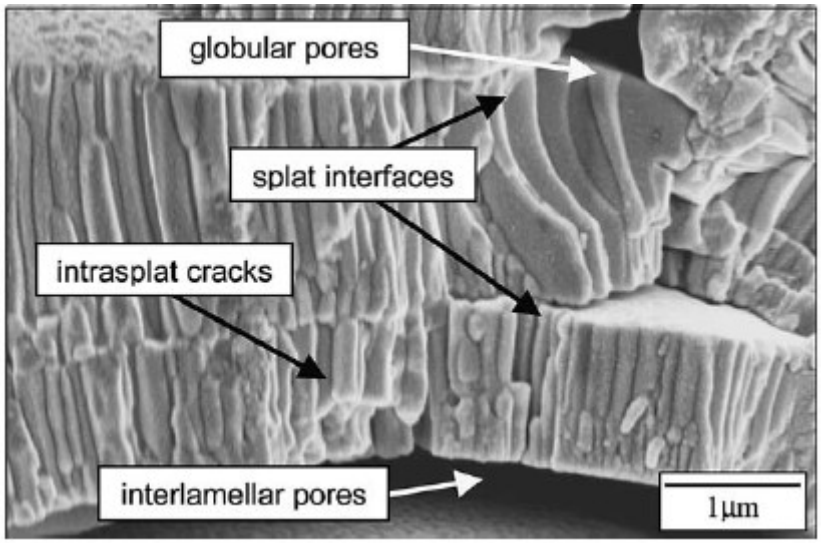

Figure 2-19 Various types of defects in a PSZ coating [111]

Influence parameter is expressed as [110]

$$D = \rho.hl + \sum_{i=1}^{n} C_K(i) \tag{2.13}$$

where ρ is the porosity, n is the number of cracks, C_K is an independent variation of the thermal nonlinear area around the defect, which is only affected by the defect. C_K of the pore with radius a is fitted as $C_K = \alpha.a^2$, C_K of a transverse crack with length $2b$ is fitted as $C_K = \beta b^2$. The longest transverse crack plays the most important role in determining the effective thermal conductivity along the spray direction, more than any individual defect [110].

Grain boundaries [112] and interfaces [73] can also scatter phonons and reduce the thermal conductivity. Effect of phonon scattering at the grain boundaries is most effective at low temperature for ceramics in general [112], and only slightly at high temperature.

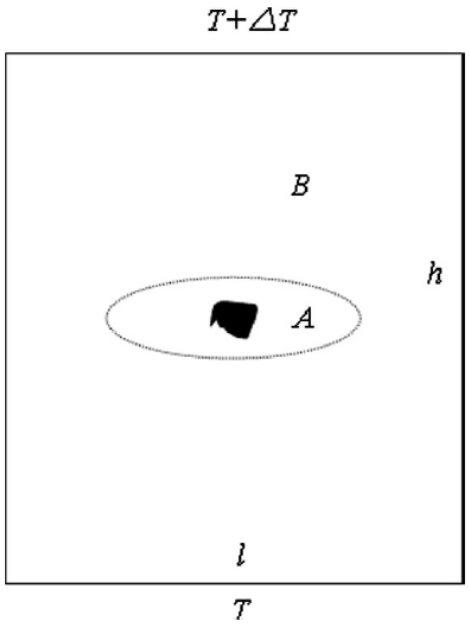

Figure 2-20 TBCs plate with defect inside subject to a temperature difference load

The study conducted by Mao et. al. [113] deduced the decrease in thermal conductivity for InSb with increasing temperature. With the results from Figure 2-21, it can be clearly seen that grain size and grain boundaries have an effect on phonon scattering.

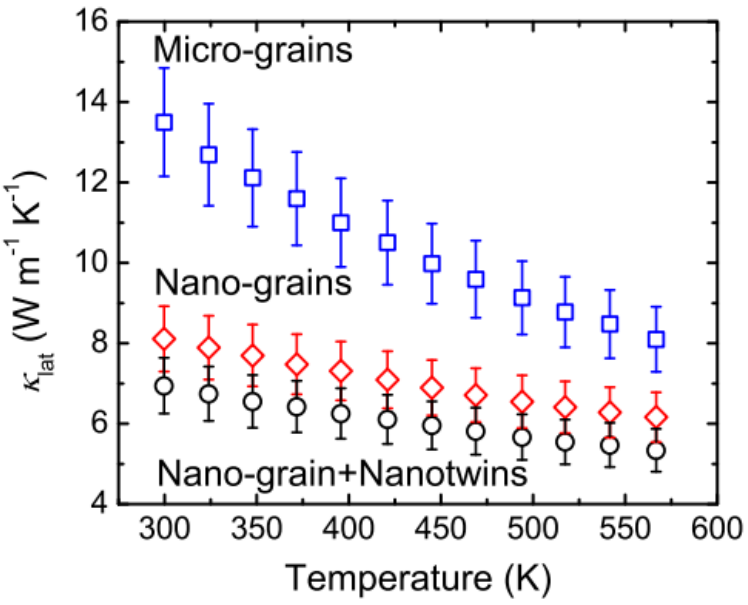

Figure 2-21 Comparison of lattice thermal conductivity κ_{lat} between different InSb specimens [113]

Yang et.al performed finite element simulations on various shapes of defects (see Figure 2-22) to analyse the effect of thermal erosion [114]. The influence of pore shapes on the distribution of coating temperature, *x* component of stress, y component of stress, *xy*-shear stress and von-Mises stress were the focused of this study. The simulation results indicate that different pore shapes not only affect the thermal stress distribution above the contact area between the bond coating and top coating surface but also affect the plastic deformation behaviour of TBCs.

Shapes	Up-triangle	Down-triangle
geometry		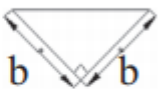
Size (mm) Area (mm^2)	a=0.12533 0 0.007854	b=0.12533 0.007854

Square	Bias-square	Circle
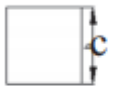		
C=0.08862 0.007854	d=0.08862 0.007854	r=0.05000 0.007854

Figure 2-22 Different shapes modelled in Yang et. al research work [114].

Another result was obtained during this work. The change in temperature drop with an increase in porosity content was calculated. The results are shown in Figure 2-23.

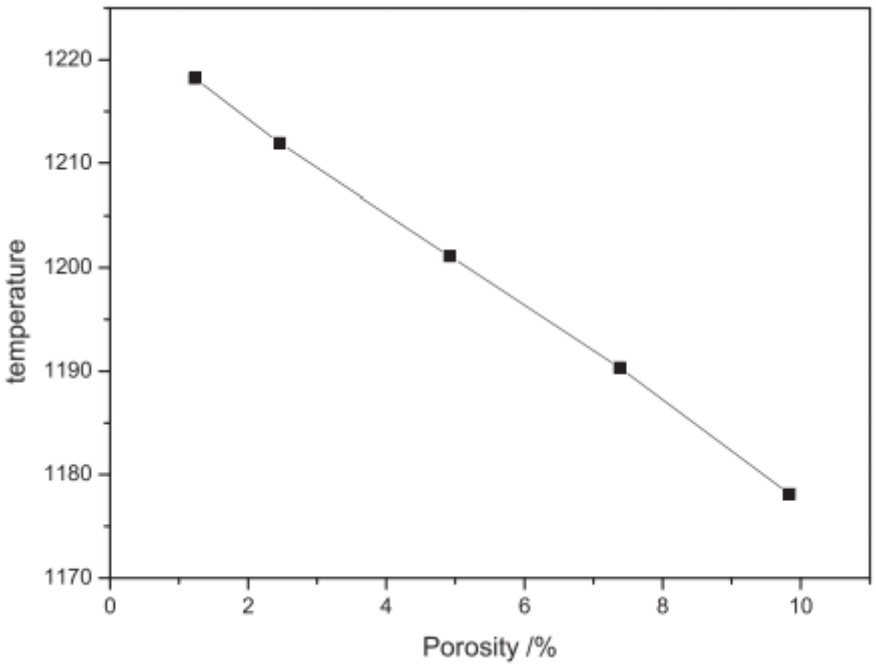

Figure 2-23 Temperature drop with increasing porosity content [114].

Meng and Wei studied the evolution of lattice structure and thermal conductivity for a range of Ti-doped, Y_2O_3-stabilized ZrO_2 (YSZ) solid solutions [115]. They studied the mechanism to reduce the thermal conductivity by Ti doping. The results of their study can be seen in Figure 2-24.

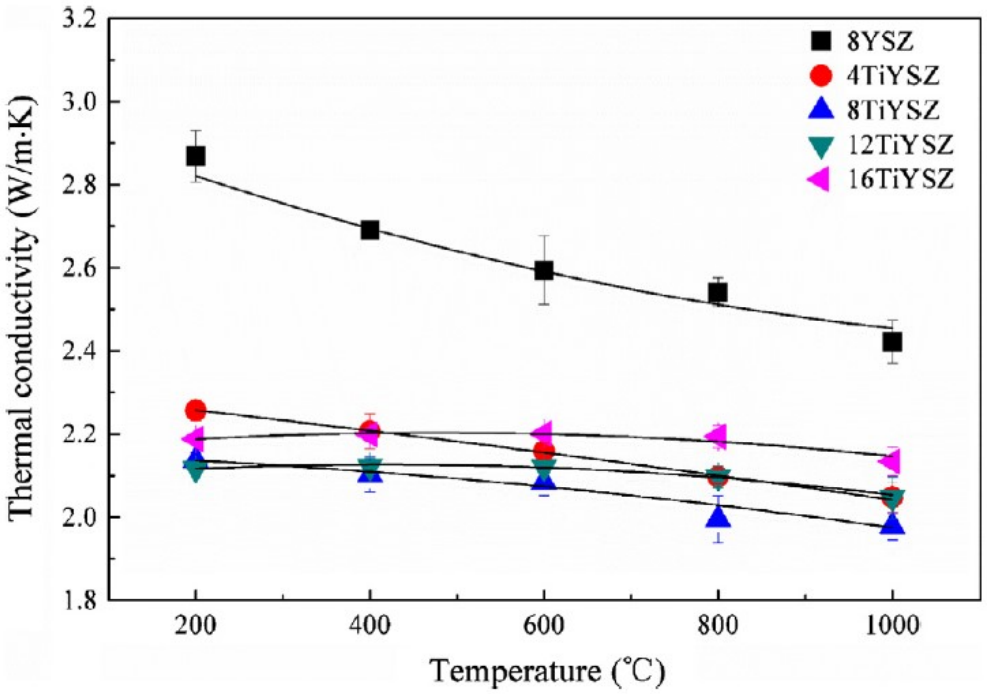

Figure 2-24 The thermal conductivity of the specimens as a function of temperature [115]

Common results obtained on the effect of defects are in [19], [55], [98], [110], [111], [115], [116] and include:

- Generally, the pores/defects account for 40–75% of the reduction in the effective properties (thermal conductivity and effective modulus, E), depending on the feedstock and the fabrication process.
- The most important parameters that affect thermal conductivity are grain contact surface area, volumetric density of macro and micro-cracks, and porous boundaries.
- There is an increase in the thermal insulation effect of TBCs with the increase in the size of pores (pores distributed in the ceramic coating). The strength of the coating must be the basis in order to increase the size of pores of the TBCs.
- Surface pores will increase thermal conductivity.
- Different shapes of pores have different effects on thermal conductivity when the overall area of the pores is fixed.

- There is a reduction in the intrinsic thermal conductivity due to phonon scattering by point defects (oxygen vacancies).
- Substitutions offer another route for phonon scattering that leads to the reduction in thermal conductivity.

2.6.3 Effect of coating structure on thermal conductivity

The thickness of YSZ coatings plays an important role in defining the total thermal conductivity, especially for the coatings deposited by the EB-PVD technique due to the fine microstructure of coating near the base. Thickness also affects thermal conductivity because of the microstructural changes across the coating thickness. These changes are roughly characterized by the grain size in the coating. Coatings have an inner zone with a fine-grained structure and an outer zone with coarse-grained microstructure [117]. The inner zone has numerous grain boundaries while the columnar structure at the outer zone becomes coarser and the number of oblique columnar boundaries decreases. Thinner coatings have lower thermal conductivity (due to fine-grained particles that increase grain boundary effect) as compared to thick coatings [117] due to the fact that the columns and the elongated intercolumnar porosity become predominantly aligned perpendicular to the plane of the coating as its thickness increases. The thermal conductivity of the inner zone is dominated by phonon scattering at the defect or grain boundaries.

The thermal conductivity of a thick coating with a thickness of about 300μm is about 40% higher than that of thin coatings of about 50μm [117]. Table 2-2 illustrates the difference between the thermal conductivity of thin film and bulk materials. The fabrication process is different for both types of coatings. There will be different properties based on the fabrication process. The difference can be clearly seen in the thick and thin coating materials.

Table 2-2 Comparison of Thermal Conductivity of thin films and bulk materials

Material	Thermal conductivity of Thin Films (W/mK)	Thermal conductivity of Bulk Material (W/mK)
Glassy SiO_2	0.12	1.3
TiO_2	0.6 (evaporated) 0.5(sputtered)	5.5-7.6 (rutile)
ZrO_2	0.8	2-5
AIN	16	70-220(polycrystalline)

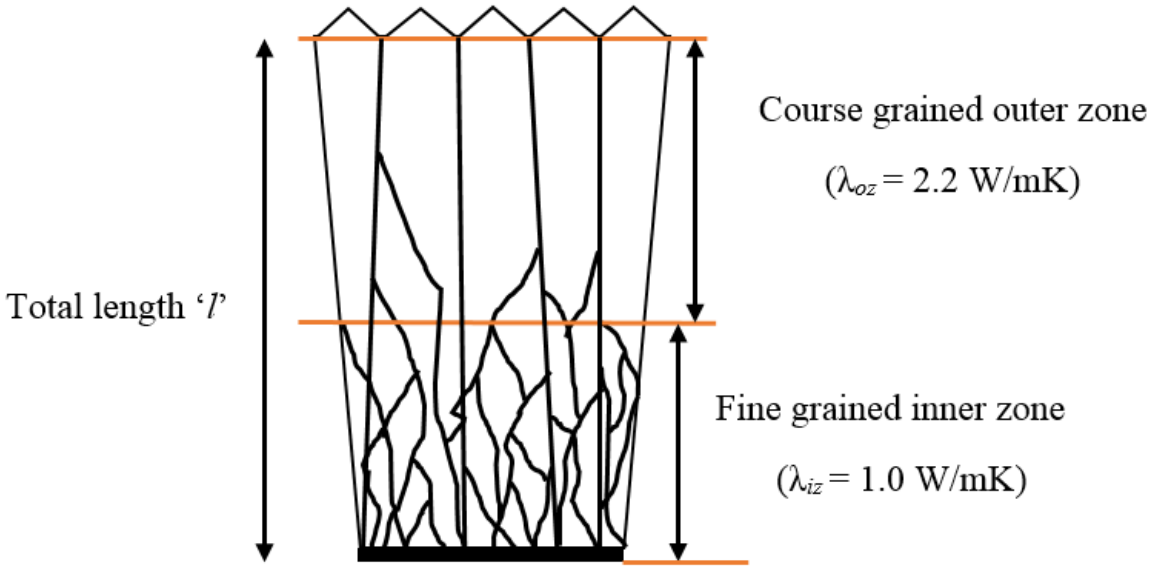

Figure 2-25 Structure of EB-PVD Coating showing two separate zones of Fine and Coarse grains [117]

Fine-grained materials tend to have a lower thermal conductivity. For instance, when the grain size is of nanometre dimensions [88], the value of 0.7 W /(m.K) is predicted. The structure of a two-layered EB-PVD coating is presented in Figure 2-25. The total thermal conductivity of two-layer coating can be obtained as

$$\frac{l}{\lambda} = \frac{l_{iz}}{\lambda_{iz}} + \frac{l_{oz}}{\lambda_{oz}} \tag{2.14}$$

where l is the thickness and λ is thermal conductivity and *oz* and *iz* stand for the outer zone and an inner zone, respectively. Figure 2-26 illustrates the effect of grain size on the thermal conductivity, where the thermal conductivity is dramatically reduced when grain size falls below 100 nm.

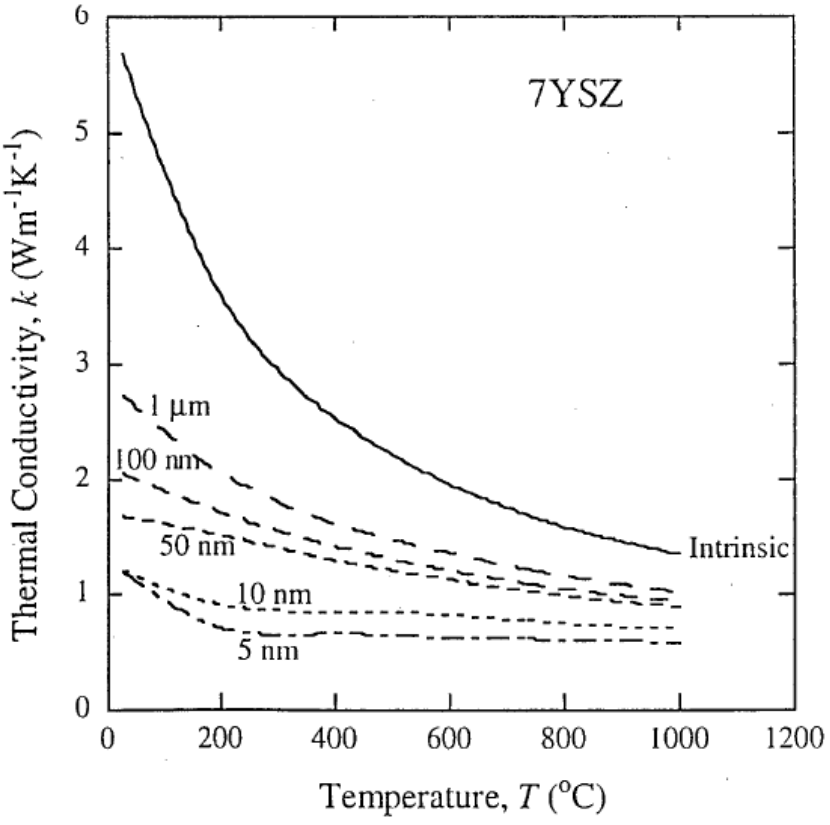

Figure 2-26 The effect of grain size on thermal conductivity of 7YSZ[88].

2.6.4 Effect of layering on the coatings produced by EB-PVD technique.

There are many techniques that were implemented by researchers to lower thermal conductivity. One such approach was the introduction of additional phonon scattering centres into the coating in order to reduce the thermal conductivity of EB-PVD TBCs [88]. Heat transfer is affected by the dispersion of phonon and photons [119]. The scattering of heat carriers is also possible at the interface between the layers. With this perspective, layering of the top coat will be an efficient idea to counter heat transfer [120]. Combined layers act as one homogeneous unit to reduce the thermal conductivity of coatings. To fully understand this effect, consider a thermal barrier coating that is composed of multiple nanolayers of different materials, such as zirconia and alumina [44], with the added advantage of thermal resistance at boundaries/interfaces. The higher the number of interfaces, the higher the possibility of scattering of heat carriers. Layering increases the scattering areas in the ceramic coating, leading to a lower thermal conductivity. Figure 2-27 provides an overview regarding the layering technique. Layered coatings will have a higher number of inner zones with a lower thermal conductivity as compared to a single layer.

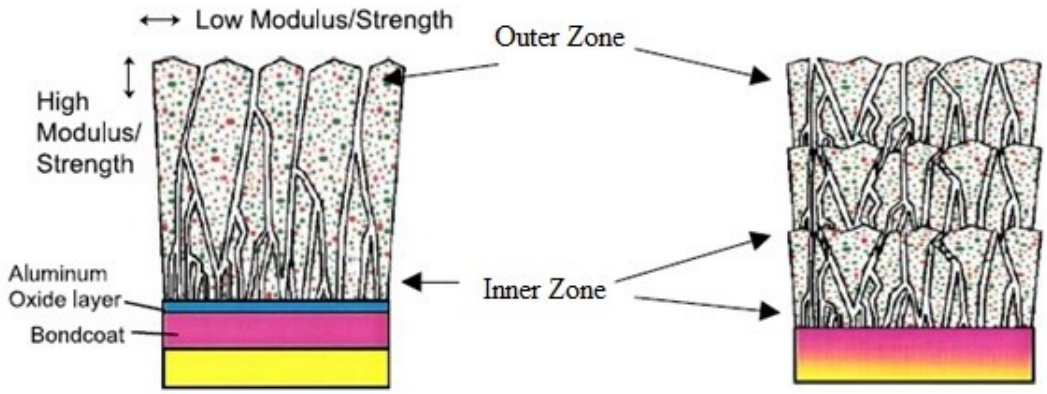

Figure 2-27 Schematic illustrating layering of coating [121]

The difference in the thermal conductivities of these is attributed to microstructures developed within the coatings. It is notable that the cracks are responsible for the lowering thermal conductivity along with the pores and other defects within the coating. It should be kept in mind while designing the layered top coat that if the layers are too distinct, the coating density will increase and can lead to premature delamination [121].

2.6.5 Effect of sintering on thermal conductivity

A large number of microcracks, pores and finer grains are present in the coatings, especially in the as-sprayed coatings. These microcracks and pores help to keep the thermal conductivity of the ceramics in the lower range. The concentration of these microcracks tends to fall when the coatings are exposed to higher temperatures because of the sintering effect. The internal structure of the coating changes quite clearly after heat treatment [122]. This happens due to the expansion of the coating during heating. The microcracks present in the coatings tend to diminish and overall porosity level falls. Sintering leads to an increase in thermal conductivity of the coatings. The thermal conductivity of as-sprayed coatings is in the range of 0.88-1.1W/(m·K).

The effect of temperature on both the conventional and nanostructured coating can be seen in Figure 2-28. The common trend of an increase in the thermal conductivity of coatings after heat treatment can be seen. The thermal conductivity of the as-sprayed coating is less than the 100h heat-treated coating. The thermal conductivity value increases from 0.8 W/mK for the as-sprayed coating to 1.2 W/mK for 100h heat treated coatings in the Nano-structured coating. This is attributed to sintering.

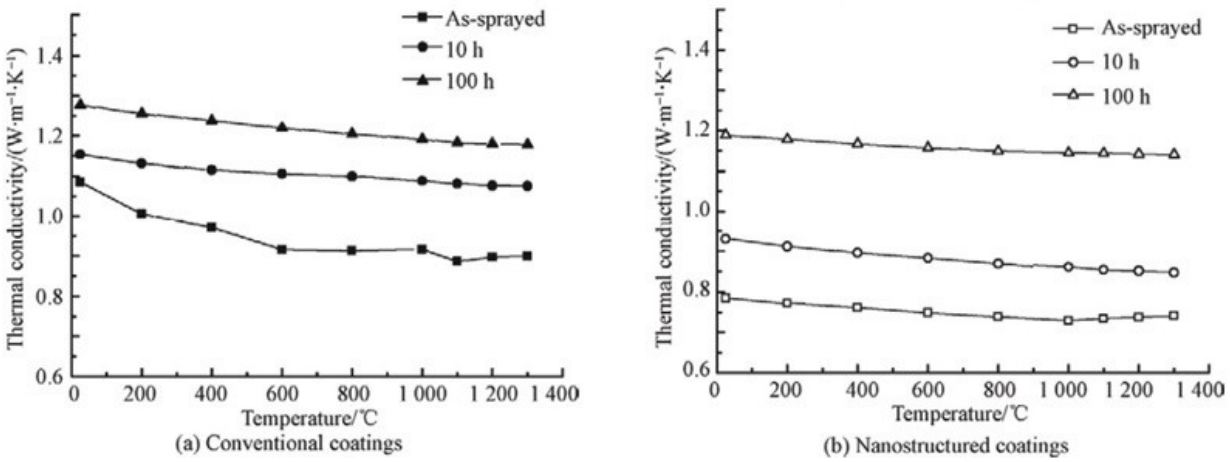

Figure 2-28 The effect of temperature on the thermal conductivity of conventional and nanostructured coatings [123]

Changes in the structure of coatings due to the sintering effect are irreversible. These changes decrease the thermal conductivity value during the heating-up period [123]. Stress relaxation plays an important role in this. The thermal conductivity of the nanostructured coating strongly depended on coating porosity. High porosity level in the nanostructured coating provides a lower thermal conductivity value. The pores interrupt the heat flow because of inefficient conduction through a void, even they are gas-filled [124]. Changes in the coating from the as-sprayed to the heat-treated state can be seen in Figure 2-29.

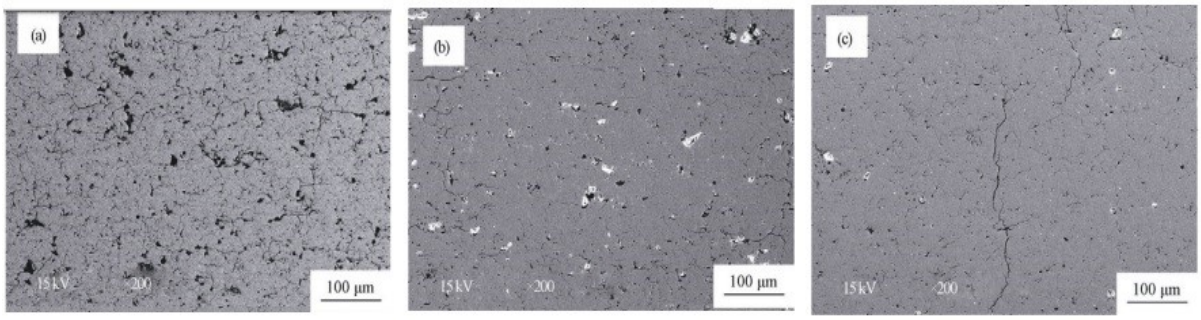

Figure 2-29 Changes in the coating microstructure due to heat treatment can be seen in (b) and (c) in comparison to (a) i.e. as-sprayed coating [123].

The changes include the closure of interlamellar pores and cracks, pore agglomeration and growth, healing of intra-splat microcracks and transformation of cracks into globular pores. The grain size of the nanostructured coating increases and exceeds the order of the mean free

path for phonon scattering with annealing time [125]. For this reason, the thermal conductivity value increases significantly with increasing grain size. From heat transfer theory, the thermal barrier effects in this situation can be determined by [123]

$$\Delta T = \frac{933\ln(1+200d)}{\ln(1+200d)+\frac{\lambda_c}{(0.005+d)h_h}+0.0267\lambda_c+\frac{2\lambda_c}{5h_i}} \tag{2.15}$$

where d is the ceramic coating thickness, h_h is the heat transfer coefficient of hot gas, h_i is the heat transfer coefficient of cooling air, and λc is the thermal conductivity of the ceramic coating.

2.6.6 Effect of interface on the thermal conductivity

The interface is an important structure in thermal barrier coatings. When heat flows across an interface between two different materials (phases) or two adjacent layers, there exists a temperature jump at the interface. This sudden change in temperature (in very small thickness of the coating) is attributed to the interfacial thermal resistance (ITR) that can be defined by the following [73]

$$R = \Delta T.J \tag{2.16}$$

where J is the heat flux density, the heat flow across a unit area in unit time, ΔT is the temperature difference between the two sides of the corresponding interface and R is the value of the ITR. The ITR was discovered in 1941 [126] and the temperature jump was at an interface between a solid and a liquid. Because of a temperature discontinuity at interfaces, composite materials will show a reduction in effective thermal conductivity due to the presence of the ITR. Temperature drops with respect to the dislocation can be seen in the coatings with an ITR in Figure 2-30. The temperature drop at the interface of top-coat and bond-coat is due to the

resistance offered by the boundary changes and these changes can simply be because of difference in material properties of top coat and bond coat.

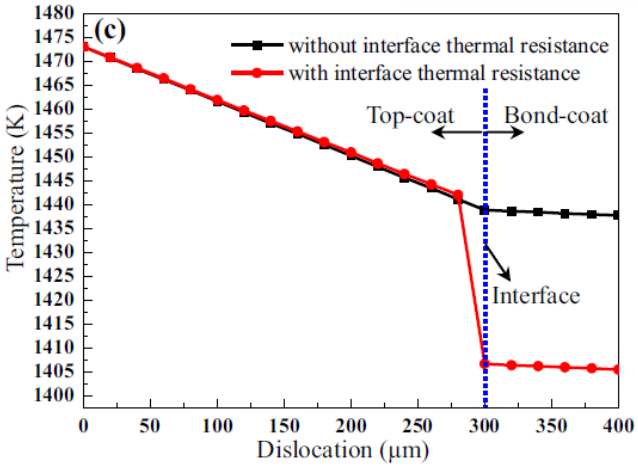

Figure 2-30 Difference in temperature drop with and without considering ITR [73]

The bond-coat/top-coat interface roughness also has a very important effect on the effective thermal conductivity of the as-sprayed TBCs [127]. The effective thermal conductivity will increase with increasing interface amplitude, while also considering the interfacial thermal resistance. However, this tendency is not evident without considering the interfacial thermal resistance.

3. Models for thermal conductivity

Modelling and predicting the thermal conductivity of thermal barrier coatings is an ongoing topic of research. Modelling involves the use of pre-existing data to form either an analytical or numerical model. These models can provide an estimate of the coatings that can be developed with modified properties. There are models that already exist.

First, a brief introduction about the thermal conductivity. Thermal conductivity (k), is the measure of heat transfer from one surface to another that is having a cross-sectional area A and are separated by a distance L. There are many formulas to calculate thermal conductivity depending on the coatings and its parameters. The thermal conductivity of free-standing materials can be determined by [128]

$$k = \alpha.C_p.\rho \tag{3.1}$$

where ρ is the density of the free-standing material (kg/m^3), C_p indicates the heat capacity of materials at constant pressure (J/(kg K)), and α is the thermal diffusion rate (m^2/s). The modelling of thermal conductivity is beneficial prior to the fabrication of the coating to better predict and understand the properties of new or modified coatings [129], [130]. Most of the times these models provide an estimation of the results that are comparable to the experimental results [130], [131]. Modelling reduce cost and increase efficiency by predicting the best possible combination of parameters for fabrication out of thousands of possible combinations.

Previous research work has produced models to predict thermal conductivity. A brief introduction to the existing models is discussed in this section.

3.1 Analytical models

A large number of analytical models have been developed to estimate the total thermal conductivity of the ceramic coatings deposited by various deposition techniques [46], [57], [74], [85]. The porous microstructure is considered one of the best ways to lower the thermal conductivity of TBCs [116], [132], [133]. Understanding the effect of pore size, shape, orientation and pore morphology can be enhanced using modelling. Most models are presented based on randomly distributed non-interacting pores of ellipsoids or spheroidal shapes, or some with periodic structures.

One of the early models was developed by Maxwell–Eucken in the late nineteenth century [99]. The assumption was made that dispersed phase was composed of randomly distributed, non-interacting and identical spheres. This model can be described by [99],[134]

$$\frac{k_{tot}}{k_d} = \frac{1-P}{1+0.5P} \tag{3.2}$$

where k_{tot} is the thermal conductivity of a porous material, k_d is the thermal conductivity of a dense material and P is the fraction of porosity. The assumption in this model was that the thermal conductivity of pores is small or negligible.

Another model was developed by Klemens. This model holds for non-spherical pores that are randomly distributed. It can be described by [135]

$$\frac{k_{tot}}{k_d} = 1-\frac{4}{3}P \tag{3.3}$$

where k_{tot} and k_d have the same meaning as mentioned above.

Hasselman [136] developed a model which calculated the effect of cracks having different orientations on the thermal conductivity of solid materials. It was concluded that maximum thermal insulation is obtained with cracks perpendicular to the direction of heat flow,

while cracks parallel to the direction of heat flow have the smallest effect on thermal conductivity.

Bruggeman provided an excellent model to predict the thermal conductivity of porous coatings [34]. Bruggeman extended the Maxwell model to systems having random dispersions of spherical particles of several sizes. He proposed a model that assumes that if a relatively large spherical particle is introduced into a dispersion containing much smaller particles, there will be a negligible disturbance of the field around the large sphere due to the small spheres. With this model, he showed that the limitation on a volumetric fraction of dilute dispersion can be removed. The Maxwell model is extended to [137]

$$\frac{k-k_m}{k+2k_m} = f\frac{k_d-k_m}{k_d+2k_m} \tag{3.4}$$

Change in conductivity dM, with the change in volume fraction of dispersed phase, is expressed as

$$\frac{dM}{3M} = \frac{dP}{1+P}\left(\frac{k_d-M}{k_d+2M}\right) \tag{3.5}$$

Integrating P from 0 to $\frac{f}{1+f}$ and M from k_m to k. leads to Bruggeman's two-phase model given by

$$\left(\frac{\frac{k}{k_m}-\frac{k_d}{k_m}}{\left(\frac{k}{k_m}\right)^{\frac{1}{3}}\left(1-\frac{k}{k_d}\right)}\right) = (1-f) \tag{3.6}$$

where k is the thermal conductivity of the composite, k_m is the thermal conductivity of the matrix, k_d is the thermal conductivity of the dispersed phase, and f is the volumetric fraction of

the i^{th} phase. Also, in this case, it is possible to generalise the modelling to a solute dispersion of randomly oriented ellipsoids.

McPherson proposed the analytical model for predicting the thermal conductivity of plasma-sprayed coatings [138] which involved regions of good and poor contact between lamellae where the regions of poor contact act as thermal resistances. The model can be given as [138]

$$\frac{k_{tot}}{k_d} = \frac{2f\delta}{\pi a} \tag{3.7}$$

where δ is the lamellae thickness, f is the fraction of 'true contact and a is the radius of individual contact areas. Li *et al.* [139] and Boire-Lavigne *et al.* [140] further developed this model.

Sevostianov *et al.* [141] developed a model which provides an improved relationship between the microstructure parameters and thermal conductivities. The microstructure was assumed to be composed of two families of penny-shaped cracks—horizontal and vertical. The thermal conductivity in the direction perpendicular to the substrate is given by [141]

$$\frac{k_{tot}}{k_d} = 1 - \frac{8\alpha_v}{3(1-P)} \tag{3.8}$$

where P is the density and α_v is the component of crack density tensor in the direction perpendicular to the substrate that incorporates the crack densities of both pore families and their scatters.

Lu *et al.* [142] proposed a model which included different kinds of pore morphologies, randomly oriented pores, aligned but spatially random pores, periodic pores and zigzag pores. They used the Finite Element Method (FEM) to calculate the conductivity of zigzag pores. The

model was applied to TBCs made by EB-PVD. The effective thermal conductivity k for zig-zag pores is obtained as [142]

$$k = \frac{\bar{q}}{(T_{bottom} - T_{top}) / \lambda} \tag{3.9}$$

where $q=q_z$ is the heat flux in the z-direction averaged in x over the top (or bottom) surface and T_{bottom} and T_{top} are the temperatures of the bottom and top surfaces respectively.

Wei *et al* proposed a model for the effect of defects on the thermal conductivity and calculated the effective thermal conductivity. They proposed a variable C_k that is an independent variable only affected by the nonlinear area around the defect. They concluded that this variable is independent of the thermal gradient and the plate size under consideration. There is no significant change in the value of C_k with respect to increasing temperature. The effective thermal conductivity of n pores having no interactions with each other can be obtained as [110]

$$K_{eff} = K_0 \left(1 - \rho - \frac{\alpha . \sum_{i=1}^{n} a_i^2}{hl} \right) \tag{3.10}$$

where K_0 is intrinsic thermal conductivity of the non-defective bulk material, a is the pore radius, α is taken to be equal to the numerical value of 3.06, h is the height and l is the width of the model.

3.2 Numerical models

Kulkarni *et al.*[143] studied the effect of powder morphology on the properties of plasma-sprayed YSZ coatings. A two-dimensional finite element model was used to represent the coating microstructure. There were three categories of voids that were considered — interlamellar pores (having a hexagonal shape), intra-splat cracks and globular pores. They predicted thermal conductivity values that were higher than the experimentally measured values due to lack of reference information for splat and pore size distribution.

Hollis [144] developed a model based on FEM to compute the thermal conductivity of special tungsten coatings. The model used 2-D images recorded using Scanning Electron Microscopy (SEM). The images were based on grey scale level in the micrographs. The dark segment represented the pores while the light portion represented tungsten. A finite element mesh was created over the image. APS coatings have a complex microstructure. A method to compensate for 3D pore structure effects was also proposed by choosing the maximum effective pore length for APS coatings [144].

Dorvaux *et al.* [145] developed software for the calculation of the thermal conductivity of porous coatings. This computation is performed based on binary images of real material. This approach included complex ceramic morphologies. The contribution of each pore family (globular pores, cracks etc.) towards thermal shielding abilities was determined by using image analysis. Later, this approach was used as an alternative to diffusivity measurements [146]. Further, it provides the relationship between sintering effects and thermal conductivity and was used to study the effect of pressure on thermal conductivity of TBCs.

Bartsch *et al.* [147] compared the results from the finite difference (Tbctool) and finite element simulations for determining the thermal response from binary images of EB-PVD TBC microstructures. The results were more precise with decreasing mesh size and when the area of the image is large.

Wang *et al.* [73] used the finite element method to simulate the heat transfer behaviour of TBCs with different interfacial characteristic based on several different interfacial thermal resistance (ITR) models. The simulation results indicate that the heat flux around the interface exhibits a significant changing characteristic and that the thermal insulation effect of TBCs would be enhanced with an increase in the area of the interface. The interface roughness (amplitude) also has a large effect on the effective thermal conductivity of the as-sprayed TBCs.

Tan *et al.* [103] generated a 2D finite element mesh with the help of processed SEM images of coating microstructure and predicted the thermal conductivity using commercial finite element code for some ceramic coatings. For YSZ coatings, the predicted results for the thermal conductivity were higher than the values obtained from the Laser Flash Analysis (LFA).

Qunbo *et al.* [148] developed a finite element mesh over a real microstructure image using digital image processing to predict various thermo-mechanical properties of TBCs. They concluded that transverse cracks in the coating are the most significant for thermal insulation.

Out of these models, Bruggeman's two-phase model is chosen as a reference model on which to propose a modification. The proposed model will be based on similar assumptions as described by Bruggeman.

The proposed model will be based on the porosity content present in the coating. There are several types of defects in the coating's microstructure. Of all, four types of defects will be chosen that will be distributed in a continuous matrix in randomly oriented manner.

A detailed discussion of the proposed model will be presented in Chapter 4.

4. Proposed model for thermal conductivity

As previously mentioned, the high-temperature performance of thermal barrier coatings is greatly influenced by microstructural features [97], [148]. The thermal and mechanical properties of ceramic coatings are also influenced by the deposition technique and process parameters, in addition to the intrinsic thermal properties of the coatings [149]. These factors contribute to changes in shape, size and morphology of the porosity inside the ceramic coating.

Analytical models provide details about the complex structure of thermal barrier coatings [150]. The defects in dense coatings strongly influence their thermal conductivity [110]. In general, these defects are often referred to as pores. Pores can be classified as open pores, horizontal or vertical pores or randomly oriented pores [151]. The most common type of pore in a coating is the randomly distributed pore.

Figure 4-1 provides an overview of the various types of defects that are assumed to be present in the coatings. The modelling of thermal conductivity is mostly performed on the basis of these types of pores. The spheroidal shape is best suited for the modelling as it can cover a wide variety of actual cracks or pores shape and orientation.

The models used for the distribution of the pores can be classified into symmetrical and asymmetrical models. This classification is based on the schematization of pores, either by the dispersion of the unique grains into the continuous matrix or by the symmetrical distribution of pores in the whole matrix.

The performance of the TBC is related to porosity; hence it became essential to design the thermal properties of these materials prior to actual fabrication by using a modelling approach.

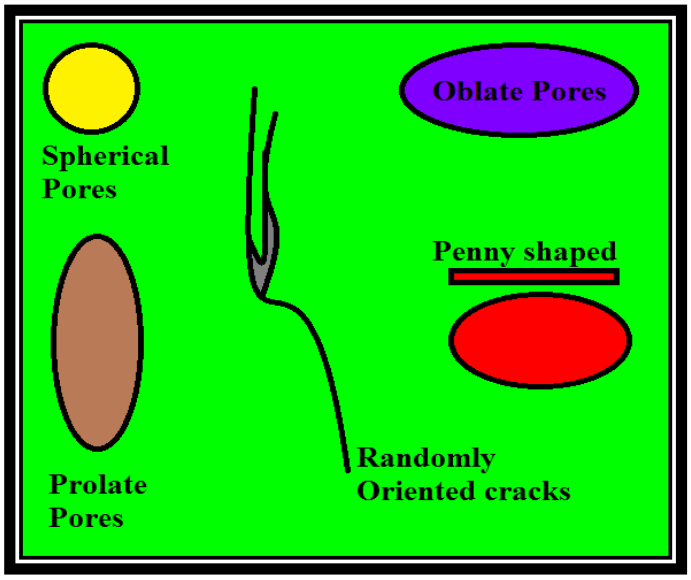

Figure 4-1 Different types of pores and cracks that are mostly used for modelling work.

The distribution of porosity in the analytical model can be presented precisely, however certain conditions need to be considered, such as the model must contain adequate microstructural details to represent the properties of the sample [152]. Even the minute details regarding the microstructural features of the coating must be included so that the actual properties can be modelled precisely.

Many analytical models have been developed and some of them have been discussed in the literature review. The models that predict the thermal conductivity with better accuracy are the hybrid combination of asymmetrical and symmetrical models [145]. Of these models, the Bruggeman asymmetrical model provides a better estimation of a coating's thermal conductivity [34].

As discussed in Chapter 3, the proposed model is based on Bruggeman's two-phase model. Details about the Bruggeman's model will be discussed in this section. Some assumptions in this thesis work are as follows:

- The thermal conductivity of the dispersed phase or of the defects is assumed to be negligible.
- Heat transfer is along the thickness of the coating only (or perpendicular to bond coat-substrate interface). No lateral heat transfer is assumed.
- The effect of connected pores is neglected.
- There is a linear relation between the porosity and thermal conductivity.

Bruggeman's model assumes the introduction several spheres in a dilute dispersion having an infinite range of size values and that each sphere is embedded in the continuous matrix. With his work, he removed the limitation on the volumetric fraction of the dilute dispersion that was not possible in the case of other models ($0 \leq f < 1$). Bruggeman designed the model for a porous TBC system. This model assumes only one type of defect having a single orientation. Example of such coatings can be seen in Figure 4-2.

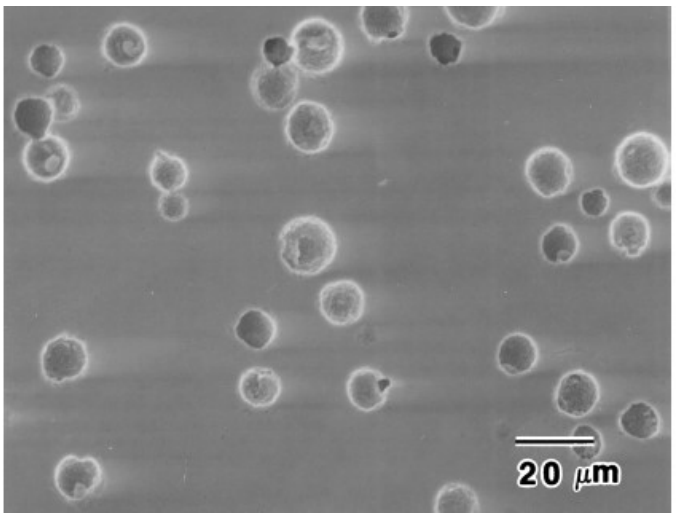

Figure 4-2 SEM image of spherical pores in continuous matrix [98]

The equation for the simple case of the Bruggeman model is given by the equation (3.6) , where k is the thermal conductivity of the composite, k_m is the thermal conductivity of the matrix, k_d is the thermal conductivity of the dispersed phase, and f is the volumetric fraction of the i^{th} phase.

Bruggeman's model is further simplified by assuming the thermal conductivity of pores/defects is negligible i.e. $k_d = 0$. Under the condition of non-radiating pores, equation (3.6) reduces to

$$\frac{k}{k_m} = \left(1 - f\right)^{\frac{3}{2}} \tag{4.1}$$

This equation is the special case when the pores are of spherical shape. The Bruggeman model is based on ellipsoids of revolution, hence in general, for the dispersion of an ellipsoid, the Bruggeman model is a modified version of equation (4.1) and is given by [153]

$$\frac{k}{k_m} = \left(1 - f\right)^{X} \tag{4.2}$$

where the value of X depends on certain factors such as the shape factor of the ellipsoid $\left(F\right)$ and α, which is the angle between the heat flux and the axis of revolution. The value of X can be described by [153]

$$X = \frac{1 - \cos^2 \alpha}{1 - F} + \frac{\cos^2 \alpha}{2F} \tag{4.3}$$

The value X is set to 3/2 when there are only spherical pores in a continuous matrix. The assumption of non-conducting pores/defects is valid for a certain temperature limit, however, its primary purpose is to simplify the model [34]. In reality, coatings contain several types of defects [19], [55], [110], [111]. Therefore, for more realistic modelling of coatings, superposition of the contributions of different defects types on the overall thermal conductivity

is required. One approach is to iterate the Bruggeman's two-phase model to higher levels of porosities. This approach is explained in detail in subsequent paragraphs.

The Bruggeman two-phase model consists of a binary mixture of dense material and spherical pores. To generate a three-phase model for composites, a two-phase model can be used in an iterative way. This approach works in two steps, first of all, the addition of type 1 porosity is assumed in the continuous matrix so that the average thermal conductivity of a binary mixture is obtained. Then, for the second step, the binary mixture is considered as a continuous matrix, and subsequently, a type 2 porosity is added in the same manner.

Suppose that f_1 and f_2 are the final percentages of type 1 and type 2 porosity, respectively, then the total porosity in the coating is given by f, which is given as the sum of the different types of porosities. Therefore, $f = f_1 + f_2$. There can be two ways of adding the defects in a continuous matrix. Consider if we add a Type 1 porosity first into the continuous matrix and then add a Type 2 porosity. This will lead to an equation given by

$$\left\{\Phi\left[\frac{f_2}{1-f_1}\right]\Psi\left(f_1\right)\right\} \tag{4.4}$$

Now consider if we first add Type 2 porosity in the continuous matrix and then Type 1, this will generate the formula as-

$$\left\{\Psi\left[\frac{f_1}{1-f_2}\right]\Phi\left(f_2\right)\right\} \tag{4.5}$$

The proposed model is developed by averaging the multiple values of the constituents that directly make up the composite material. Therefore, when we average the two possible cases we can have the thermal conductivity of the three-phase mixture [153] as

$$k = \frac{k_0}{2}\left\{\Psi\left[\frac{f_1}{(1-f_2)}\right]\Phi(f_2)+\Phi\left[\frac{f_2}{(1-f_1)}\right]\Psi(f_1)\right\} \tag{4.6}$$

where k_0 is the thermal conductivity of the matrix, $\Psi(f)$ and $\Phi(f)$ are functions describing the effect of defects on the thermal conductivity of the coating. This process is also known as an averaging technique. The equation (4.6) is symmetrical with respect to the product of $\Psi(f)$ and $\Phi(f)$ in order to satisfy the commutative properties of the dilution process. This property helps to produce a unique solution.

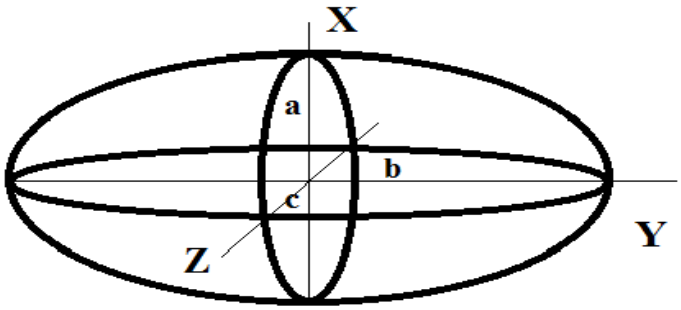

Figure 4-3 Spheroidal shape used in modelling defects

For this thesis work, spheroids (ellipsoids having a revolution axis corresponding to the ellipsoid axis '*a*' and with the other two axes equal i.e. *b*=*c*) are chosen to model the various types of defects. Spheroids can be used to define a wide variety of real situations by defining the angle between the heat flux and the dispersed particle i.e. *α,* and by varying the axes ratio *a/c*. A spheroidal shape can be seen in Figure 4-3. This shape can be modelled into lamellas, cylinders, spheres and spheroids by varying the ratio between the axes of the spheroid.

- Possible Shapes (Figure 4-4)→
  - Sphere: when all axes are equal i.e. a = b = c.
  - Oblate: when b > a and c > a.
  - Prolate: when a > b and a > c.

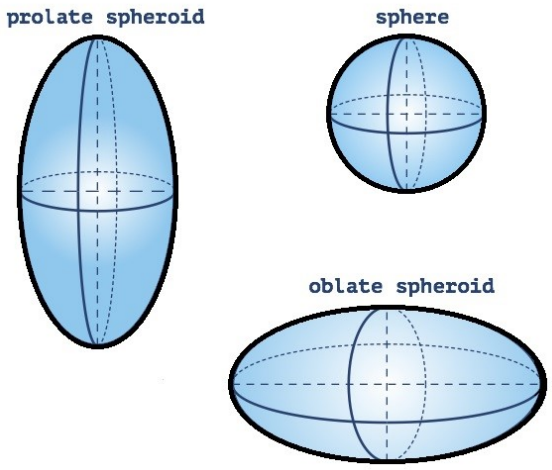

Figure 4-4 Pictorial representation of different spheroidal shapes

For equation (4.3), the values of the shape factor F vary as per the different shapes under consideration. The shape factor F depends on the ratio of axes a/c. The ratio of axes is obtained using the software Image J. The graphical representation of the shape factor with varying axial ratio *a/c* is shown in Figure 4-5.

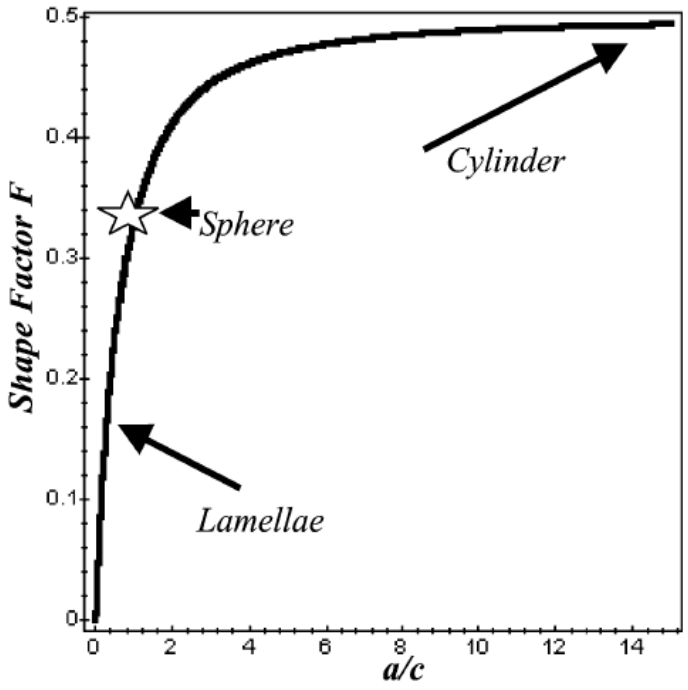

Figure 4-5 Shape factor F as a function of the axial ratio a/c of the spheroid [153].

Corresponding to the value of a/c, the shape factor F can be obtained from Figure 4-5.

In case of sphere shaped defects; when the major and minor axis are equal ($a = c$). For a sphere, the value of shape factor is given by F=1/3.

When the axis a is smaller than axes b and c ($c > a$), the spheroid is stretched horizontally to obtain the shape of an oblate spheroid. The shape factor F for oblate pores (lamellas) lies between 0 and 1/3.

A prolate shape spheroid is created when pores are stretched in the vertical direction and there is a very little area in the horizontal direction. The shape factor for prolate pores lies between 1/3 to 1/2.

There is an exception where, if the lamellae are oriented normal to the heat flux, X is equal to 1. An illustration of a prolate spheroid, oblate spheroid and sphere are shown in Figure 4-4. The value of the X can also be modelled using a cylindrical shape as well. For a cylinder, the X values depend on the orientation of the major axis a. The values are different depending on whether the 'a' axis is parallel, randomly oriented and/or perpendicular [153].

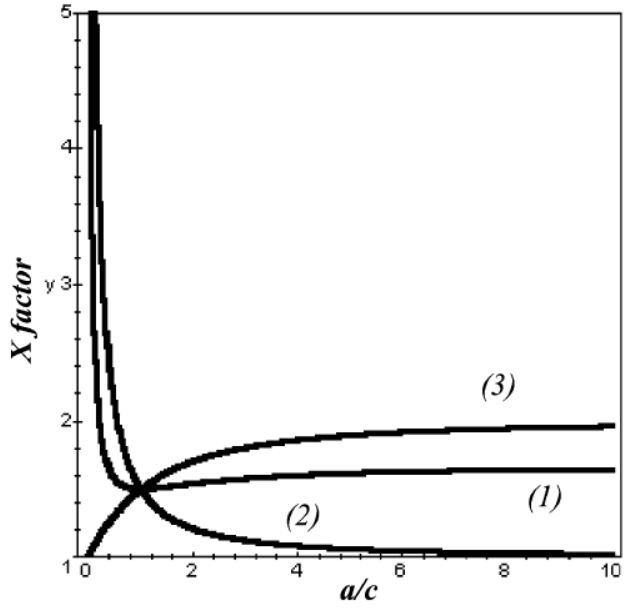

Figure 4-6 X-factor as a function of the axial ratio a/c for different spheroidal shapes [153].

Figure 4-6 represents the graph of the relationship between the *X* factor and *a/c* ratio. The curve marked as (1) represents the *X* factor values for spheroid pores that are randomly oriented. Curve (2) represents the *X* factor values for a spheroid with revolution axis '*a*' oriented parallel to the heat flux. Similarly, the curve (3) represents the values of *X*-factor for the spheroids oriented with the revolution axis '*a*' normally to the heat flux. The intersection of all three curves represents the point for the *X*-factor value for a sphere. At this point (*a/c=1*) and *X=1.5*. Flow chart of the whole process can be seen in Figure 4-7.

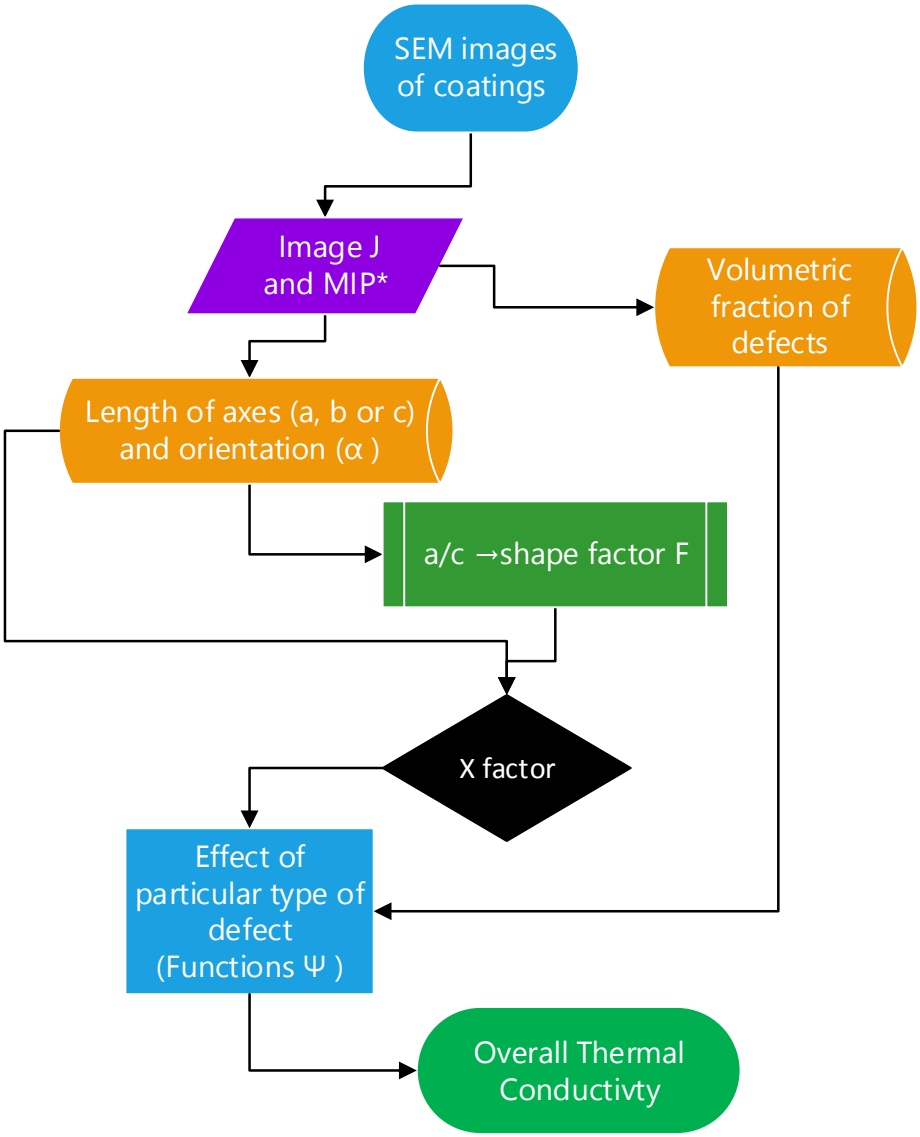

Figure 4-7 Flowchart describing the process to obtain the thermal conductivity of a coating.

For the present thesis work, Bruggeman's two-phase model was chosen as a reference model and with the help of an iterative approach (using the averaging technique), a five-phase model is developed. The goal this thesis work is to enhance the analytical model to better predict the overall thermal conductivity of a ceramic coating by using a five-phase mixture. In the proposed modified model, four different types of defects are assumed to be embedded into the continuous matrix. This makes this model as a five-phase model for porous composites. The assumption of no heat transfer through these pores is still valid, therefore $k_d = 0$ (k_d is the thermal conductivity of pores). The nomenclature of the current model is described in Table 4-1.

Table 4-1 Nomenclature of the proposed model

f_i	Represents the volumetric fraction of the i^{th} phase of the composite. Value of f range from 0-1.
Spheroid	Ellipsoid having a revolution axis corresponding to ellipsoid axis a and the other two axes are equal i.e. $b=c$.
Shape factor F	A numerical value related to the shape of a spheroid.
X factor	A numerical value taking into consideration both shape and orientation of spheroid in heat flux
k	The thermal conductivity of the composite.
k_0	The thermal conductivity of the dense material.
Φ, Ψ, Θ and β	Functions each representing the effect of different types of porosity on thermal conductivity
f_1, f_2, f_3 and f_4	Volumetric fraction of porosity corresponding to Ψ, Φ, Θ and β respectively.

The total porosity f is the sum of the contributions of all the different types of porosities. Therefore, it is given as $f = f_1+f_2+f_3+f_4$. The values of Φ, Ψ, Θ and β all are given by the equation (4.2). The values of different porosity types are obtained from previous works [88], [111], [119], [153], as well as from image analysis using Image J. With the proposed iterative approach, the addition of four different types of porosities simultaneously into the continuous matrix is carried out using the averaging method. This gives the formula for five-phase porous composite material that consists of twenty-four equations. Therefore, for better understanding, the formula for the five-phase model is divided into four parts. This process does not affect the formula in any manner as all four parts simply sum. The five-phase model can be expressed as

$$k = \frac{k_0}{24}(A+B+C+D) \tag{4.7}$$

where A, B, C and D provides simplification of the formula. The formula averages the all possible condition in which the four different types of defects can be added in different sequences. The values for A, B, C and D are given as follows:

$$A = \left\{\left\{\left(\frac{\Psi(f1)}{1-(f2+f3+f4)}\right)*\left(\frac{\Phi(f2)}{1-(f3+f4)}\right)*\left(\frac{\Theta(f3)}{1-f4}\right)*(\beta(f4))\right\}+\right.$$
$$\left\{\left(\frac{\Psi(f1)}{1-(f2+f3+f4)}\right)*\left(\frac{\Phi(f2)}{1-(f3+f4)}\right)*\left(\frac{\beta(f4)}{1-f3}\right)*(\Theta(f3))\right\}+$$
$$\left\{\left(\frac{\Psi(f1)}{1-(f2+f3+f4)}\right)*\left(\frac{\Theta(f3)}{1-(f2+f4)}\right)*\left(\frac{\Phi(f2)}{1-f4}\right)*(\beta(f4))\right\}+$$
$$\left\{\left(\frac{\Psi(f1)}{1-(f2+f3+f4)}\right)*\left(\frac{\Theta(f3)}{1-(f2+f4)}\right)*\left(\frac{\beta(f4)}{1-f2}\right)*(\Phi(f2))\right\}+$$
$$\left\{\left(\frac{\Psi(f1)}{1-(f2+f3+f4)}\right)*\left(\frac{\beta(f4)}{1-(f2+f3)}\right)*\left(\frac{\Phi(f2)}{1-f3}\right)*(\Theta(f3))\right\}+$$
$$\left\{\left(\frac{\Psi(f1)}{1-(f2+f3+f4)}\right)*\left(\frac{\beta(f4)}{1-(f2+f3)}\right)*\left(\frac{\Theta(f3)}{1-f2}\right)*(\Phi(f2))\right\}$$

$$B=\left\{\left\{\left(\frac{\Phi(f2)}{1-(f1+f3+f4)}\right)*\left(\frac{\Psi(f1)}{1-(f3+f4)}\right)*\left(\frac{\Theta(f3)}{1-f4}\right)*(\beta(f4))\right\}+\right.$$
$$\left\{\left(\frac{\Phi(f2)}{1-(f1+f3+f4)}\right)*\left(\frac{\Psi(f1)}{1-(f3+f4)}\right)*\left(\frac{\beta(f4)}{1-f3}\right)*(\Theta(f3))\}+\right.$$
$$\left\{\left(\frac{\Phi(f2)}{1-(f1+f3+f4)}\right)*\left(\frac{\Theta(f3)}{1-(f1+f4)}\right)*\left(\frac{\Psi(f1)}{1-f4}\right)*(\beta(f4))\}+\right.$$
$$\left\{\left(\frac{\Phi(f2)}{1-(f1+f3+f4)}\right)*\left(\frac{\Theta(f3)}{1-(f1+f4)}\right)*\left(\frac{\beta(f4)}{1-f1}\right)*(\Psi(f1))\}+\right.$$
$$\left\{\left(\frac{\Phi(f2)}{1-(f1+f3+f4)}\right)*\left(\frac{\beta(f4)}{1-(f1+f3)}\right)*\left(\frac{\Psi(f1)}{1-f3}\right)*(\Theta(f3))\}+\right.$$
$$\left\{\left(\frac{\Phi(f2)}{1-(f1+f3+f4)}\right)*\left(\frac{\beta(f4)}{1-(f1+f3)}\right)*\left(\frac{\Theta(f3)}{1-f1}\right)*(\Psi(f1))\}\right.$$

$$C=\left\{\left\{\left(\frac{\Theta(f3)}{1-(f1+f2+f4)}\right)*\left(\frac{\Psi(f1)}{1-(f2+f4)}\right)*\left(\frac{\Phi(f2)}{1-f4}\right)*(\beta(f4))\right\}+\right.$$
$$\left\{\left(\frac{\Theta(f3)}{1-(f1+f2+f4)}\right)*\left(\frac{\Psi(f1)}{1-(f2+f4)}\right)*\left(\frac{\beta(f4)}{1-f3}\right)*(\Phi(f2))\}+\right.$$
$$\left\{\left(\frac{\Theta(f3)}{1-(f1+f2+f4)}\right)*\left(\frac{\Phi(f2)}{1-(f1+f4)}\right)*\left(\frac{\Psi(f1)}{1-f4}\right)*(\beta(f4))\}+\right.$$
$$\left\{\left(\frac{\Theta(f3)}{1-(f1+f2+f4)}\right)*\left(\frac{\Phi(f2)}{1-(f1+f4)}\right)*\left(\frac{\beta(f4)}{1-f1}\right)*(\Psi(f1))\}+\right.$$
$$\left\{\left(\frac{\Theta(f3)}{1-(f1+f2+f4)}\right)*\left(\frac{\beta(f4)}{1-(f1+f2)}\right)*\left(\frac{\Psi(f1)}{1-f2}\right)*(\Phi(f2))\}+\right.$$
$$\left\{\left(\frac{\Theta(f3)}{1-(f1+f2+f4)}\right)*\left(\frac{\beta(f4)}{1-(f1+f2)}\right)*\left(\frac{\Phi(f2)}{1-f1}\right)*(\Psi(f1))\}\right.$$

$$D=\left\{\left\{\left(\frac{\beta(f4)}{1-(f1+f3+f2)}\right)*\left(\frac{\Psi(f1)}{1-(f3+f2)}\right)*\left(\frac{\Theta(f3)}{1-f2}\right)*(\Phi(f2))\right\}+\right.$$
$$\left\{\left(\frac{\beta(f4)}{1-(f1+f3+f2)}\right)*\left(\frac{\Psi(f1)}{1-(f3+f2)}\right)*\left(\frac{\Phi(f2)}{1-f3}\right)*(\Theta(f3))\}+\right.$$
$$\left\{\left(\frac{\beta(f4)}{1-(f1+f3+f2)}\right)*\left(\frac{\Theta(f3)}{1-(f1+f2)}\right)*\left(\frac{\Psi(f1)}{1-f2}\right)*(\Phi(f2))\}+\right.$$
$$\left\{\left(\frac{\beta(f4)}{1-(f1+f3+f2)}\right)*\left(\frac{\Theta(f3)}{1-(f1+f2)}\right)*\left(\frac{\Phi(f2)}{1-f1}\right)*(\Psi(f1))\}+\right.$$
$$\left\{\left(\frac{\beta(f4)}{1-(f1+f3+f2)}\right)*\left(\frac{\Phi(f2)}{1-(f1+f3)}\right)*\left(\frac{\Psi(f1)}{1-f3}\right)*(\Theta(f3))\}+\right.$$
$$\left\{\left(\frac{\beta(f4)}{1-(f1+f3+f2)}\right)*\left(\frac{\Phi(f2)}{1-(f1+f3)}\right)*\left(\frac{\Theta(f3)}{1-f1}\right)*(\Psi(f1))\}\right.$$

By simply averaging all the possibilities of the addition of defects, the five-phase formula was obtained. Each type of defect has its respective shape factor *F* and *X*-factor. The calculation of these parameters is important for the proposed model to work as expected. These calculations are performed in the next section.

4.1 Calculation of the *X*-factor for different values of shape factor *F* and angle *α*

The model for the five-phase composite material depends on the shape, size and orientation of the various types of porosities/defects. It is known that the orientation of the pores and cracks impact the overall thermal conductivity [19], [136], [142]. Even a small deviation in the axes of the pores will result in different values for the thermal conductivity, even for materials with the same composition [154]. As discussed earlier in the above section, the *X* values vary according to the shape under consideration. In this section, the different values of *X* with respect to different angles and shapes will be calculated using equation (4.3).

The first step for the model is to obtain values of different axes of the defects using Image J. After obtaining the ratio of axes *a*/*c*, the shape factor *F* is obtained from the Figure 4-5. The *F* values vary with respect to different kinds of shapes. The orientation of the defects is also obtained using Image J. The orientation α (see Figure 4-8) is the angle between the vertical heat flux and the axis of revolution.

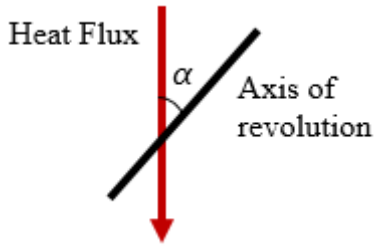

Figure 4-8 Representation of angle α

The value of shape factor *F* for the horizontal type of defects or lamellae lies within the range of 0-1/3. It is apparent from the work of Hasselman that the pores that are perpendicular to the direction of heat flow are more beneficial in reducing the thermal conductivity compared to the pores that are aligned parallel to the direction of heat flux [136]. This explains the lower thermal conductivity of APS coatings as compared to EB-PVD TBC. APS coatings have a more splat structure (lamellae porosity) that lowers the heat transfer [140].

Vertical type of defects or the cylindrical defects has a shape factor *F*, in the range of 1/3-1/2. The cylindrical shape is used to represent the cracks or pores that are more spread in coatings. The tiny voids are often represented by a sphere, but in most cases, these pores get elongated during the thermal cycling under the influence of thermal stress and mismatch between thermal expansion coefficient of different materials [155].

The values of *X*-factor are calculated using equation (4.3) at various angles, such as 0°, 30°, 45°, 60° and 90°. The difference caused by changing the orientation of an axis can be seen

in the figures below. Figure 4-9 and Figure 4-10 represent the graphs between the values of *X* corresponding to the values of *F* at an angle *α* of 0 degrees.

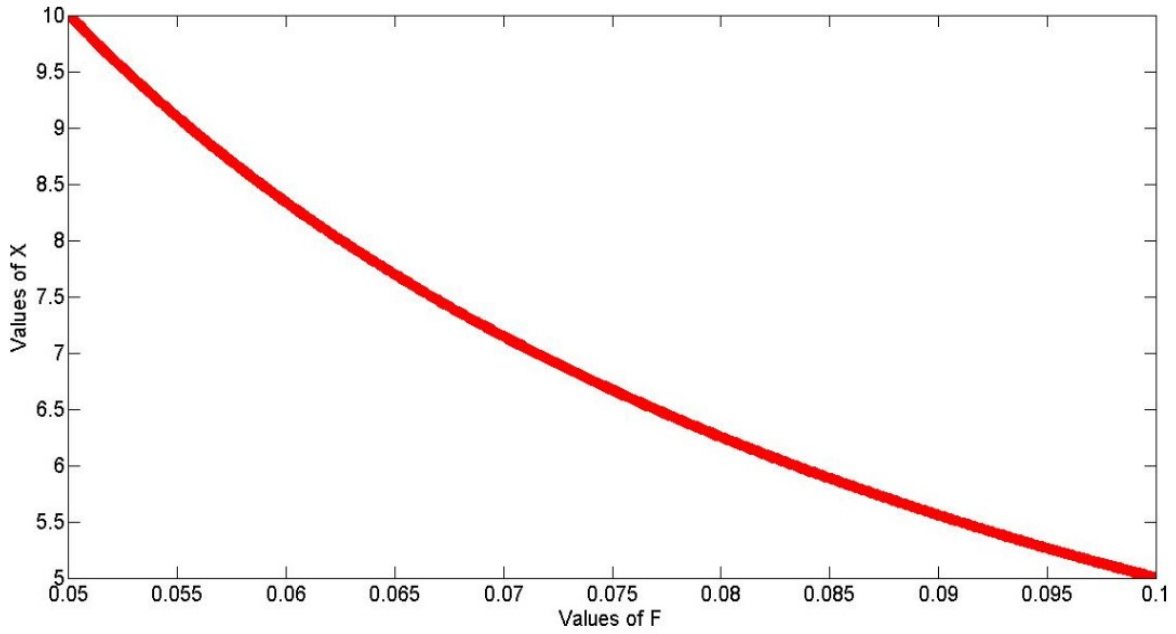

Figure 4-9 Values of X with respect to shape factor F at α = 0° for F between 0.05 to 0.

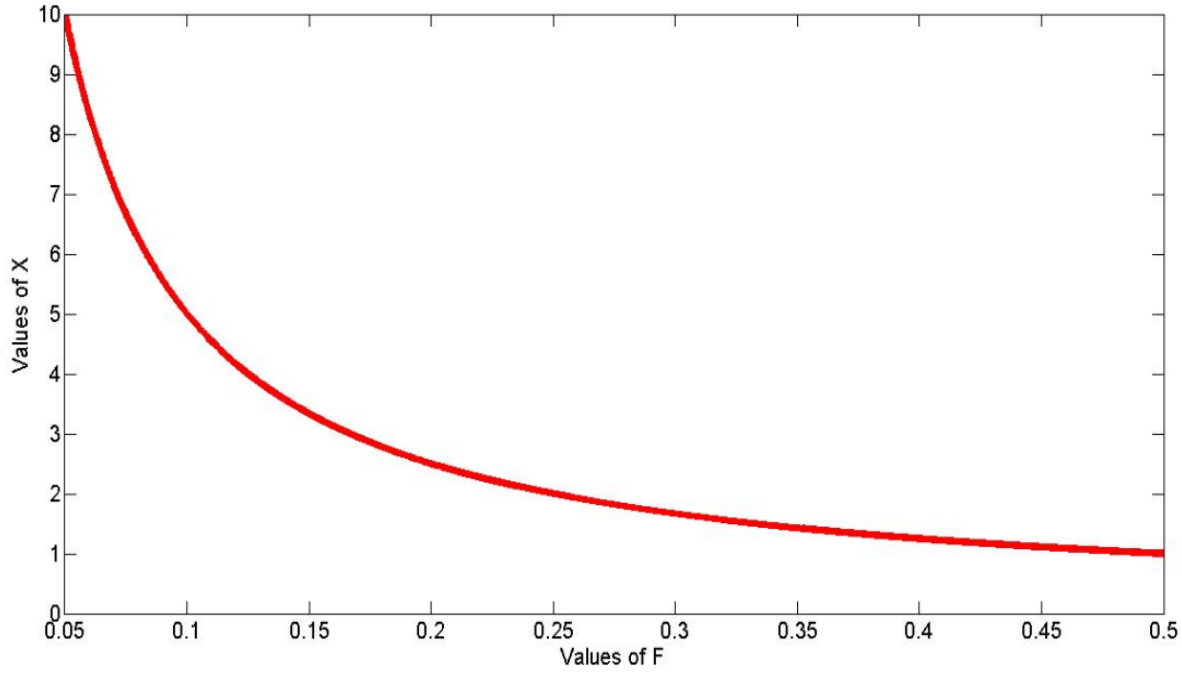

Figure 4-10 Values of X with respect to shape factor F at α = 0^0 for F between 0.05 to 0.5

Changing the angle of the axis of revolution corresponding to heat flux from 0° to 30° affects the values of *F* and ultimately the values of *X*. Figure 4-11 represents the changes in the values of *X* for the variation in angle α from 0° to 30°.

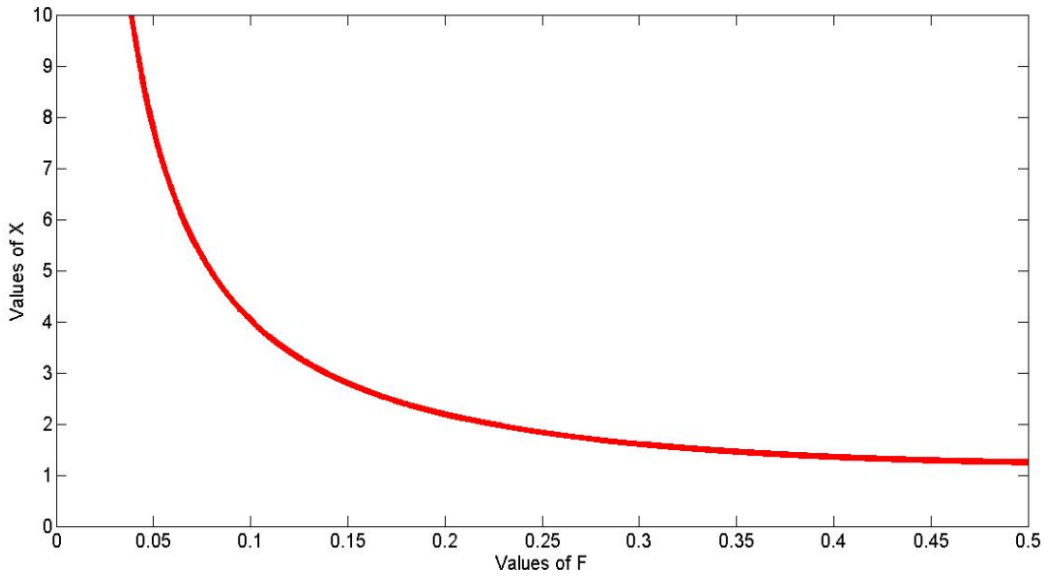

Figure 4-11 Values of X with respect to shape factor F at α = 30° for F between 0 to 0.5

The change in the curvature of the graph provides evidence to support the dependence of *X* values on the shape factor *F*. Figure 4-12 represents the graph between *X* and *F* for an angle α=45°.

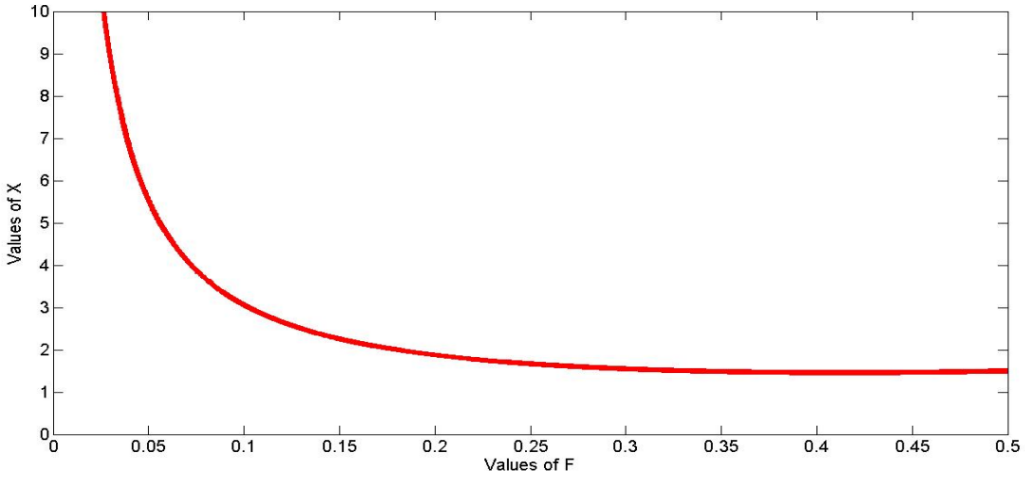

Figure 4-12 Values of X with respect to shape factor F at α = 45° for F between 0 to 0.5

Figure 4-13 illustrates the results obtained during the calculation of the *X* factor corresponding to *F* at an angle of 60° between the axis of revolution of the spheroid and heat flux.

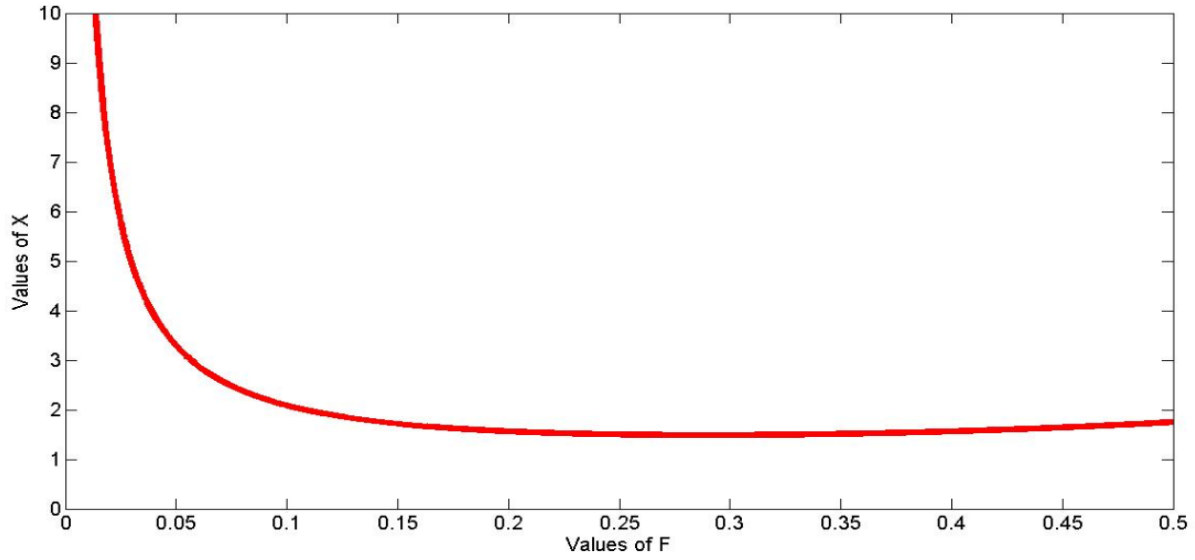

Figure 4-13 Values of X with respect to shape factor F at α = 60° for F between 0 to 0.5

It can be seen from all the figures present in this section that there is a variation in the values of *X* with increasing angle *α*. When the axis of revolution is directly perpendicular to the heat flux, the value of *X* increases with an increase in the value of shape factor *F*. The representation of this can be clearly seen in Figure 4-14, where the starting value of *X* is the lowest and tends to increase with increasing value of *F*. The results obtained from these graphs will be used in the proposed five-phase model for composite materials to calculate the thermal conductivity of different materials. Certain points or values will be chosen from these figures for particular cases.

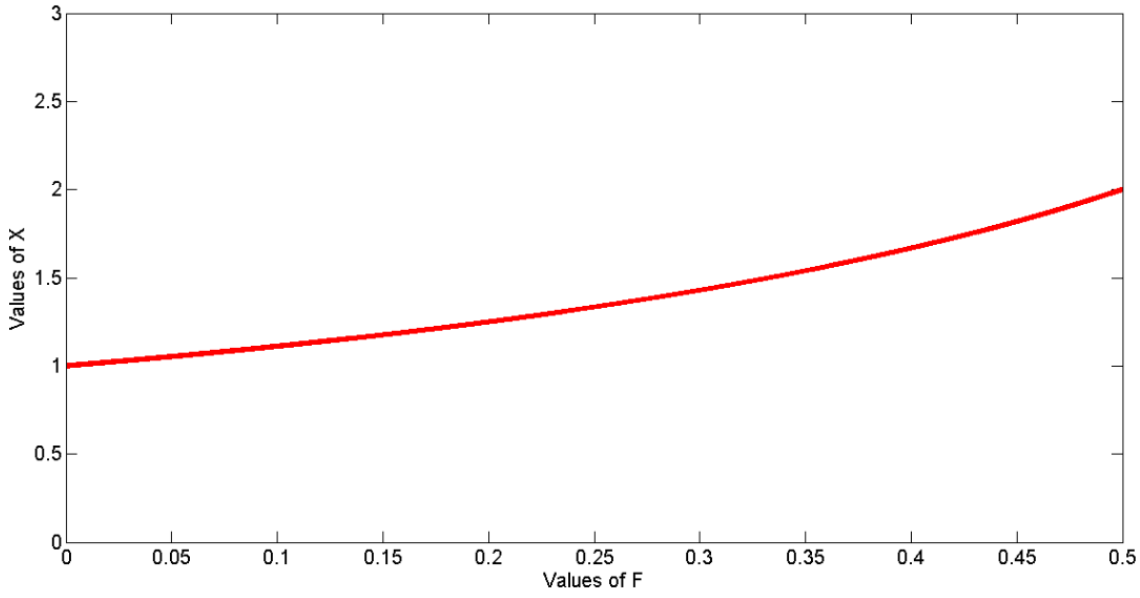

Figure 4-14 Values of X with respect to shape factor F at α = 90° for F between 0 to 0.5

4.2 Obtaining values for the current model

Currently, the evaluation of porosity volume is the major method of characterization of thermally sprayed deposit microstructure. To better estimate the thermal conductivity of the coating with the five-phase model, the shape factor *F* is chosen to approximately to 5 decimal places. During the calculation of the values, changes corresponding to a single decimal place are inevitable. Therefore, certain values of *F* have higher decimal places to accommodate minute changes.

For the computation of thermal conductivity using the equation (4.7), the values of the functions Φ, Ψ, Θ, and β all defined using equation (4.2). Table 4-2 represents the effect of different values of *X* on the different functions. The functions used in this table are based on the equation (4.2).

Table 4-2 The effect of different F and α

Function	**Representation in terms of *X***
Open randomly oriented - Φ(f)	$(1-f)^{X_1}$
Revolution axis oriented parallel to heat flux - Ψ(f)	$(1-f)^{X_2}$
Non-flat spheroids - Θ(f)	$(1-f)^{X_3}$
Revolution axis oriented perpendicular to heat flux - β(f)	$(1-f)^{X_4}$

When the length of axes $a = c = 1$, then ratio $a/c = 1$. Corresponding to the ratio of axes equal to one, we have shape factor F=0.3333. At any given angle, the value of X in this is always equal to 1.5.

Table 4-3 The X values for F=1/3 at different angles

The X values obtained for the shape factor F = 0.3333 or 1/3	
Angle *α*	***X* values**
At 0°	1.5
At 30°	1.5
At 45°	1.5
At 60°	1.5
At 90°	1.5

This shows that the current shape being modelled is a sphere as there is no change in the value of X with changing the orientation of the pore (see Table 4-3). In actual coatings,

there are very few voids that are identical to the shape of a sphere due to the elongation of cracks and pores during thermal cycling [155]. Most of the real cracks or pores can be modelled using spheroids. Spheroids encompass most cracks and pores that can be found in the high-temperature coatings [142].

During the calculation of *X*-factor, the values are obtained in the range of 1 to 10 for different types of pore shapes and orientation. A limit is set on cracks to be considered as microcracks, as it is difficult to model the small cracks. The maximum upper limit for narrow microcracks is arbitrarily chosen as 100nm. The microcracks with length over 100nm are treated as open porosity.

The microcracks can be described by sharp disk-shaped spheroids (penny shape pores). Penny shaped cracks can be observed in two different orientations. Most of the cracks have a revolution axis oriented parallel to the thickness of the coatings. This type of pores can be denoted by the function Ψ. The remnant penny-shaped pores have the revolution axis oriented perpendicular to the heat flux. This type of pore can be denoted by function β. The *X* value for these microcracks changes with different types of material under consideration.

The axes ratio in the case of microcracks is obtained as 0.07. Using this value, the value for shape factor *F* is obtained using Figure 4-5. Further using the value of *F*, we found the value of *X* for function the $\Psi(f)$ using $\alpha = 0^{o}$. The value of $\Psi(f) = 7$ is obtained for most of the materials. This value is a fitting parameter in the model.

Furthermore, for the penny-shaped cracks, the a/c ratio is approximately equal to 10 and the corresponding shape factor *F* is 0.496. The angle α is equal to 90^{o} for penny-shaped cracks. The value of the function $\beta(f)$ varies between 1.2 – 2, due to the variation of the ratio of axes, but for most cases, $X = 2$ is chosen for β.

Another type of porosity that is modelled is the non-flat spheroid. The non-flat spheroids are represented by the function $\Theta(f)$. The axes ratio for these types of pores is equal to 0.7. The angle α is $0°$ in this case. Using these values of F and α and using the equation (4.3), the X value for non-flat spheroidal shaped defects is obtained as 1.7.

The open randomly oriented porosity is described by the function $\Phi(f)$. In the case of randomly oriented defects/pores, the ratio of axes is 1:1.25 leading to shape factor F of 0.3. The defects are assumed to have the value of angle $\alpha = 0°$. The value of X for open randomly oriented porosity is obtained as 1.66, as found in the work of Schulz [156].

Table 4-4 Values of different parameters

a	c	a/c	F (shape factor)	X	Defect Shape
1	1.25	0.8	0.3	1.66*	Open Randomly Oriented
1	14	0.07	0.067-0.072	7^	Microcracks
10	1	10	0.496	2*^	Penny shaped ($\alpha=90^o$)
1	1.4	0.7	0.294	1.7*	Non-flat porosity

Different combination of ratios a/c and their respective shape factors F with final X-values can be obtained from the Table 4-4. Table 4-5 represents the values of different parameters that are used in the proposed model corresponding to different pore shapes and their respective functions that describe the effect of the defect on the thermal conductivity of coatings. The values for randomly oriented pores are calculated at various angles and their

respective shape factors are described with these angles. These values are calculated using the previously described equations for *F* and *X*.

Table 4-5 Representation of functions with respective shape factor F and X value.

Function	**Value of shape factor *F***		**Value of *X*-factor**
Φ(*f*)	at 0°	0.30001	1.66
	at 30°	0.28632	
	at 45°	0.25216	
	at 60°	0.1638	
	at 90°	0.3976	
Ψ(*f*)	0.071429		7
Θ(*f*)	0.2941		1.7
β(*f*)	0.41665 - 0.24999		1.2 - 2

The data in Table 4-5 are graphically represented in Figure 4-15. These data points are used in the five-phase model proposed in this thesis. The results for thermal conductivity values are obtained using these data points. These points are treated as valid for all the materials that are being modelled in this work.

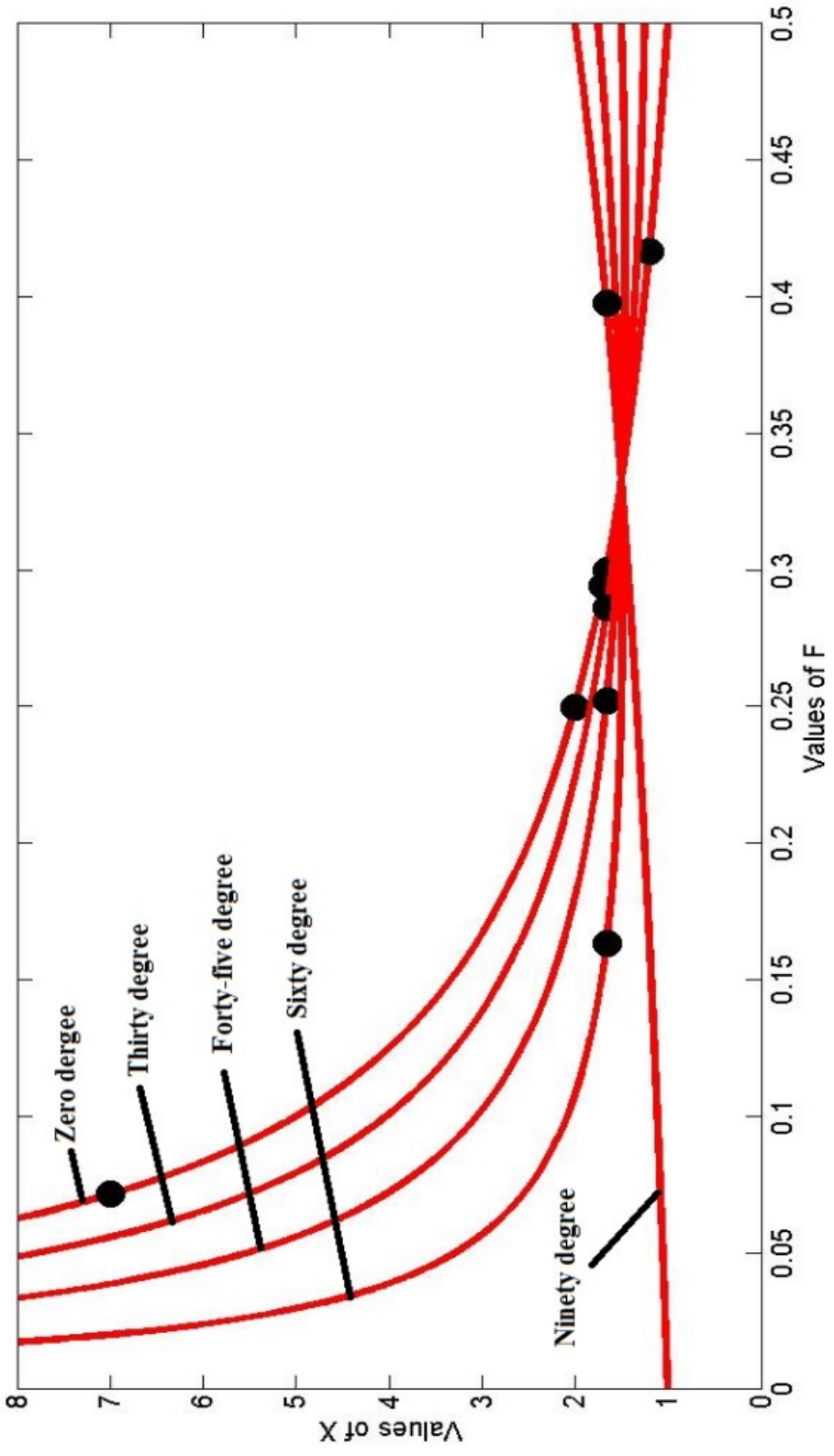

Figure 4-15 Representation of data points for various angles

5. Verification of the proposed model.

An important step in research is to validate the results. To authenticate the proposed model, results are obtained from prior models, FEA model and experimental results for comparison to the proposed five-phase model.

5.1 Microstructure Characterization of TBC

The properties of a thermal barrier coating rely significantly on its microstructure and defects of all the constituents, including pores, cracks, oxides, impurities and other contaminations. A better understanding of the coating microstructure allows detailed investigation of the mechanical properties, electrical/dielectric behaviour, and thermal transport properties.

Quantitative and/or qualitative analysis of microstructural aspects of the TBCs has been performed in the past using several techniques [139], [157]–[159]. Defect or porosity levels in the coatings can be calculated using some advanced techniques such as mercury intrusion porosimetry (MIP) [160], image analysis software i.e. Image J [161], and SANS i.e. small angle neutron scattering technique [162]. These methods help to evaluate the total porosity in a coating containing different types of pores, pores of different sizes and distribution, and can even obtain the orientation of small-scale defects [111], [143], [163]. Of these methods, image analysis is economical, robust and a more reliable method to characterize the TBC microstructure [164].

Image J uses the cross-sectional images of the coating to obtain information regarding the pores, cracks, other defects and their orientation. Commonly used methods to obtain better quality cross-sectional images are scanning electron microscopy (SEM) [165], and light optical microscopy (LOM) [166]. The data for the validation process in this thesis are obtained from the references that used SEM images for image analysis (using Image J) and MIP technique.

Some of the data are obtained using Image J software. The calculated data is combined with reference data to validate the results of the five-phase model. Details regarding the image analysis using Image J and MIP process are discussed in next section.

5.1.1 Fundamentals of image analysis technique

The goal of image analysis is the extraction of meaningful information about the microstructure of the coatings. Several software packages to analyse the porosity of materials have been developed and one of the most used is Image J. Over the past thirty years, this software drove the field of microstructural characterization. The structure of Image J has been kept simple and user-friendly with modifications to its tools and plug-ins. A core set of principles allowed the software to become a modern image processing platform.

A brief introduction to the process of image analysis using Image J (National Institute of Health (NIH), USA) is discussed in this section. To capture the variation in the microstructure using image analysis techniques, several images are needed along the cross-section of the microstructure. These digital images are composed of thousands of pixels. These pixels are tiny dots connected in a sequence to generate an output (image). These images are converted into binary format using Image J. The magnification of images affects the data. Therefore, the magnification of images is set to a certain value to obtain global information regarding coating microstructure. A too-high magnification leads to loss of global data and too low magnification leads to depletion of small-scale details of the microstructure. Error in the data is also caused by factors such as brightness, contrast, operating mode and location from where the image is taken.

Image J can analyse two types of images namely, grey-scale images and binary images. The software converts digital coloured images into a grayscale image. Image scale is set as per the magnification of the image. Image threshold is set with respect to the number of pores or

defects present in the picture. The raw data can be converted into numbers and details about each pore and crack can be obtained. The basic structure of Image J can be seen in Figure 5-1.

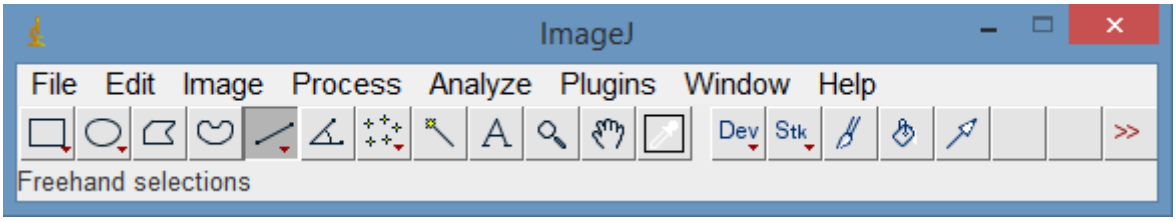

Figure 5-1 Representation of the Image J software menu.

The results for porosity can directly be retrieved from the percentage area column. This software can also provide other details such as total area, average pore size, circularity, solidity, feret diameter (a measure of an object size along a specified direction) and feret angle. This analysis of original coatings offers an exact experimental data for our reference. The data obtained from this process can be used to compare with the results of the model proposed in this thesis.

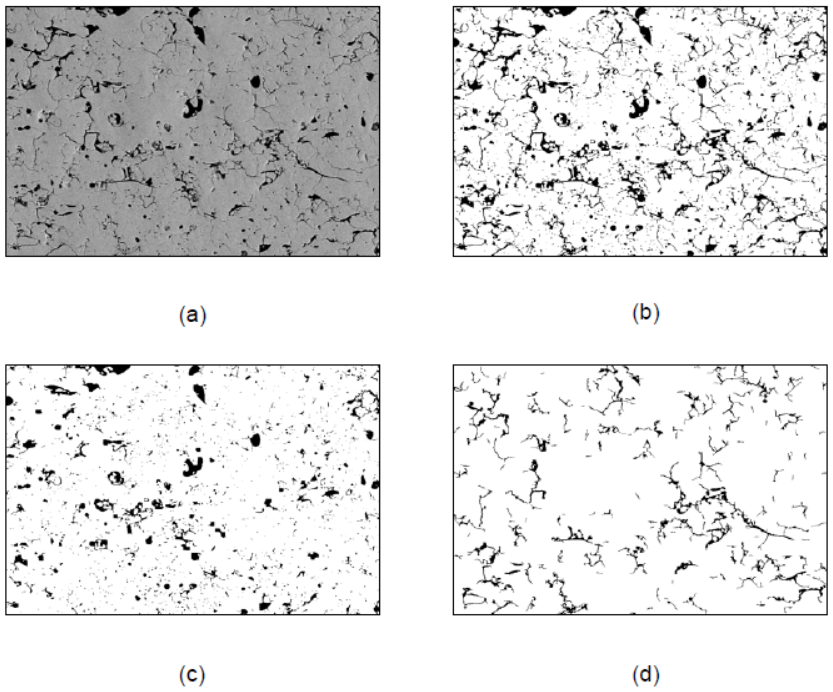

Figure 5-2 Image analysis for TBC: (a) Original SEM image, (b) Binary image, (c) Globular pore image, (d) crack image

Collection of coating images

Thermal spray coatings are dissected into pieces and each piece is polished on the cross-section or in-plane surface. The polished pieces are used as samples to obtain high-resolution microstructure images using SEM. Figure 5-2 represents the image analysis technique performed on an image of a thermal spray coating of YSZ. The transition from (a) to (b) in Figure 5-2 is the image thresholding.

5.1.2 Fundamentals of mercury intrusion porosimetry

Qualitative characterization of porosity of TBCs is possible via microstructural observation and quantitative characterization by Mercury Intrusion Porosimetry (MIP). MIP is an advanced technique to characterize the distribution of pore sizes. It allows the measurement of total porosimetry for open pores. It is an indirect method but is quite simple. The information about the connectivity of pores can be obtained using this method. MIP can measure capillary pores in the range of 0.005-10μm.

Mercury intrusion porosimetry is based on the principle that a non-wetting liquid that has a contact angle greater than 90°, will only encroach the capillaries under pressure. The relation between the pressure and capillary diameter is given as [167]

$$P = \frac{-4.\gamma.cos(\theta)}{d} \tag{5.1}$$

where P is the pressure, γ is the surface tension of the liquid, θ is the contact angle between the mercury and the pore wall and d is the diameter of the capillary.

The requirement of this process is that mercury must be forced into the capillaries under pressure. A schematic representing the mercury intrusion process is shown in Figure 5-3. The mercury-filled piston-cylinder apparatus is pushed against the coating surface. The piston is forced to move in the downward direction so that mercury can penetrate the small capillary

pores replacing the vacuum. The pore size distribution is established from the volume encroached at each pressure increment. The total volume of the porosity can be obtained by simply calculating the total volume of mercury intruded.

The limitations of this process are that in many cases this process is not able to measure the true distribution of sizes for pore geometry. For instance, for materials having very large internal pores that are accessible through very narrow throats, MIP interprets the size of the pores as the diameter of their throats. This error is referred to the “ink bottle” effect. This method also fails to provide accurate results for pores with radii larger than 80μm.

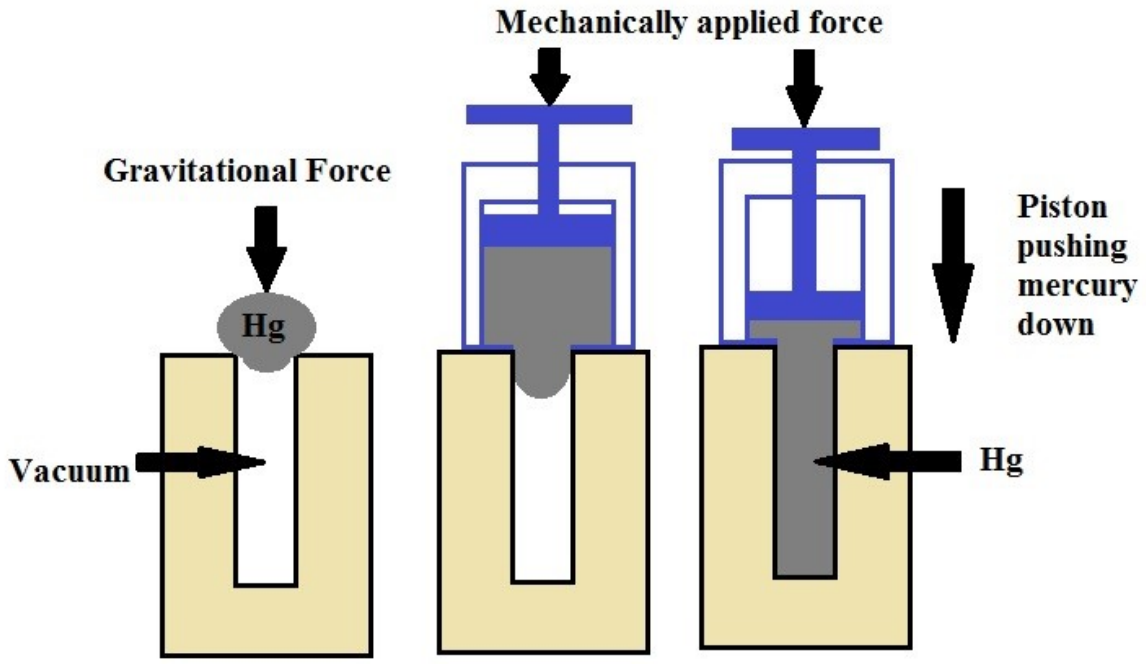

Figure 5-3 Schematic of Mercury Intrusion Process.

The results obtained from these two processes are used in this thesis. The data for the validation process are obtained from several sources including the results of image analysis. The combined results of Image J and MIP are used so that a better estimation of porosity content of small and large cracks that are present in coatings can be obtained.

5.2 Collected data from various sources and obtained results.

The results obtained from the proposed model are compared with four-phase model results, experimental results and FEA results. Data obtained for the four-phase model are presented in. Table 5-1 describes different types of porosity content present in a coating. The coatings used are Yttria Partially Stabilized Zirconia (YPSZ), Magnesia-stabilized Zirconia (MSZ), and Ceria Stabilized Zirconia (CSZ). The composition of these materials is (8YSZ) $8Y_2O_3$-ZrO_2, (22MSZ) 22MgO-ZrO2 and (25 CSZ) $25CeO_2$-$2.5Y_2O_3$-ZrO_2.

A single image of the cross-section is used to calculate the porosity content. It should be noted that the different images of the same coating (at different layer thickness) may produce different results for the porosity content.

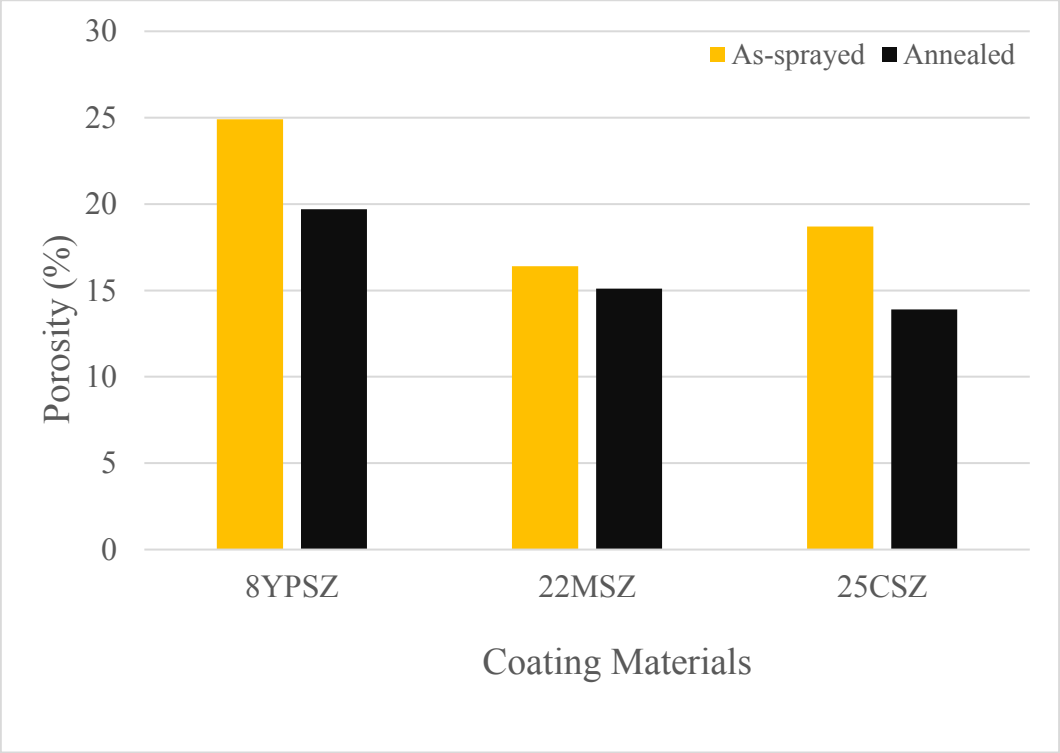

Figure 5-4 Porosity level of as-sprayed and annealed coatings of different coatings.

Table 5-1 Input parameters for four-phase model [153]

Sample Materials	8YPSZ	22MSZ	25CSZ
Bulk Thermal Conductivity (W/(m.K))	2.8	2.2	2.8
Overall Porosity (%) (As sprayed)	24.9	16.4	18.7
Overall Porosity (%) (Annealed)	19.7	15.1	13.9
Open Randomly oriented porosity (As sprayed)	0.9	4.5	3.9
Open Randomly Oriented porosity (%) (Annealed)	5.2	10.4	3.4
Microcracks (%) (As sprayed)	9.4	5	6.5
Microcracks (%) (Annealed)	2.8	3.3	7.5
Non-flat porosity (%) (As sprayed)	14.6	9.6	8.3
Non -flat porosity (%) (Annealed)	11.7	1.4	5.4

The porosity content of three different coating materials is presented in Figure 5-4. The yellow bars represent the porosity content of as-sprayed coatings and black bars represent the porosity content of heat-treated (annealed) coatings. A drop in the porosity content can be seen for the heat-treated coatings. This drop in porosity is due to sintering of the coatings due to thermal cycling [123].

Further data are collected for different forms of yttria-stabilized zirconia coatings. Three different forms of coatings are considered and their thermal conductivity modelling and measurements are performed. The results for porosity content are obtained for as-sprayed and annealed coatings using Image J. The abbreviations used in Table 5-2 are as follows: F&C refers to Fused and Crushed, A&S refers to Agglomerated and Sintered and HOSP refers to plasma densified hollow spheres.

Table 5-2 Calculated porosity for different YSZ samples using Image J.

YSZ Samples	Overall Porosity (%) (As-sprayed)	Overall Porosity (%) (Annealed)
F&C	21.3	16.9
A&S	17.9	16.1
HOSP	19.0	14.4

A graphical representation of three different YSZ coatings is given in Figure 5-5.

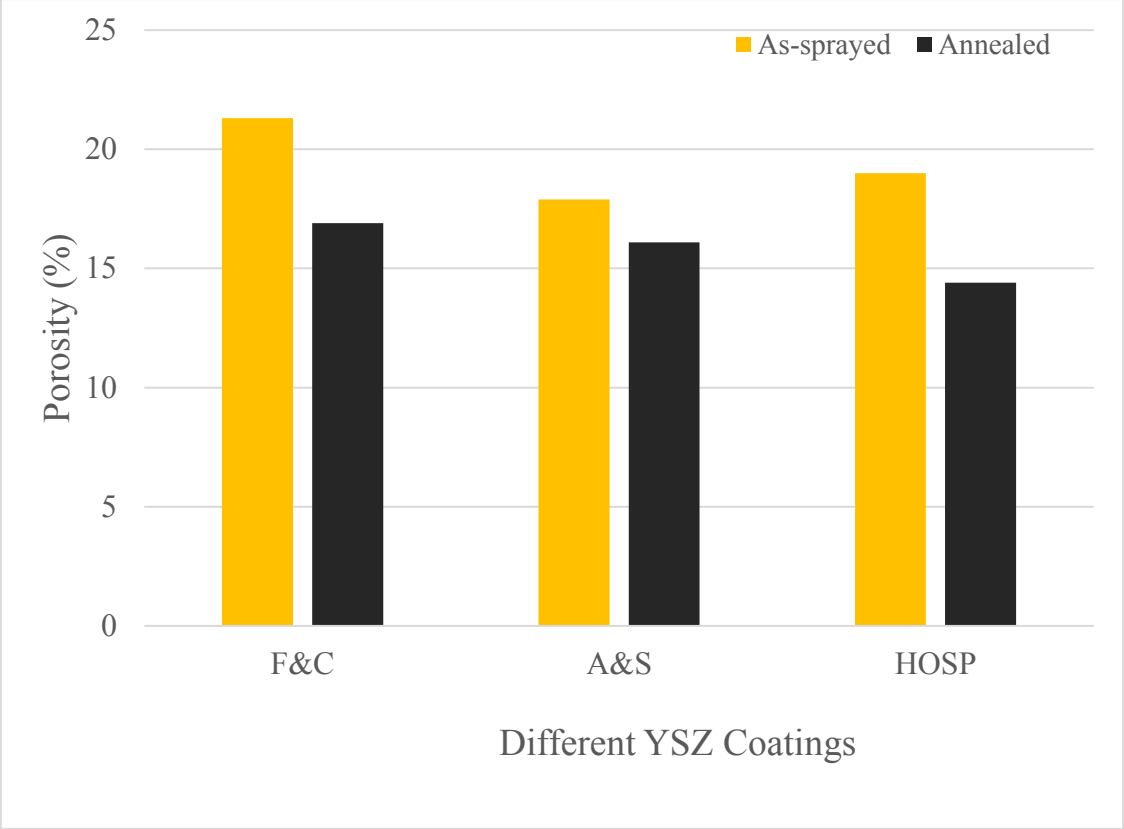

Figure 5-5 Porosity level in three different types of YSZ coatings.

In Figure 5-5, the yellow bars represent the porosity content of as-sprayed coatings and the black bars represent the porosity content of heat-treated annealed coatings.

The five-phase model for the composite material was used to calculate the thermal conductivity of various coatings. The data used in the proposed model can be obtained from Table 5-3. Thermal conductivity of Molybdenum, 8YSZ, 22MSZ, 25CSZ, YSZ- F&C, A&S, HOSP was calculated using the five-phase model. Porosity content of the coating materials is presented in Figure 5-6. The overall porosity level is distributed into four different categories; open randomly oriented pores, microcracks, non-flat porosity and penny-shaped cracks.

*H.T refers to heat treated samples in Table 5-3.

Table 5-3 Results obtained from the five-phase model for different materials.

Sample Material	Molybdenum	8YSZ	8YSZ H.T	22MSZ	22MSZ H.T	25CSZ	25CSZ H.T
Bulk Thermal conductivity	142	2.8	2.8	2.2	2.2	2.8	2.8
Obtained Thermal conductivity using Five-phase model	15.76	1.18	1.60	1.14	1.35	1.175	1.93
Total porosity	50.5	24.55	20.7	18.9	16.8	23.7	13.9
Open randomly oriented porosity (>100nm)	9	1.25	5.2	4.5	10.4	3.9	5.1
Microcracks (<100nm)	13	6.2	2.8	5	3	6.5	1.9
Non-flat porosity	13	14.3	11.7	6.9	1.4	8.3	3.8
Penny shaped	15.5	2.8	1	2.5	2	5	3.1

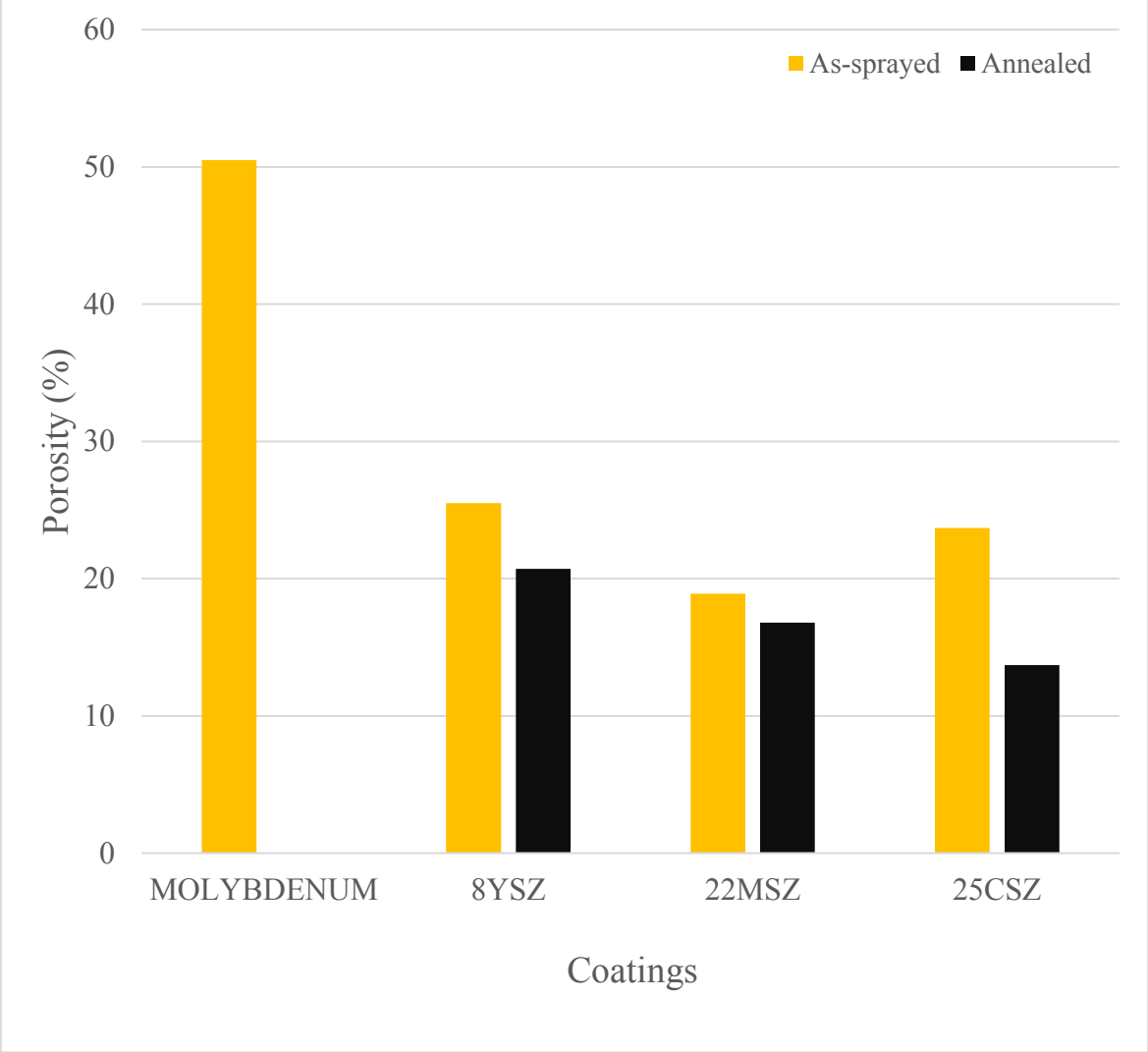

Figure 5-6 Porosity level for different materials for the five-phase model.

The black and yellow bars in Figure 5-6 represent the porosity content for as-sprayed and annealed coatings respectively.

The results obtained from the five-phase model for thermal conductivity of coatings are presented in Figure 5-7. Only results for as-sprayed coatings of the three materials are presented in this figure.

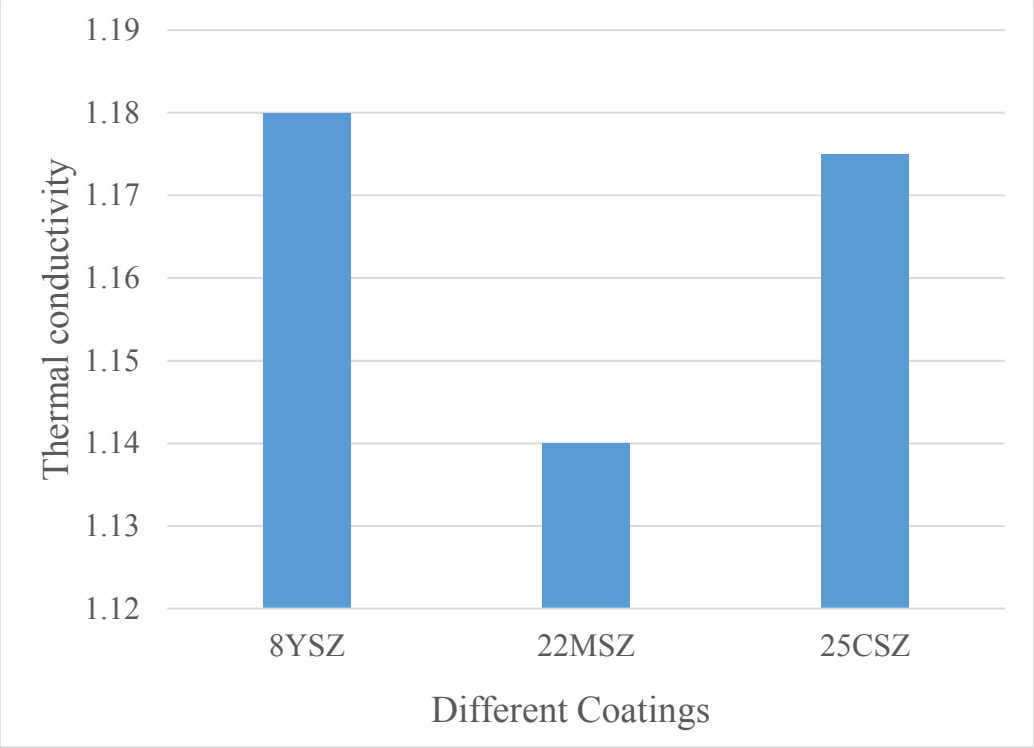

Figure 5-7 Thermal conductivity obtained using five-phase model.

The thermal conductivity of three different YSZ coatings was obtained using the five-phase model. The overall porosity and porosity distribution among various contributing factors are presented in Table 5-4 along with the obtained values of thermal conductivities using the five-phase model.

Table 5-4 Calculation of thermal conductivity for different YSZ samples using Five-phase model

Sample Material	HOSP (As sprayed)	HOSP (H.T)	F&C (As sprayed)	F&C (H.T)	A&S (As sprayed)	A&S (H.T)
Bulk Thermal conductivity	2.8	2.8	2.8	2.8	2.8	2.8
Obtained Thermal conductivity using Five-phase model	1.12	1.36	1.2	1.79	1.33	1.56
Total porosity	19	14.4	21.3	16.9	17.9	16.1
Open randomly oriented porosity (>100nm)	3.6	2.2	6	5.8	4.99	2
Microcracks (<100nm)	9.4	8	7.2	2	6.87	4.8
Non-flat porosity	3.5	3	3.1	4.7	4.05	7.8
Penny shaped	2.5	1.2	5	4.4	2	1.5

Figure 5-8 presents the results obtained from the calculation of thermal conductivity of three YSZ coatings, HOSP, F&C, and A&S. Blue bars represent the thermal conductivity of as-sprayed coatings and orange bars represent the thermal conductivity of annealed coatings. The increase in the thermal conductivity is attributed to sintering since small microcracks and vertical cracks or pores tends to diminish during the thermal cycling due to the expansion of coating material during heating.

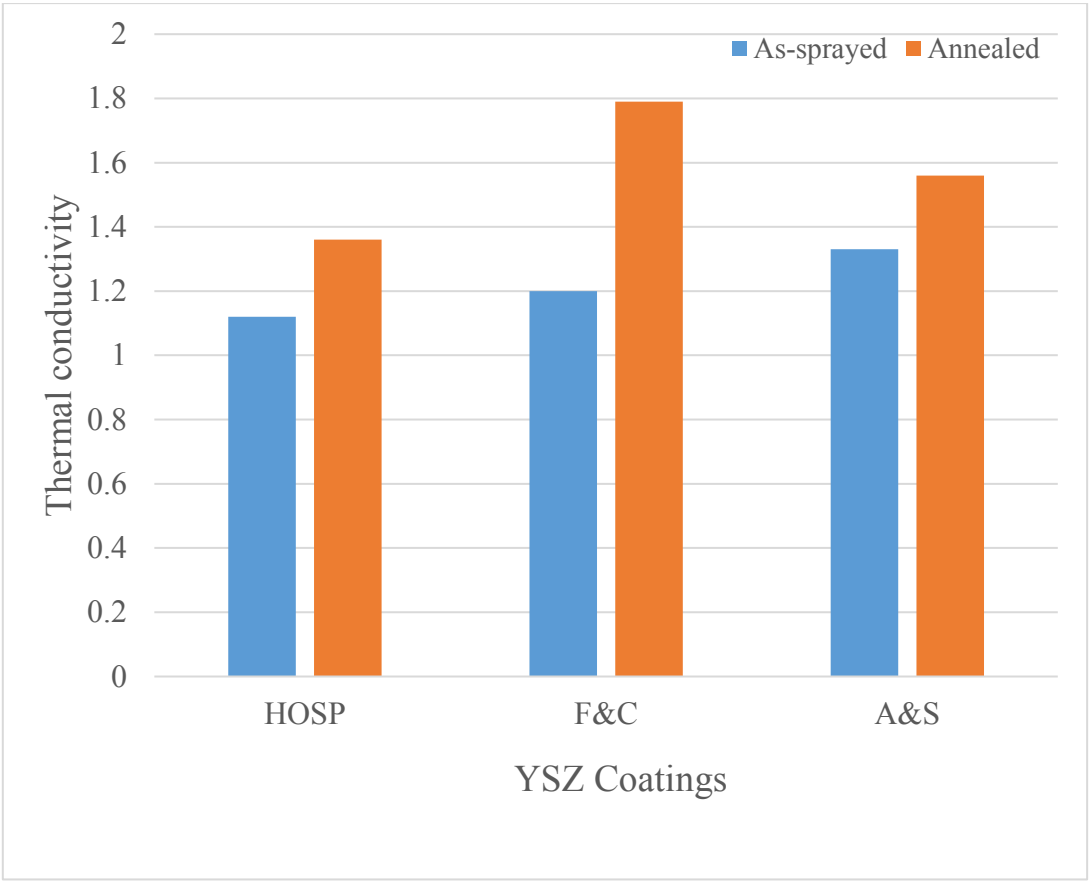

Figure 5-8 Thermal Conductivity of different YSZ coatings obtained from the five-phase model.

Comparison of results obtained from the five-phase model with experimental results is carried out in Table 5-5. Graphical representation of this comparison can be seen in Figure 5-9.

Table 5-5 Comparison of five-phase results with experimental results

Sample	Experimental thermal conductivity		Simulated thermal conductivity using five-phase model	
	Before H.T	After H.T	Before H.T	After H.T
8YSZ	1.2	1.62	1.18	1.60
22MSZ	1.1	4.37	1.14	1.35
25CSZ	1.19	2.05	1.175	1.93
Molybdenum	14.2-15.8	N/A	15.76	N/A

In Figure 5-9, blue bars represent the thermal conductivity obtained from the five-phase model for composite materials while the orange bars represent the values obtained from experimental results. The value obtained from the experimental data in the case of 22MSZ (annealed) coating is much higher than the 22MSZ (as-sprayed). The bulk thermal conductivity of 22MSZ is 2.2 W/(m.K). The value obtained for heat-treated 22MSZ is near 4 W/(m.K), which is higher than the bulk thermal conductivity. Given the outlier nature of this point, it was assumed that this value was a transcription error.

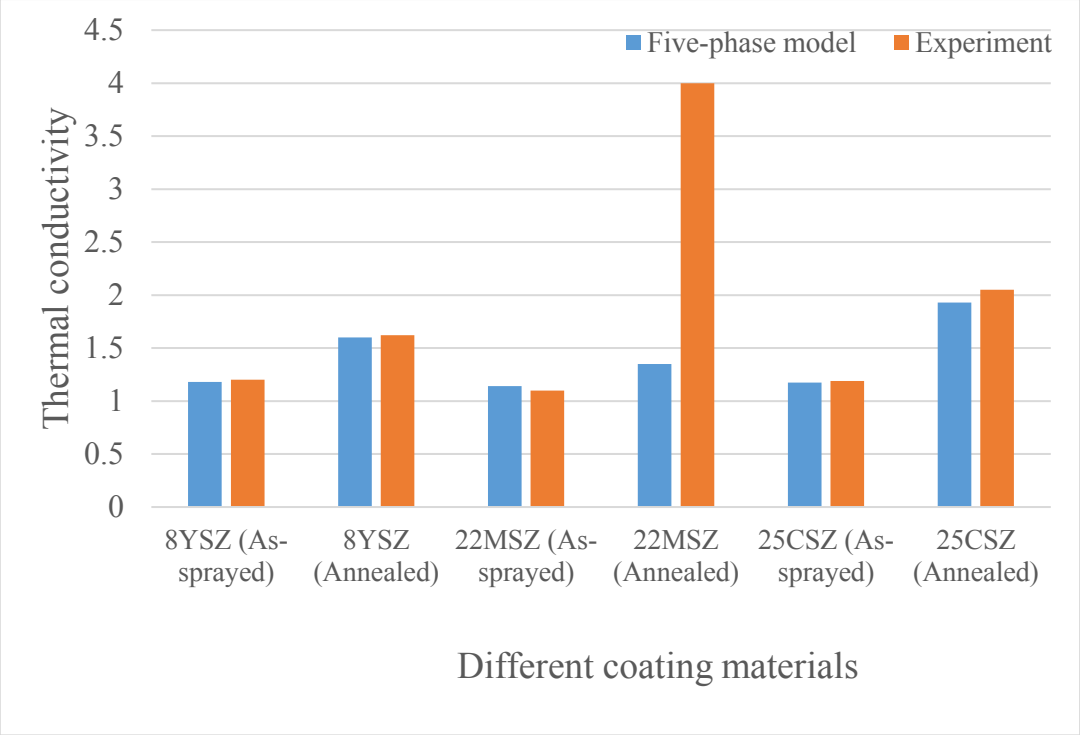

Figure 5-9 Comparison of thermal conductivity obtained from a five-phase model with experimental results.

Similar to the previous comparison, another comparison is performed between the results obtained from the four-phase model and five-phase model (Table 5-6). This comparison provides a better understanding of the results obtained since the five-phase model depicts the results better than the four phase-model.

Table 5-6 Comparison of five-phase model to four-phase model experiment

Sample	Thermal conductivity obtained from four-phase model		Thermal conductivity obtained from five-phase model	
	Before H.T	After H.T	Before H.T	After H.T
8YSZ	1.0	1.68	1.18	1.60
22MSZ	1.2	1.37	1.14	1.35
25CSZ	1.13	1.68	1.175	1.93

In Table 5-7, the percentage difference between the results obtained from the five-phase model and four-phase model is calculated. Negative sign represents a percentage decrease in the values obtained using the five-phase model with respect to the four-phase model.

Table 5-7 Difference between results from the five-phase model and four-phase model.

Sample	Difference between five-phase model and four-phase model
8YSZ (As-sprayed)	15.25%
8YSZ (Annealed)	-5%
22MSZ (As-sprayed)	-5.2%
22MSZ (Annealed)	-1.48%
25CSZ (As-sprayed)	3.8%
25CSZ (Annealed)	12.95%

In Table 5-8, the difference between the thermal conductivity values obtained from experimental results and results from the five-phase model is calculated and presented in the second column. These results are compared with the difference between experimental thermal conductivity values and results from the four-phase model, which are presented in the third column. It can clearly be seen from Table 5-8 that the results obtained from the five-phase model are closer to the experimental values than those obtained from the four-phase model.

Table 5-8 Thermal conductivity difference between experimental results and different models.

Sample	Thermal conductivity difference between experimental values and five-phase model	Thermal conductivity difference between experimental results model and four-phase model
8YSZ (As-sprayed)	-1.66%	-16.7%
8YSZ (Annealed)	-1.23%	3.7%
22MSZ (As-sprayed)	3.6%	9.1%
22MSZ (Annealed)	-69%	-68.6%
25CSZ (As-sprayed)	-1.26%	-5%
25CSZ (Annealed)	-5.85%	-18%
Molybdenum (As-sprayed)	-0.25% with maximum experimental value	N/A

In Table 5-8, the percentage change in the difference obtained from experimental results and modelled results are presented. The negative sign represents the results that are below the experimental results. In most of the cases, the values obtained from the five-phase modelling are closer to the experimental values, neglecting the outliner results of 22MSZ. The results obtained using the proposed five-phase model are within 6% of experiment results.

The thermal conductivity comparison between the four-phase model and five-phase model is presented graphically in Figure 5-10. The five-phase model values are represented by blue bars and the four-phase model values are represented by grey bars. A separate comparison was performed in order to have a better understanding of different values.

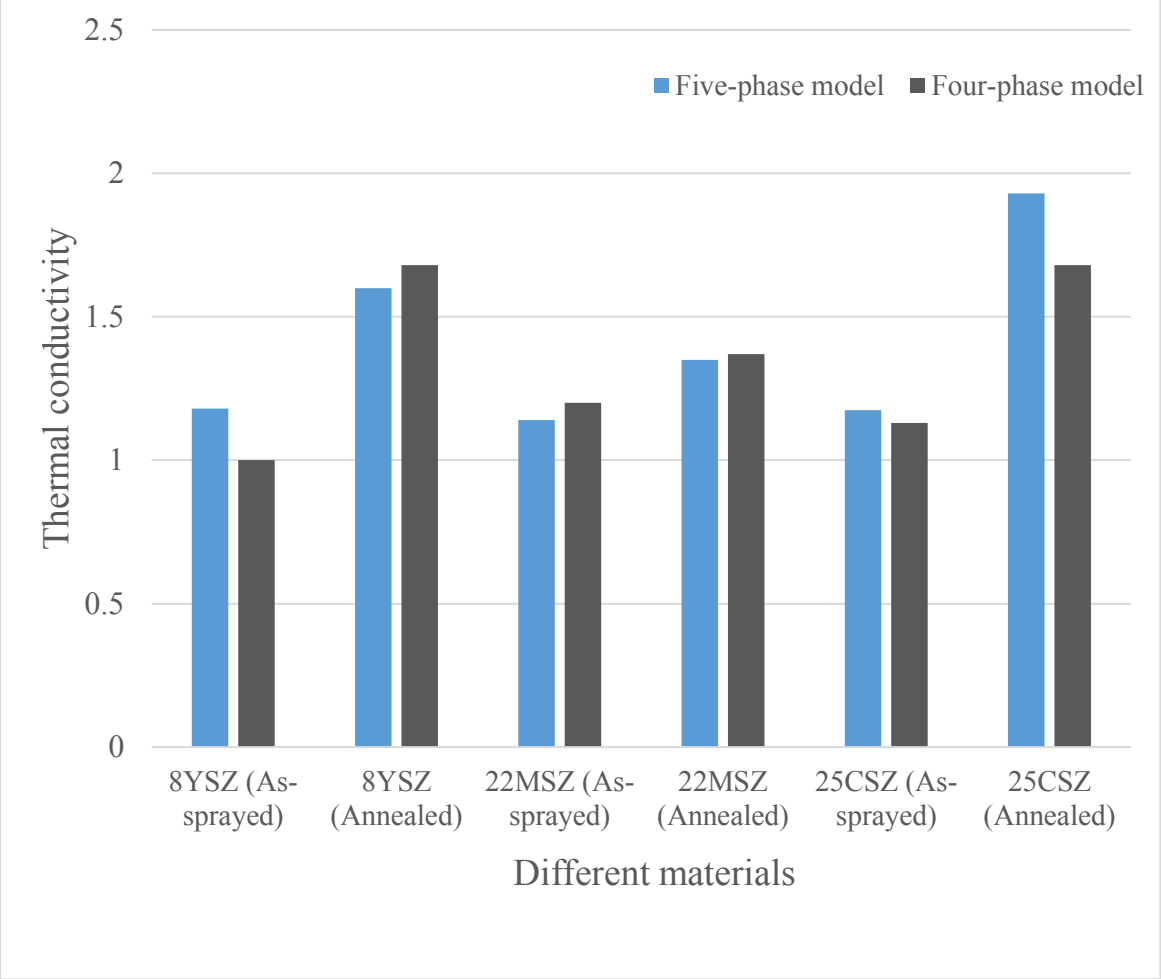

Figure 5-10 Comparison of thermal conductivity obtained from a five-phase model with four-phase model results.

Figure 5-11 provides an overall comparison of 8YSZ, 22MSZ and 25CSZ for the three different methods to measure thermal conductivity. The comparison is performed between the

results obtained from the three methods namely, the five-phase model, the four-phase model and experimental results.

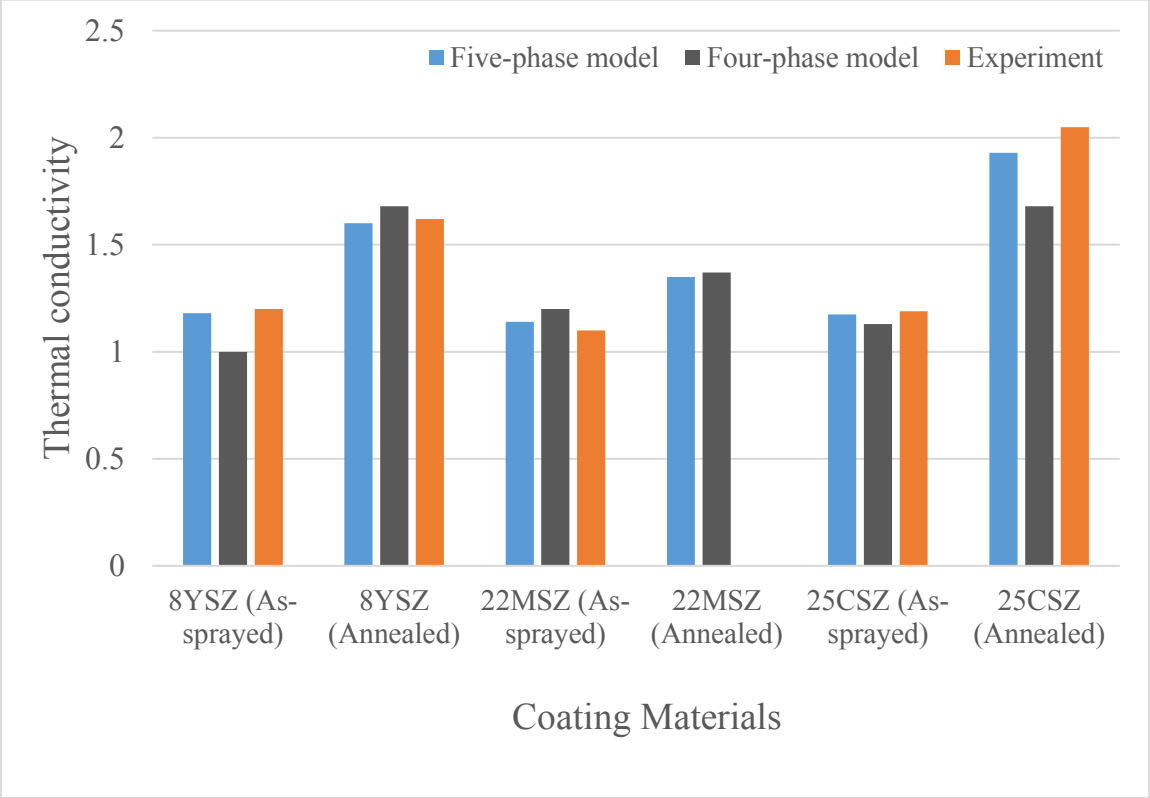

Figure 5-11 Comparison of five-phase model with four-phase model and experiment results.

In Table 5-9, thermal conductivity values obtained from three different YSZ coating materials are presented. These values were obtained from experimental results, FEA results and from the five-phase modelling. A comparison was performed between the values obtained from these three processes.

The comparison was performed for as-sprayed coatings and for annealed coatings. The results from experiment and FEA are presented as a range of values.

Table 5-9 Comparison of five-phase model with experimental and FEA results for three YSZ samples

Samples	Experimental Thermal Conductivity (W/(m.K))	Five-phase Model Thermal Conductivity (W/(m.K))	Thermal conductivity obtained from FEA (W/(m.K))
HOSP (As-sprayed)	1.10±(0.09)	1.12	1.32±(0.13)
HOSP (Annealed)	1.30±(0.1)	1.36	1.42±(0.14)
F&C (As-sprayed)	1.23±(0.1)	1.2	1.56±(0.16)
F&C (Annealed)	1.85±(0.15)	1.79	1.78±(0.18)
A&S (As-sprayed)	1.12±(0.09)	1.33	1.75±(0.18)
A&S (Annealed)	1.43±(0.11)	1.56	1.77±(0.18)

Figure 5-12 and Table 5-9 provides an overall comparison of the three different YSZ coatings, HOSP, F&C, A&S. In Figure 5-12, the orange bars represent the experimental results, the blue bars represent the values obtained from the five-phase model and the green bars represent the values obtained from FEA model. In Figure 5-12, the values obtained from Table 5-9 are plotted to make the observations between these three techniques of calculating thermal conductivity. The FEA results are obtained from the work of Y.Tan [103], [168]

The values in Table 5-10 shows the closeness of the values from the five-phase model to the experimental and FEA results. The negative percentage change represents values that are lower than the experimental and/or FEA results. It is concluded that the five-phase model predicts the thermal conductivity better than the FEA model.

Table 5-10 Difference between experimental and five-phase model results, and the difference between FEA and five-phase model results.

Samples obtained for different YSZ coatings	Difference between thermal conductivity values from experimental and five-phase model	Difference between thermal conductivity values from FEA and five-phase model
HOSP (As-sprayed)	1.2%	-15.5%
HOSP (Annealed)	4.6%	-4.2%
F&C (As-sprayed)	-2.4%	-23%
F&C (Annealed)	-3.24%	0.5%
A&S (As-sprayed)	18.7%	-24%
A&S (Annealed)	9%	-11.8%

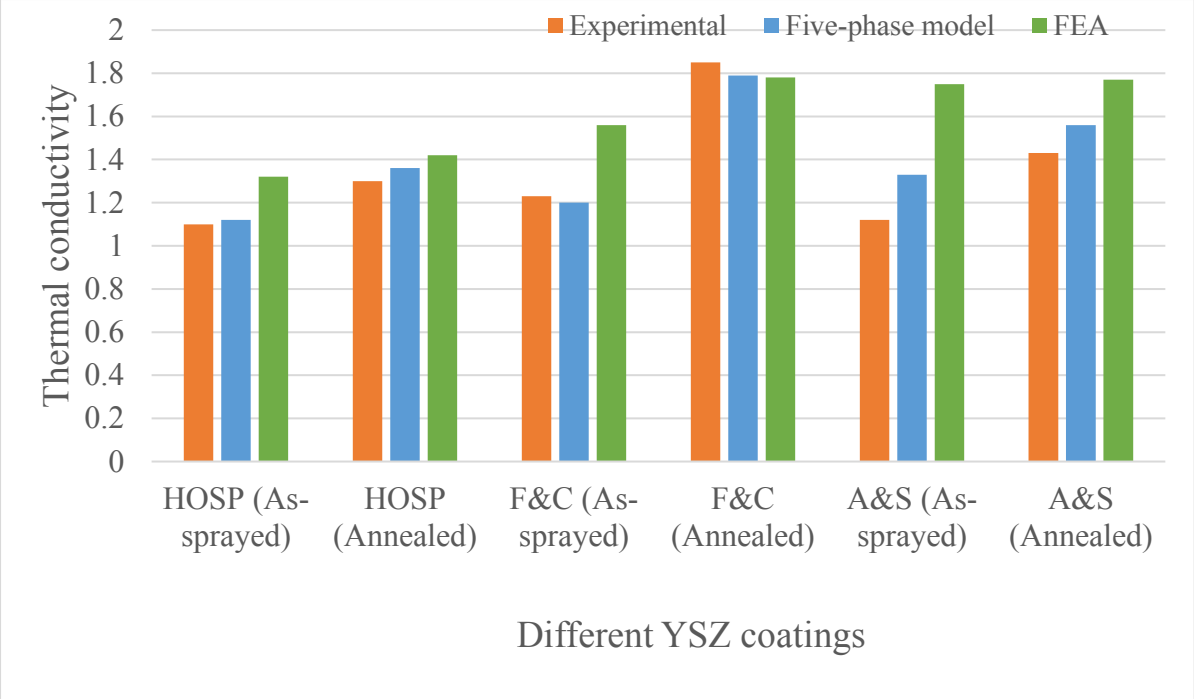

Figure 5-12 Comparison of five-phase model results with experimental and FEA results.

5.3 Results and Discussion

A five-phase model to predict thermal conductivity of thermal barrier coatings was developed in this thesis and validated against the results from the four-phase model, FEA model and experimental results. The presented model takes into consideration the different types of pores that are mostly present in a topcoat. The parameters used in the model were obtained from previous models and fitting parameters. The results obtained with the new proposed model were then validated against the reference data.

By comparing the predicted values with experimental results, it was shown that the proposed five-phase model can predict the thermal conductivity of ceramic coatings closer to the actual values. The proposed model uses real microstructure images and MIP results to obtain porosity content in the coatings to better predict the thermal conductivity. The proposed model has the potential to predict microstructure-property relationships.

The presence of different types of pores and cracks influences the overall thermal conductivity of the coatings. Microcracks present in the coating's microstructure influence the thermal conductivity. The density of microcracks is affected by heat treatment due to the expansion of the coating material. Smaller cracks disappear in the coating due to sintering and lead to lower porosity content, which ultimately leads to an increase in thermal conductivity. This was observed in all the cases presented in this thesis.

For sample coatings of molybdenum, 8YPSZ, 22MSZ, and 25CSZ, the thermal conductivity was predicted based on the porosity content present in the coatings. The five-phase model can predict the values of thermal conductivity within 6% of the experimental results. There is one exceptional case for 22MSZ, where the experimental result was much higher than the simulated value. The comparison of five-phase model results was performed with four-phase model and it was seen that value for 22MSZ for both the four-phase and five-

phase model simulations was less than the experimental result. It is possible that a faulty data source that led to an error in the experimental results. The reference data for 22MSZ was thus treated as an outlier and was neglected for a valid comparison.

In the comparison of results obtained from the four-phase model, five-phase model, and experimental data, the five-phase model predicts the values better than the four-phase model. The five-phase model predicts the value of thermal conductivity to be closer to the experimentally obtained value.

Three different YSZ coatings were modelled to predict their thermal conductivity using the five-phase model. These coatings are F&C, A&S and HOSP. The overall porosity level in these coatings was calculated using image analysis software i.e. Image J. Image J is the most trusted software to analyse the coatings microstructure using high-quality SEM images of coating microstructure.

The results obtained from the five-phase model were in accordance with experimental results. The obtained results obtained were better than those predicted by the FEA model by Y.Tan [168]. The results obtained in this thesis were validated using experimental results and the difference in predicted value and experimental results were found to be within an acceptable error range.

The five-phase model based on the porosity level in the thermal barrier coating was successfully implemented to predict the thermal conductivity of coatings. The proposed model predicts thermal conductivity values close to experimentally obtained values. The results obtained with the five-phase model are more accurate than those of the previous models (FEA and four-phase model).

The modelling approach developed in this thesis could be used as a powerful tool to model and measure the thermal conductivity of coatings and to design new coatings with an optimized microstructure to enhance the performance of TBCs.

5.4 Limitations

It was found that the five-phase model can predict the thermal conductivity better than the four-phase model and FEA models for the coatings under consideration. However, there can be certain limitations to the five-phase model. Some of these limitations are discussed in this section.

- The assumption of a non-radiating pore may not hold for all the temperatures. However, the temperature range at which the TBC is required has a very little impact on heat transfer by radiation.
- The proposed model considers the effect of defects that are independent and are dispersed within the matrix. It is assumed that the defects do not interfere with neighbouring defects.
- The effect of interconnected porosity is not truly considered in the five-phase model.
- The model is developed based on a linear relationship between the thermal conductivity and porosity. Any non-linearity in this relationship will lead to changes in the results obtained using the five-phase model.
- There can be a certain amount of error while calculating the porosity content of the coatings. This error can be due to software limitations or human errors.

6. Conclusion

The Five-phase model to predict the thermal conductivity of the ceramic coatings was developed and validated. The five-phase model can predict the thermal conductivity of thermal barrier coatings using the microstructural details obtained from SEM images. Comparison of the predicted values with the experimental values was performed and it was concluded that this model can be used as an important tool to predict and derive the thermal conductivity of ceramic coatings within an acceptable error range.

The five-phase model uses the microstructural details of the coating obtained from the image analysis using Image J and MIP to derive the thermal conductivity. Images of the microstructure can be obtained using SEM, TEM or LOM. Most of the details of the microstructure were included in this model. Image analysis helps to better understand the coating microstructure.

There are various types of defects that are present in the coating microstructure that leads to a decrease in the thermal conductivity of a coating. There are four specific types of defects that are included in this model. These defects are open randomly oriented pores, microcracks, penny-shaped cracks and non-flat porosity. Different types of defects have different effects on the thermal conductivity. The effect of different defects is calculated in this thesis.

Porous TBCs can significantly improve the thermal conductivity. The results obtained from the proposed five-phase are within a 6% error for the various coatings under consideration with some exceptions. These results are within the error range of experimental values. Therefore, new coating structures could be designed or modelled using the five-phase model.

A change in thermal conductivity values with thermal cycling was observed. This change is attributed to the sintering of the coatings. Thermal conductivity values obtained from the five-phase model are better than those obtained with the four-phase model. The proposed five-phase model can also predict the thermal conductivity value better than the FEA model under consideration.

The proposed five-phase model was developed for a certain type of coatings but with the results obtained from several different types of coating, it is concluded that the proposed model can be used to calculate thermal conductivity of most of the thermal barrier coatings using their microstructural details.

Thus, it can be concluded that the modelling approach developed in this thesis can be a powerful and effective tool to design and predict thermal conductivity. The optimized microstructure can be developed with the proposed model using several iterations and by changing the parameters each time. The optimized microstructure can significantly improve the performance and efficiency of the TBCs.

6.1 Future Work

The proposed model can be used to model and predict the thermal conductivity of thermal barrier coatings by using microstructural details. However, there are still some areas which can be improved.

- First, the effect of radiating pores can be considered to fully optimize the five-phase model.
- The number of types of defects included in this thesis was four. This number can be increased to 5 or 6 types of defects. With the increase in the number of defects, the formula to calculate the thermal conductivity will become complex and may lose its significance. The number of the equation will increase from 24 to 120 with the addition of just one more type of defect.
- Microstructural details can be obtained using more advanced techniques to remove any error in calculating thermal conductivity based on porosity.

References

[1] R. C. Reed, *The Superalloys: Fundamentals and Applications by Roger C. Reed*. Cambridge University Press, 1742.

[2] A. K. Ray and R. W. Steinbrech, "Crack propagation studies of thermal barrier coatings under bending," *J. Eur. Ceram. Soc.*, vol. 19, no. 12, pp. 2097–2109, Oct. 1999.

[3] W. J. Brindley and R. A. Miller, "Thermal barrier coating life and isothermal oxidation of low-pressure plasma-sprayed bond coat alloys," *Surf. Coat. Technol.*, vol. 43–44, no. 1–3, pp. 446–457, 1990.

[4] K. Kokini and Y. R. Takeuchi, "Initiation of surface cracks in multilayer ceramic thermal barrier coatings under thermal loads," *Mater. Sci. Eng. A*, vol. 189, no. 1, pp. 301–309, Dec. 1994.

[5] N. Roy, K. M. Godiwalla, E. S. Dwarakadasa, and A. K. Ray, "Elasto-plastic deformation in thermal barrier coated superalloys," *Scr. Mater.*, vol. 51, no. 7, pp. 739–743, Oct. 2004.

[6] A. K. Ray *et al.*, "Fatigue behavior of a thermal barrier coated superalloy at 800°C," *Mater. Sci. Eng. A*, vol. 448, no. 1, pp. 294–298, Mar. 2007.

[7] D. R. Clarke and C. G. Levi, "Materials design for the next generation thermal barrier coatings," *Annu. Rev. Mater. Res.*, vol. 33, no. 1, pp. 383–417, 2003.

[8] H. Wadley, "Wadley Research Group - UVA." 2013.

[9] S. Dutta, "Fracture toughness and reliability in high-temperature structural ceramics and composites: Prospects and challenges for the 21st century," *Bull. Mater. Sci.*, vol. 24, no. 2, pp. 117–120, Apr. 2001.

[10] R. A. Miller, "Thermal barrier coatings for aircraft engines: history and directions," *J. Therm. Spray Technol.*, vol. 6, no. 1, p. 35, Mar. 1997.

[11] J. R. Brandon and R. Taylor, “Thermal properties of ceria and yttria partially stabilized zirconia thermal barrier coatings,” *Surf. Coat. Technol.*, vol. 39–40, pp. 143–151, 1989.

[12] A. Vardelle *et al.*, “The 2016 Thermal Spray Roadmap,” *J. Therm. Spray Technol.*, vol. 25, no. 8, pp. 1376–1440, Dec. 2016.

[13] S. Bose, “Chapter 7 - Thermal barrier coatings (TBCs),” in *High Temperature Coatings*, Burlington: Butterworth-Heinemann, 2007, pp. 155–232.

[14] Q. M. Yu and Q. He, “Effect of material properties on residual stress distribution in thermal barrier coatings,” *Ceram. Int.*, Nov. 2017.

[15] A. Fahr, B. Rogé, and J. Thornton, “Detection of thermally grown oxides in thermal barrier coatings by nondestructive evaluation,” *J. Therm. Spray Technol.*, vol. 15, no. 1, pp. 46–52, Mar. 2006.

[16] H. M. Tawancy, A. I. Mohammad, L. M. Al-Hadhrami, H. Dafalla, and F. K. Alyousf, “On the performance and failure mechanism of thermal barrier coating systems used in gas turbine blade applications: Influence of bond coat/superalloy combination,” *Eng. Fail. Anal.*, vol. 57, pp. 1–20, Nov. 2015.

[17] R. A. Miller, “Current status of thermal barrier coatings — An overview,” *Surf. Coat. Technol.*, vol. 30, no. 1, pp. 1–11, 1987.

[18] X. F. Zhang *et al.*, “Enhanced properties of Al-modified EB-PVD 7YSZ thermal barrier coatings,” *Ceram. Int.*, vol. 42, no. 12, pp. 13969–13975, 2016.

[19] L. Wang *et al.*, “Influence of pores on the thermal insulation behavior of thermal barrier coatings prepared by atmospheric plasma spray,” *Mater. Des.*, vol. 32, no. 1, pp. 36–47, 2011.

[20] J. Zhang and V. Desai, “Evaluation of thickness, porosity and pore shape of plasma sprayed TBC by electrochemical impedance spectroscopy,” *Surf. Coat. Technol.*, vol. 190, no. 1, pp. 98–109, 2005.

[21] J. Wang *et al.*, “Effect of spraying power on microstructure and property of nanostructured YSZ thermal barrier coatings,” *J. Alloys Compd.*, vol. 730, no. Supplement C, pp. 471–482, Jan. 2018.

[22] D. R. Clarke, M. Oechsner, and N. P. Padture, “Thermal-barrier coatings for more efficient gas-turbine engines,” *MRS Bull.*, vol. 37, no. 10, pp. 891–898, Oct. 2012.

[23] G.-R. Li, G.-J. Yang, C.-X. Li, and C.-J. Li, “A comprehensive mechanism for the sintering of plasma-sprayed nanostructured thermal barrier coatings,” *Ceram. Int.*, vol. 43, no. 13, pp. 9600–9615, Sep. 2017.

[24] S. Sampath, V. Srinivasan, A. Valarezo, A. Vaidya, and T. Streibl, “Sensing, Control, and In Situ Measurement of Coating Properties: An Integrated Approach Toward Establishing Process-Property Correlations,” *J. Therm. Spray Technol.*, vol. 18, no. 2, pp. 243–255, Jun. 2009.

[25] W. Chi, “Thermal transport properties of thermally sprayed coatings: An integrated study of materials, processing and microstructural effects.,” Stony Brook University, 2007.

[26] S. Mahade, N. Curry, S. Björklund, N. Markocsan, and P. Nylén, “Engineered thermal barrier coatings deposited by suspension plasma spray,” *Mater. Lett.*, vol. 209, no. Supplement C, pp. 517–521, Dec. 2017.

[27] V. Kumar and B. Kandasubramanian, “Processing and design methodologies for advanced and novel thermal barrier coatings for engineering applications,” *Particuology*, vol. 27, no. Supplement C, pp. 1–28, Aug. 2016.

[28] F. Fanicchia, D. A. Axinte, J. Kell, R. McIntyre, G. Brewster, and A. D. Norton, “Combustion Flame Spray of CoNiCrAlY & YSZ coatings,” *Surf. Coat. Technol.*, vol. 315, no. Supplement C, pp. 546–557, Apr. 2017.

[29] W. R. Chen, X. Wu, B. R. Marple, and P. C. Patnaik, “Oxidation and crack nucleation/growth in an air-plasma-sprayed thermal barrier coating with NiCrAlY bond coat,” *Surf. Coat. Technol.*, vol. 197, no. 1, pp. 109–115, 2005.

[30] D. Zhang, “1 - Thermal barrier coatings prepared by electron beam physical vapor deposition (EB–PVD),” in *Thermal Barrier Coatings*, Woodhead Publishing, 2011, pp. 3–24.

[31] J. Zhang, X. Guo, Y.-G. Jung, L. Li, and J. Knapp, “Lanthanum zirconate based thermal barrier coatings: A review,” *Surf. Coat. Technol.*, vol. 323, no. Supplement C, pp. 18–29, Aug. 2017.

[32] X. Chen *et al.*, “Columnar and DVC-structured thermal barrier coatings deposited by suspension plasma spray: high-temperature stability and their corrosion resistance to the molten salt,” *Ceram. Int.*, vol. 42, no. 15, pp. 16822–16832, Nov. 2016.

[33] B. Zhang, L. Wei, H. Guo, and H. Xu, “Microstructures and deposition mechanisms of quasi-columnar structured yttria-stabilized zirconia coatings by plasma spray physical vapor deposition,” *Ceram. Int.*, vol. 43, no. 15, pp. 12920–12929, Oct. 2017.

[34] D. A. G. Bruggeman, “Berechnung verschiedener physikalischer Konstanten von heterogenen Substanzen. I. Dielektrizitätskonstanten und Leitfähigkeiten der Mischkörper aus isotropen Substanzen,” *Ann. Phys.*, vol. 416, pp. 636–664, 1935.

[35] W. A. Nelson and R. M. Orenstein, “TBC experience in land- based gas turbines,” *J. Therm. Spray Technol.*, vol. 6, no. 2, pp. 176–180, Jun. 1997.

[36] J. Cho, J. Park, and J. An, “Low thermal conductivity of atomic layer deposition yttria-stabilized zirconia (YSZ) thin films for thermal insulation applications,” *J. Eur. Ceram. Soc.*, vol. 37, no. 9, pp. 3131–3136, Aug. 2017.

[37] X. Wang, S. Guo, L. Zhao, Y. Zhu, and L. Ai, “A novel thermal barrier coating for high-temperature applications,” *Ceram. Int.*, vol. 42, no. 2, Part A, pp. 2648–2653, Feb. 2016.

[38] F. Zhou *et al.*, “Thermal cycling behavior of nanostructured 8YSZ, SZ/8YSZ and 8CSZ/8YSZ thermal barrier coatings fabricated by atmospheric plasma spraying,” *Ceram. Int.*, vol. 43, no. 5, pp. 4102–4111, Apr. 2017.

[39] J. Jiang, Z. Zou, W. Wang, X. Zhao, Y. Liu, and Z. Cao, “Effect of internal oxidation on the interfacial morphology and residual stress in air plasma sprayed thermal barrier coatings,” *Surf. Coat. Technol.*, vol. 334, no. Supplement C, pp. 215–226, Jan. 2018.

[40] L. Su and C. Yi, “Effects of CMAS penetration on the delamination cracks in EB-PVD thermal barrier coatings with curved interface,” *Ceram. Int.*, vol. 43, no. 12, pp. 8893–8897, Aug. 2017.

[41] W. Fan and Y. Bai, “Review of suspension and solution precursor plasma sprayed thermal barrier coatings,” *Ceram. Int.*, vol. 42, no. 13, pp. 14299–14312, Oct. 2016.

[42] R. A. Miller, “History of Thermal Barrier Coatings for Gas Turbine Engines: Emphasizing NASA’s Role from 1942 to 1990,” presented at the Thermal Barrier Coatings II, Engineering Conference International, KlosterIree, Germany, 2009.

[43] S. Stecura, “Two-layer thermal barrier coating for turbine airfoils - furnace and burner rig test results,” Sep. 1976.

[44] S. Stecura, “Effects of compositional changes on the performance of a thermal barrier coating system. [yttria-stabilized zirconia coatings on gas turbine engine blades],” presented at the Ann. Conf. on Composite and Advanced Mater., 21-24 Jan. 1979, United States, 1978.

[45] “Study of the coating stability of a TBC system,” *Mater. High Temp.*, vol. 17, no. 2, pp. 197–203, 2000.

[46] Z. Xu, X. Zhou, R. Mu, and L. He, “Structure, phase stability and thermophysical properties of (Yb0.1La0.9)2(Zr0.7Ce0.3)2O7 ceramics,” *Mater. Lett.*, vol. 135, no. Supplement C, pp. 162–164, Nov. 2014.

[47] X. Zhong *et al.*, “Improvement in thermal shock resistance of gadolinium zirconate coating by addition of nanostructured yttria partially-stabilized zirconia,” *Ceram. Int.*, vol. 41, no. 6, pp. 7318–7324, Jul. 2015.

[48] M. Peters, K. Fritscher, G. Staniek, W. A. Kaysser, and U. Schulz, “Design and Properties of Thermal Barrier Coatings for advanced turbine engines,” *Mater. Werkst.*, vol. 28, no. 8, pp. 357–362, 1997.

[49] M. Gell, D. N. Duhl, D. K. Gupta, and K. D. Sheffler, “Advanced Superalloy Airfoils,” *JOM*, vol. 39, no. 7, pp. 11–15, Jul. 1987.

[50] M. Y. Ali, S. Q. Nusier, and G. M. Newaz, “Creep effects on early damage initiation in a TBC system,” *J. Mater. Sci.*, vol. 39, no. 10, pp. 3383–3390, 2004.

[51] L. Xu, W. Wang, T. Gao, X. Shi, J. Gao, and W. Liang, “Experimental study on cooling performance of a steam-cooled turbine blade with five internal cooling smooth channels,” *Exp. Therm. Fluid Sci.*, vol. 58, no. Supplement C, pp. 180–187, Oct. 2014.

[52] S. Stecura, “Advanced thermal barrier system bond coatings for use on nickel-, cobalt- and iron-base alloy substrates,” *Thin Solid Films*, vol. 136, no. 2, pp. 241–256, Feb. 1986.

[53] T. H, “Physical chemistry . W.J. Moore, Longman, London, 5th edition, 1972, pp. xiii + 977, price £3.75,” *J. Mol. Struct.*, vol. 17, pp. 434–435, Aug. 1973.

[54] M. Arai, H. Ochiai, and T. Suidzu, “A novel low-thermal-conductivity plasma-sprayed thermal barrier coating controlled by large pores,” *Surf. Coat. Technol.*, vol. 285, no. Supplement C, pp. 120–127, Jan. 2016.

[55] M. Zhao, W. Pan, C. Wan, Z. Qu, Z. Li, and J. Yang, “Defect engineering in development of low thermal conductivity materials: A review,” *J. Eur. Ceram. Soc.*, vol. 37, no. 1, pp. 1–13, Jan. 2017.

[56] L. Xu, S. Bo, Y. Hongde, and W. Lei, “Evolution of Rolls-royce Air-cooled Turbine Blades and Feature Analysis,” *Procedia Eng.*, vol. 99, no. Supplement C, pp. 1482–1491, Jan. 2015.

[57] U. Schulz, “Phase Transformation in EB-PVD Yttria Partially Stabilized Zirconia Thermal Barrier Coatings during Annealing,” *J. Am. Ceram. Soc.*, vol. 83, no. 4, pp. 904–910, Apr. 2000.

[58] A. C. Fox and T. W. Clyne, “Oxygen transport by gas permeation through the zirconia layer in plasma sprayed thermal barrier coatings,” *Surf. Coat. Technol.*, vol. 184, no. 2–3, pp. 311–321, Jun. 2004.

[59] R. Streiff, O. Cerclier, and D. H. Boone, “Structure and hot corrosion behavior of platinum-modified aluminide coatings,” *Surf. Coat. Technol.*, vol. 32, no. 1–4, pp. 111–126, Nov. 1987.

[60] K. Ma and J. M. Schoenung, “Isothermal oxidation behavior of cryomilled NiCrAlY bond coat: Homogeneity and growth rate of TGO,” *Surf. Coat. Technol.*, vol. 205, no. 21, pp. 5178–5185, Aug. 2011.

[61] I. Spitsberg and K. More, “Effect of thermally grown oxide (TGO) microstructure on the durability of TBCs with PtNiAl diffusion bond coats,” *Mater. Sci. Eng. A*, vol. 417, no. 1, pp. 322–333, Feb. 2006.

[62] X. Fang, G. Zhang, and X. Feng, “Performance of TBCs system due to the different thicknesses of top ceramic layer,” *Ceram. Int.*, vol. 41, no. 2, Part B, pp. 2840–2846, Mar. 2015.

[63] M. J. Lance, J. A. Haynes, and B. A. Pint, “The effects of temperature and substrate curvature on TBC lifetime and residual stress in alumina scales beneath APS YSZ,” *Surf. Coat. Technol.*, vol. 308, no. Supplement C, pp. 19–23, Dec. 2016.

[64] R. G. Wellman, J. R. Nicholls, and K. Murphy, “Effect of microstructure and temperature on the erosion rates and mechanisms of modified EB PVD TBCs,” *Wear*, vol. 267, no. 11, pp. 1927–1934, Oct. 2009.

[65] V. Lughi, V. K. Tolpygo, and D. R. Clarke, “Microstructural aspects of the sintering of thermal barrier coatings,” *Mater. Sci. Eng. A*, vol. 368, no. 1–2, pp. 212–221, Mar. 2004.

[66] A. G. Evans, D. R. Mumm, J. W. Hutchinson, G. H. Meier, and F. S. Pettit, “Mechanisms controlling the durability of thermal barrier coatings,” *Prog. Mater. Sci.*, vol. 46, no. 5, pp. 505–553, Jan. 2001.

[67] A. G. Evans, D. R. Clarke, and C. G. Levi, “The influence of oxides on the performance of advanced gas turbines,” *J. Eur. Ceram. Soc.*, vol. 28, no. 7, pp. 1405–1419, 2008.

[68] C. G. Levi, E. Sommer, S. G. Terry, A. Catanoiu, and M. Rühle, “Alumina Grown during Deposition of Thermal Barrier Coatings on NiCrAlY,” *J. Am. Ceram. Soc.*, vol. 86, no. 4, pp. 676–85, Apr. 2003.

[69] G. C. Rybicki and J. L. Smialek, “Effect of the theta-alpha-Al2O3 transformation on the oxidation behavior of beta-NiAl+Zr,” *Oxid. Met.*, pp. 275–304, Apr. 1989.

[70] V. K. Tolpygo and D. R. Clarke, “Microstructural study of the theta-alpha transformation in alumina scales formed on nickel-aluminides,” *Mater. High Temp.*, vol. 17, no. 1, pp. 59–70, Jan. 2000.

[71] R. McPherson, “A review of microstructure and properties of plasma sprayed ceramic coatings,” *Surf. Coat. Technol.*, vol. 39, pp. 173–181, Dec. 1989.

[72] D. Li *et al.*, “Microstructure formed by suspension plasma spraying: From YSZ splat to coating,” *Ceram. Int.*, vol. 43, no. 10, pp. 7488–7496, Jul. 2017.

[73] L. Wang *et al.*, "Effect of interface on the thermal conductivity of thermal barrier coatings: A numerical simulation study," *Int. J. Heat Mass Transf.*, vol. 79, pp. 954–967, Dec. 2014.

[74] Z. Ahmad, A. U. Khan, R. Farooq, T. Saif, and N. R. Mastoi, "Mechanism of Corrosion and Erosion Resistance of Plasma- Sprayed Nanostructured Coatings," 2016.

[75] H. Berndt, A.-Q. Zeng, H.-R. Stock, and P. Mayr, "Zirconium carbonitride films produced by plasma-assisted metal organic chemical vapour deposition," *Surf. Coat. Technol.*, vol. 74, pp. 369–374, Sep. 1995.

[76] W. D. Kingery, H. K. Bowen, and D. R. Uhlmann, *Introduction to Ceramics, 2nd Edition*, 2 edition. New York: Wiley-Interscience, 1976.

[77] E. Reinhold, P. Botzler, and C. Deus, "EB-PVD process management for highly productive zirconia thermal barrier coating of turbine blades," *Surf. Coat. Technol.*, vol. 120–121, pp. 77–83, 1999.

[78] S. M. Meier, D. K. Gupta, and K. D. Sheffler, "Ceramic thermal barrier coatings for commercial gas turbine engines," *JOM*, vol. 43, no. 3, pp. 50–53, Mar. 1991.

[79] U. Schulz and M. Schmücker, "Microstructure of ZrO2 thermal barrier coatings applied by EB-PVD," *Mater. Sci. Eng. A*, vol. 276, no. 1–2, pp. 1–8, 2000.

[80] A. A. Tchizhik, A. I. Rybnikov, I. S. Malashenko, S. A. Leontiev, and A. S. Osyka, "The effect of EB PVD coatings on structure and properties of nickel-base superalloy for gas turbine blades," *Surf. Coat. Technol.*, vol. 78, no. 1–3, pp. 113–123, 1996.

[81] P. Mechnich, W. Braue, and U. Schulz, "High-Temperature Corrosion of EB-PVD Yttria Partially Stabilized Zirconia Thermal Barrier Coatings with an Artificial Volcanic Ash Overlay," *J. Am. Ceram. Soc.*, vol. 94, no. 3, pp. 925–931, Mar. 2011.

[82] V. Lughi and D. R. Clarke, “Low-temperature transformation kinetics of electron-beam deposited 5wt.% yttria-stabilized zirconia,” *Acta Mater.*, vol. 55, no. 6, pp. 2049–2055, Apr. 2007.

[83] U. Saral and N. Toplan, “Thermal cycle properties of plasma sprayed YSZ/Al2O3 thermal barrier coatings,” *Surf. Eng.*, vol. 25, no. 7, pp. 541–547, 2009.

[84] R. Prabu, S. Ramesh, M. Savitha, and M. Balachandar, “Review of physical vapour deposition (PVD) techniques,” in *Proceedings of the International Conference on“Sustainable Manufacturing,”* 2013.

[85] K. Matsumoto, Y. Itoh, and T. Kameda, “EB-PVD process and thermal properties of hafnia-based thermal barrier coating,” *Sci. Technol. Adv. Mater.*, vol. 4, no. 2, pp. 153–158, 2003.

[86] R. V. Hillery, B. H. Pilsner, and R. L. McKnight, “Thermal barrier coating life prediction model development,” NASA, Ohio, 180807, 1988.

[87] A. Maricocchi, A. Bartz, and D. Wortman, “PVD TBC experience on GE aircraft engines,” *J. Therm. Spray Technol.*, vol. 6, no. 2, pp. 193–198, 1997.

[88] J. R. Nicholls, K. J. Lawson, A. Johnstone, and D. S. Rickerby, “Methods to reduce the thermal conductivity of EB-PVD TBCs,” *Surf. Coat. Technol.*, vol. 151–152, pp. 383–391, Mar. 2002.

[89] R. Vaßen, F. Traeger, and D. Stöver, “Correlation between spraying conditions and microcrack density and their influence on thermal cycling life of thermal barrier coatings,” *J. Therm. Spray Technol.*, vol. 13, no. 3, pp. 396–404, Sep. 2004.

[90] U. Schulz *et al.*, “Some recent trends in research and technology of advanced thermal barrier coatings,” *Aerosp. Sci. Technol.*, vol. 7, no. 1, pp. 73–80, Jan. 2003.

[91] R. J. Oram and E. G. Wolff, “Simple Guarded Hot Plate Technique for Making Thermal Conductivity Measurements of Composite Materials at Cryogenic Temperatures,” in *Advances in Cryogenic Engineering Materials*, Springer, Boston, MA, 1998, pp. 349–357.

[92] W. Chi, S. Sampath, and H. Wang, “Comparison of the Thermal Transport Property Measurements of Thermally Sprayed Coatings by the Laser and Xenon Flash Techniques,” *J. Therm. Spray Technol.*, vol. 16, no. 3, pp. 444–448, 2007.

[93] S. R. Casolco, J. Xu, and J. E. Garay, “Transparent/translucent polycrystalline nanostructured yttria stabilized zirconia with varying colors,” *Scr. Mater.*, vol. 58, no. 6, pp. 516–519, 2008.

[94] M. Gupta, N. Curry, P. Nylén, N. Markocsan, and R. Vaßen, “Design of next generation thermal barrier coatings — Experiments and modelling,” *Surf. Coat. Technol.*, vol. 220, pp. 20–26, Apr. 2013.

[95] E. Litovskii, I. Zborovskii, and I. Uspenskii, “On the temperature dependence of the thermal conductivity of ceramic materials with rarefaction of the gas medium,” *J. Eng. Phys.*, vol. 27, no. 4, pp. 1225–1230, 1974.

[96] D. Zhu and R. A. Miller, “Thermal-Barrier Coatings for Advanced Gas-Turbine Engines,” *MRS Bull.*, vol. 25, no. 7, pp. 43–47, Jul. 2000.

[97] W. Chi, S. Sampath, and H. Wang, “Ambient and high-temperature thermal conductivity of thermal sprayed coatings,” *J. Therm. Spray Technol.*, vol. 15, no. 4, pp. 773–778, 2006.

[98] K. W. Schlichting, N. P. Padture, and P. G. Klemens, “Thermal conductivity of dense and porous yttria-stabilized zirconia,” *J. Mater. Sci.*, vol. 36, no. 12, pp. 3003–3010, Jun. 2001.

[99] L. Pawlowski and P. Fauchais, “Thermal transport properties of thermally sprayed coatings,” *Int. Mater. Rev.*, vol. 37, no. 1, pp. 271–289, Jan. 1992.

[100] Y. S. Touloukian, *Thermal conductivity: nonmetallic solids*. New York: IFI/Plenum, 1970.

[101] T. Ashworth and D. R. Smith, *Thermal Conductivity 18*, Softcover reprint of the original 1st ed. 1985 edition. Springer, 2012.

[102] N. L. Vočadlo and G. D. Price, "The Grüneisen parameter — computer calculations via lattice dynamics," *Phys. Earth Planet. Inter.*, vol. 82, no. 3–4, pp. 261–270, Mar. 1994.

[103] Y. Tan, J. P. Longtin, and S. Sampath, "Modeling thermal conductivity of thermal spray coatings: comparing predictions to experiments," *J. Therm. Spray Technol.*, vol. 15, no. 4, pp. 545–552, Dec. 2006.

[104] D. S. Almeida, C. R. M. Silva, M. do C. de A. Nono, and C. A. A. Cairo, "Electron Beam-Physical Vapour Deposition of Zirconia Co-Doped with Yttria and Niobia," *Mater. Sci. Forum*, vol. 498–499, pp. 453–458, 2005.

[105] S. Raghavan, H. Wang, R. B. Dinwiddie, W. D. Porter, and M. J. Mayo, "The effect of grain size, porosity and yttria content on the thermal conductivity of nanocrystalline zirconia," *Scr. Mater.*, vol. 39, no. 8, pp. 1119–1125, Sep. 1998.

[106] S. Alprine, M. Derrien, Y. Jaslier, and R. Mavrel, "Thermal barrier coatings: the thermal conductivity challenge," *Proc. 85th Meet. AGARD Struct. Mater. Panel Aalb.*, 1997.

[107] S. Fabris, A. T. Paxton, and M. W. Finnis, "A stabilization mechanism of zirconia based on oxygen vacancies only," *Acta Mater.*, vol. 50, no. 20, pp. 5171–5178, 2002.

[108] G. Pezzotti, M. C. Munisso, A. A. Porporati, and K. Lessnau, "On the role of oxygen vacancies and lattice strain in the tetragonal to monoclinic transformation in alumina/zirconia composites and improved environmental stability," *Biomaterials*, vol. 31, no. 27, pp. 6901–6908, Sep. 2010.

[109] G. E. Youngblood, R. W. Rice, and R. P. Ingel, “Thermal Diffusivity of Partially and Fully Stabilized (Yttria) Zirconia Single Crystals,” *J. Am. Ceram. Soc.*, vol. 71, no. 4, pp. 255–260, Apr. 1988.

[110] S. Wei, W. Fu-chi, F. Qun-Bo, and M. Zhuang, “Effects of defects on the effective thermal conductivity of thermal barrier coatings,” *Appl. Math. Model.*, vol. 36, no. 5, pp. 1995–2002, May 2012.

[111] Z. Wang, A. Kulkarni, S. Deshpande, T. Nakamura, and H. Herman, “Effects of pores and interfaces on effective properties of plasma sprayed zirconia coatings,” *Acta Mater.*, vol. 51, no. 18, pp. 5319–5334, Oct. 2003.

[112] P. G. Klemens, “Phonon scattering and thermal resistance due to grain boundaries,” *Int. J. Thermophys.*, vol. 15, no. 6, pp. 1345–1351, Nov. 1994.

[113] J. Mao, Y. Wang, Z. Liu, B. Ge, and Z. Ren, “Phonon scattering by nanoscale twin boundaries,” *Nano Energy*, vol. 32, no. Supplement C, pp. 174–179, Feb. 2017.

[114] M. Yang *et al.*, “Effect of five kinds of pores shape on thermal stress properties of thermal barrier coatings by finite element method,” *Ceram. Int.*, vol. 43, no. 13, pp. 9664–9678, Sep. 2017.

[115] M. Zhao and W. Pan, “Effect of lattice defects on thermal conductivity of Ti-doped, Y2O3-stabilized ZrO2,” *Acta Mater.*, vol. 61, no. 14, pp. 5496–5503, 2013.

[116] E. Y. Litovsky and M. Shapiro, “Gas Pressure and Temperature Dependences of Thermal Conductivity of Porous Ceramic Materials: Part 1, Refractories and Ceramics with Porosity below 30%,” *J. Am. Ceram. Soc.*, vol. 75, no. 12, pp. 3425–3439, Dec. 1992.

[117] H. J. Ratzer-Scheibe, U. Schulz, and T. Krell, “The effect of coating thickness on the thermal conductivity of EB-PVD PYSZ thermal barrier coatings,” *Surf. Coat. Technol.*, vol. 200, no. 18–19, pp. 5636–5644, 2006.

[118] “NATO Research & Technology Organization Publications : NATO Collection.” [Online]. Available: http://nato-pubs.ekt.gr/NATORTO/handle/123456789/4723. [Accessed: 07-Feb-2017].

[119] H. S. Zhang, S. R. Liao, Y. Wei, and S. K. Guan, “Methods to Reduce Thermal Conductivity Further of Plasma Sprayed Thermal Barrier Coatings,” *Adv. Mater. Res.*, vol. 230–232, pp. 49–53, 2011.

[120] Y. A. Tamarin, E. B. Kachanov, and S. V. Zherzdev, “Thermophysical Properties of Ceramic Layers in TBC-EB,” *Mater. Sci. Forum*, vol. 251–254, pp. 949–956, 1997.

[121] J. Singh, D. E. Wolfe, R. A. Miller, J. I. Eldridge, and D.-M. Zhu, “Tailored microstructure of zirconia and hafnia-based thermal barrier coatings with low thermal conductivity and high hemispherical reflectance by EB-PVD,” *J. Mater. Sci.*, vol. 39, no. 6, pp. 1975–1985, 2004.

[122] B. H. Kear and W. E. Mayo, “Thermal Sprayed Nanostructured Hard Coatings,” in *Nanostructured Films and Coatings*, Springer, Dordrecht, 2000, pp. 113–129.

[123] K. Wang, H. Peng, H. Guo, and S. Gong, “Effect of Sintering on Thermal Conductivity and Thermal Barrier Effects of Thermal Barrier Coatings,” *Chin. J. Aeronaut.*, vol. 25, no. 5, pp. 811–816, Oct. 2012.

[124] H. J. Ratzer-Scheibe and U. Schulz, “The effects of heat treatment and gas atmosphere on the thermal conductivity of APS and EB-PVD PYSZ thermal barrier coatings,” *Surf. Coat. Technol.*, vol. 201, no. 18, pp. 7880–7888, 2007.

[125] N. Wang, C. Zhou, S. Gong, and H. Xu, “Heat treatment of nanostructured thermal barrier coating,” *Ceram. Int.*, vol. 33, no. 6, pp. 1075–1081, 2007.

[126] P. L. Kapitza, “Heat Transfer and Superfluidity of Helium II,” *Phys. Rev.*, vol. 60, no. 4, pp. 354–355, Aug. 1941.

[127] M. Gupta, K. Skogsberg, and P. Nylén, “Influence of Topcoat-Bondcoat Interface Roughness on Stresses and Lifetime in Thermal Barrier Coatings,” *J. Therm. Spray Technol.*, vol. 23, no. 1–2, pp. 170–181, Jan. 2014.

[128] L. Liu, H. Zhang, X. Lei, and Y. Zheng, “Dependence of microstructure and thermal conductivity of EB-PVD thermal barrier coatings on the substrate rotation speed,” *Phys. Procedia*, vol. 18, pp. 206–210, 2011.

[129] J. C. Y. Koh and A. Fortini, “Prediction of thermal conductivity and electrical resistivity of porous metallic materials,” *Int. J. Heat Mass Transf.*, vol. 16, no. 11, pp. 2013–2022, Nov. 1973.

[130] R. Gaumé, B. Viana, D. Vivien, J.-P. Roger, and D. Fournier, “A simple model for the prediction of thermal conductivity in pure and doped insulating crystals,” *Appl. Phys. Lett.*, vol. 83, no. 7, pp. 1355–1357, Aug. 2003.

[131] E. Ahmadloo and S. Azizi, “Prediction of thermal conductivity of various nanofluids using artificial neural network,” *Int. Commun. Heat Mass Transf.*, vol. 74, pp. 69–75, May 2016.

[132] B. K. Jang, “Thermal conductivity of nanoporous ZrO2-4 mol% Y2O3 multilayer coatings fabricated by EB-PVD,” *Surf. Coat. Technol.*, vol. 202, no. 8, pp. 1568–1573, 2008.

[133] Y. Lang, Y. Dong, J. Zhou, and C.-A. Wang, “YSZ fiber-reinforced porous YSZ ceramics with lowered thermal conductivity: Influence of the sintering temperature,” *Mater. Sci. Eng. A*, vol. 600, pp. 76–81, Apr. 2014.

[134] J. C. Maxwell, *A Treatise on Electricity and Magnetism, Vol. 1*, 3rd ed. edition. New York: Dover Publications, 1954.

[135] P. G. Klemens, “Effective thermal conductivity of a matrix with two kinds of inclusions,” *Int. J. Thermophys.*, vol. 17, no. 4, pp. 979–981, Jul. 1996.

[136] D. P. H. Hasselman, “Effect of Cracks on Thermal Conductivity,” *J. Compos. Mater.*, vol. 12, no. 4, pp. 403–407, 1978.

[137] S. Banisi, J. A. Finch, and A. R. Laplante, “Electrical conductivity of dispersions: A review,” *Miner. Eng.*, vol. 6, no. 4, pp. 369–385, Apr. 1993.

[138] R. McPherson, “A model for the thermal conductivity of plasma-sprayed ceramic coatings,” *Thin Solid Films*, vol. 112, no. 1, pp. 89–95, 1984.

[139] C.-J. Li and A. Ohmori, “Relationships between the microstructure and properties of thermally sprayed deposits,” *J. Therm. Spray Technol.*, vol. 11, no. 3, pp. 365–374, 2002.

[140] S. Boire-Lavigne, C. Moreau, and R. Saint-Jacques, “The relationship between the microstructure and thermal diffusivity of plasma-sprayed tungsten coatings,” *J. Therm. Spray Technol.*, vol. 4, no. 3, pp. 261–267, 1995.

[141] I. Sevostianov and M. Kachanov, “Anisotropic thermal conductivities of plasma-sprayed thermal barrier coatings in relation to the microstructure,” *J. Therm. Spray Technol.*, vol. 9, no. 4, pp. 478–482, Dec. 2000.

[142] T. J. Lu, C. G. Levi, H. N. G. Wadley, and A. G. Evans, “Distributed Porosity as a Control Parameter for Oxide Thermal Barriers Made by Physical Vapor Deposition,” *J. Am. Ceram. Soc.*, vol. 84, no. 12, pp. 2937–2946, 2001.

[143] A. Kulkarni *et al.*, “Comprehensive microstructural characterization and predictive property modeling of plasma-sprayed zirconia coatings,” *Acta Mater.*, vol. 51, no. 9, pp. 2457–2475, May 2003.

[144] K. J. Hollis, “Pore Phase Mapping and Finite-Element Modeling of Plasma Sprayed Tungsten Coatings,” Dec. 1995.

[145] J. M. Dorvaux, O. Lavigne, R. Mevrel, M. Poulain, Y. Renollet, and C. Rio, “Modelling the thermal conductivity of thermal barrier coatings. Proceedings of the 85th Meeting of

the AGARD Structures and Materials Panel," Aalborg, Denmark, NATO-AGARD-R-823, 1997.

[146] B. Saint-Ramond, "HITS - High Insulation Thermal Barrier Coating systems," *Air Space Eur.*, vol. 3, no. 3, pp. 174–177, May 2001.

[147] M. Bartsch, U. Schulz, J.-M. Dorvaux, O. Lavigne, E. R. Fuller, and S. A. Langer, "Simulating Thermal Response of Eb-Pvd Thermal Barrier Coating Microstructures," in *27th Annual Cocoa Beach Conference on Advanced Ceramics and Composites: A: Ceramic Engineering and Science Proceedings*, W. M. Kriven and H.-T. Lin, Eds. John Wiley & Sons, Inc., 2003, pp. 549–554.

[148] F. Qunbo, W. Fuchi, W. Lu, and M. Zhuang, "Microstructure-Based Prediction of Properties for Thermal Barrier Coatings." Beijing Institute of Technology, 2009.

[149] Y. Dong, C.-A. Wang, J. Zhou, and Z. Hong, "A novel way to fabricate highly porous fibrous YSZ ceramics with improved thermal and mechanical properties," *J. Eur. Ceram. Soc.*, vol. 32, no. 10, pp. 2213–2218, Aug. 2012.

[150] L. Wang *et al.*, "Design and optimization of coating structure for the thermal barrier coatings fabricated by atmospheric plasma spraying via finite element method," *J. Asian Ceram. Soc.*, vol. 2, no. 2, pp. 102–116, Jun. 2014.

[151] H. Xu and H. Guo, Eds., *Thermal Barrier Coatings*, 1 edition. Woodhead Publishing, 2011.

[152] M. Kachanov and I. Sevostianov, "On quantitative characterization of microstructures and effective properties," *Int. J. Solids Struct.*, vol. 42, no. 2, pp. 309–336, Jan. 2005.

[153] F. Cernuschi, S. Ahmaniemi, P. Vuoristo, and T. Mäntylä, "Modelling of thermal conductivity of porous materials: application to thick thermal barrier coatings," *J. Eur. Ceram. Soc.*, vol. 24, no. 9, pp. 2657–2667, Aug. 2004.

[154] P. Scardi, M. Leoni, F. Cernuschi, and A. Figari, “Microstructure and Heat Transfer Phenomena in Ceramic Thermal Barrier Coatings,” *J. Am. Ceram. Soc.*, vol. 84, no. 4, pp. 827–835, Apr. 2001.

[155] S. Rangaswamy, H. Herman, and S. Safai, “Thermal expansion study of plasma-sprayed oxide coatings,” *Thin Solid Films*, vol. 73, no. 1, pp. 43–52, Nov. 1980.

[156] B. Schulz, “Thermal conductivity of porous and highly porous materials,” *High Temp High Press*, vol. 13, p. 649, 1981.

[157] P. K. Wright and A. G. Evans, “Mechanisms governing the performance of thermal barrier coatings,” *Curr. Opin. Solid State Mater. Sci.*, vol. 4, no. 3, pp. 255–265, Jun. 1999.

[158] C. G. Levi, “Emerging materials and processes for thermal barrier systems,” *Curr. Opin. Solid State Mater. Sci.*, vol. 8, no. 1, pp. 77–91, Jan. 2004.

[159] R. A. Miller and C. E. Lowell, “Failure mechanisms of thermal barrier coatings exposed to elevated temperatures,” *Thin Solid Films*, vol. 95, no. 3, pp. 265–273, Sep. 1982.

[160] A. B. Abell, K. L. Willis, and D. A. Lange, “Mercury Intrusion Porosimetry and Image Analysis of Cement-Based Materials,” *J. Colloid Interface Sci.*, vol. 211, no. 1, pp. 39–44, Mar. 1999.

[161] C. A. Schneider, W. S. Rasband, and K. W. Eliceiri, “NIH Image to ImageJ: 25 years of image analysis,” *Nat. Methods*, vol. 9, no. 7, pp. 671–675, Jul. 2012.

[162] G Zaccai and and B. Jacrot, “Small Angle Neutron Scattering,” *Annu. Rev. Biophys. Bioeng.*, vol. 12, no. 1, pp. 139–157, 1983.

[163] A. J. Allen, J. Ilavsky, G. G. Long, J. S. Wallace, C. C. Berndt, and H. Herman, “Microstructural characterization of yttria-stabilized zirconia plasma-sprayed deposits using multiple small-angle neutron scattering,” *Acta Mater.*, vol. 49, no. 9, pp. 1661–1675, May 2001.

[164] S. Deshpande, A. Kulkarni, S. Sampath, and H. Herman, “Application of image analysis for characterization of porosity in thermal spray coatings and correlation with small angle neutron scattering,” *Surf. Coat. Technol.*, vol. 187, no. 1, pp. 6–16, Oct. 2004.

[165] N. M. Yanar, F. S. Pettit, and G. H. Meier, “Failure characteristics during cyclic oxidation of yttria stabilized zirconia thermal barrier coatings deposited via electron beam physical vapor deposition on platinum aluminide and on NiCoCrAlY bond coats with processing modifications for improved performances,” *Metall. Mater. Trans. A*, vol. 37, no. 5, pp. 1563–1580, May 2006.

[166] J. M. Pardal, S. S. M. Tavares, M. da P. C. Fonseca, J. A. de Souza, L. M. Vieira, and H. F. G. de Abreu, “Deleterious phases precipitation on superduplex stainless steel UNS S32750: characterization by light optical and scanning electron microscopy,” *Mater. Res.*, vol. 13, no. 3, pp. 401–407, Sep. 2010.

[167] D. N. Winslow, “Advances in Experimental Techniques for Mercury Intrusion Porosimetry,” in *Surface and Colloid Science*, Springer, Boston, MA, 1984, pp. 259–282.

[168] Y. Tan, “Thermal Design and Microstructure-Based Property Assessment for Thermal Spray Coating Systems,” Stony Brook University, New York, 2007.

Appendix

This section includes the MATLAB codes and details of Image J used during the thesis work.

The code used to calculate the thermal conductivity using the five-phase is given below.

MATLAB Code for thesis

```
% f
f1=0.058;
f2=0.02;
f3=0.047;
f4=0.044;

% X
X1=1.66;
X2=7;
X3=1.7;
X4=2;

% p
p1=f1/(1-(f2+f4+f3));
p2=f2/(1-(f3+f4));
p3=f3/(1-f4);
p4=p1;
p5=p2;
p6=f4/(1-f3);
p7=p1;
p8=f3/(1-(f2+f4));
p9=f2/(1-f4);
p10=p1;
p11=p8;
p12=f4/(1-f2);
p13=p1;
p14=f4/(1-(f2+f3));
p15=f2/(1-f3);
p16=p1;
p17=p14;
p18=f3/(1-f2);

 %r
r1=f2/(1-(f1+f3+f4));
r2=f1/(1-(f3+f4));
r3=f3/(1-f4);
```

```
r4=r1;
r5=r2;
r6=f4/(1-f3);
r7=r1;
r8=f3/(1-(f1+f4));
r9=f1/(1-f4);
r10=r1;
r11=r8;
r12=f4/(1-f1);
r13=r1;
r14=f4/(1-(f1+f3));
r15=f1/(1-f3);
r16=r1;
r17=r14;
r18=f3/(1-f1);

s1=f3/(1-(f1+f2+f4));
s2=f1/(1-(f2+f4));
s3=f2/(1-f4);
s4=s1;
s5=s2;
s6=f4/(1-f3);
s7=s1;
s8=f2/(1-(f1+f4));
s9=f1/(1-f4);
s10=s1;
s11=s8;
s12=f4/(1-f1);
s13=s1;
s14=f4/(1-(f1+f2));
s15=f1/(1-f2);
s16=s1;
s17=s14;
s18=f2/(1-f1);

t1=f4/(1-(f1+f2+f3));
t2=f1/(1-(f3+f2));
t3=f3/(1-f2);
t4=t1;
t5=t2;
t6=f2/(1-f3);
t7=t1;
t8=f3/(1-(f1+f2));
t9=f1/(1-f2);
t10=t1;
t11=t8;
t12=f2/(1-f1);
t13=t1;
t14=f2/(1-(f1+f3));
t15=f1/(1-f3);
```

t16=t1;　　t18=f3/(1-f1);

t17=t14;

A=((((1-p1)^X1)*((1-p2)^X2)*((1-p3)^X3)*((1-f4)^X4))+(((1-p4)^X1)*((1-p5)^X2)*((1-p6)^X4)*((1-f3)^X3))+(((1-p7)^X1)*((1-p8)^X3)*((1-p9)^X2)*((1-f4)^X4))+(((1-p10)^X1)*((1-p11)^X3)*((1-p12)^X4)*((1-f2)^X2))+(((1-p13)^X1)*((1-p14)^X4)*((1-p15)^X2)*((1-f3)^X3))+(((1-p16)^X1)*((1-p17)^X4)*((1-p18)^X3)*((1-f2)^X2)));

B=((((1-r1)^X2)*((1-r2)^X1)*((1-r3)^X3)*((1-f4)^X4))+(((1-r4)^X2)*((1-r5)^X1)*((1-r6)^X4)*((1-f3)^X3))+(((1-r7)^X2)*((1-r8)^X3)*((1-r9)^X1)*((1-f4)^X4))+(((1-r10)^X2)*((1-r11)^X3)*((1-r12)^X4)*((1-f1)^X1))+(((1-r13)^X2)*((1-r14)^X4)*((1-r15)^X1)*((1-f3)^X3))+(((1-r16)^X2)*((1-r17)^X4)*((1-r18)^X3)*((1-f1)^X1)));

C=((((1-s1)^X3)*((1-s2)^X1)*((1-s3)^X2)*((1-f4)^X4))+(((1-s4)^X3)*((1-s5)^X1)*((1-s6)^X4)*((1-f2)^X2))+(((1-s7)^X3)*((1-s8)^X2)*((1-s9)^X1)*((1-f4)^X4))+(((1-s10)^X3)*((1-s11)^X2)*((1-s12)^X4)*((1-f1)^X1))+(((1-s13)^X3)*((1-s14)^X4)*((1-s15)^X1)*((1-f2)^X2))+(((1-s16)^X3)*((1-s17)^X4)*((1-s18)^X2)*((1-f1)^X1)));

D=((((1-t1)^X4)*((1-t2)^X1)*((1-t3)^X3)*((1-f2)^X2))+(((1-t4)^X4)*((1-t5)^X1)*((1-t6)^X2)*((1-f3)^X3))+(((1-t7)^X4)*((1-t8)^X3)*((1-t9)^X1)*((1-f2)^X2))+(((1-t10)^X4)*((1-t11)^X3)*((1-t12)^X2)*((1-f1)^X1))+(((1-t13)^X4)*((1-t14)^X2)*((1-t15)^X1)*((1-f3)^X3))+(((1-t16)^X4)*((1-t17)^X2)*((1-t18)^X3)*((1-f1)^X1)));

$$k = \frac{k_0}{24}(A+B+C+D)$$

The f_1 to f_4 can vary according to the content of different types of defects present in the coating.

Weblink for Image J

Details regarding the Image J software can be obtained from the National Institutes of Health (NIH) website. The link is provided below. This software is open-source software which can be freely used and modified.

https://imagej.nih.gov/ij//